Innovative methods for retrieving cloud properties from the BASTA radar

Pragya Vishwakarma

université PARIS-SACLAY

Méthodes innovantes pour la restitution des propriétés des nuages à partir du radar BASTA

Innovative methods for retrieving cloud properties from BASTA radar

Thèse de doctorat de l'université Paris-Saclay

École doctorale n° 129, Sciences de l'Environnement d'Ile-de-France (SEIF)
Spécialité de doctorat : Instrumentation, télédétection, observation et techniques spatiales pour l'océan, l'atmosphère et le climat
Graduate School : Géosciences, Climat, Environnement et Planètes,
Référent : Université de Versailles-Saint-Quentin-en-Yvelines

Thèse préparée dans l'unité de recherche LATMOS (Université Paris-Saclay, UVSQ, CNRS), sous la direction de **Julien DELANOË**, Maître de conférences

Thèse soutenue à Guyancourt, le 14 avril 2022, par

Pragya VISHWAKARMA

Composition du jury

Hélène BROGNIEZ Professeure des Universités, UVSQ-Paris Saclay (LATMOS)	Présidente
Alexis BERNE Professeur Associé, EPFL (LTE)	Rapporteur & Examinateur
Céline CORNET Professeure des Universités, UDL (LOA)	Rapporteur
Pauline MARTINET Chargée de Recherche, Météo-France (CNRM)	Examinatrice
Julien DELANOË Maître de conférences, UVSQ-Paris Saclay (LATMOS)	Directeur de thèse

THESE DE DOCTORAT

NNT : 2022UPASJ009

université PARIS-SACLAY

ÉCOLE DOCTORALE
Sciences de l'Environnement d'Île-de-France (SEIF)

Titre : Méthodes innovantes pour la restitution des propriétés des nuages à partir du radar BASTA
Mots clés : Nuages, Brouillard, Radar, Radiomètre, Algorithme

Résumé : Des études ont montré que la représentation des nuages de basse altitude est encore sous-estimée dans divers modèles climatiques. Un des paramètres fondamentaux pour caractériser les propriétés microphysiques de ces nuages est le contenu en eau liquide (LWC). Cette thèse vise à développer un algorithme d'estimation du LWC de ces nuages en combinant radar nuage à 95GHz (BASTA) et radiomètre micro-ondes (MWR). On utilise traditionnellement des relations empiriques du type $Z = aLWC^b$ (Z étant la réflectivité radar). Cependant, ces relations ne représentent pas toujours la variabilité de la distribution en taille des gouttes dans un système nuageux hétérogène et ne tiennent pas compte de l'atténuation des nuages liquides. Je réutilise ce concept mais la contrainte sur le pré-facteur « a » est relachée en ajoutant des informations supplémentaires telles que le contenu intégré en eau liquide (LWP), ici restitué par le radiomètre. Pour tester le comportement de l'algorithme, un test de sensibilité est réalisé en utilisant des profils de brouillard synthétiques issus d'une simulation AROME. L'étude de sensibilité ne permettant pas de valider les hypothèses microphysiques de la méthode, le LWC restitué est comparé aux observations in-situ recueillies pendant la campagne SOFOG-3D. Enfin, l'algorithme est appliqué à 39 cas de nuages et de brouillard de novembre 2018 à mai 2019 à l'observatoire SIRTA afin de construire une climatologie de LWC et de valeurs de « a ». Puisque la méthode de restitution doit être utilisable même sans information du radiomètre, nous utilisons cette climatologie comme connaissance a priori des valeurs de « a » ce dernier n'étant plus contraint par le LWP.

Title : Innovative methods for retrieving cloud properties from the BASTA radar
Keywords : Clouds, Fog, Radar, Radiometer, Algorithme

Abstract : Studies have shown that the representation of low-level clouds is still underestimated in various climate models. One of the fundamental parameters to characterize the microphysical properties of these clouds is the liquid water content (LWC). This thesis aims to develop an algorithm for estimating the LWC of these clouds by combining cloud radar at 95GHz (BASTA) and microwave radiometer (MWR). Traditionally, empirical relations of the type $Z = aLWC^b$ (Z being the radar reflectivity) are used. However, these relationships do not always represent the variability of the droplet size distribution in a heterogeneous cloud system and do not take into account the attenuation of liquid clouds. I reuse this concept but the constraint on the pre-factor "a" is relaxed by adding additional information such as the integrated liquid water content (LWP), here retrieved by the radiometer. To test the behavior of the algorithm, a sensitivity test is performed using synthetic fog profiles from an AROME simulation. As the sensitivity study does not allow the microphysical hypotheses of the method to be validated, the retrieved LWC is compared to the in-situ observations collected during the SOFOG-3D campaign. Finally, the algorithm is applied to 39 cases of clouds and fog from November 2018 to May 2019 at the SIRTA observatory in order to build a climatology of LWC and "a" values. Since the restitution method must be usable even without information from the radiometer, we use this climatology as a priori knowledge of the values of "a", the latter no longer being constrained by the LWP.

Acknowledgements

This Ph.D. thesis has been full of learnings for me. I got a chance to live abroad for the first time, which has introduced me to a new culture and environment. Everyone during this journey has contributed directly or indirectly, and I hope that I have not forgotten someone, even if the name is not listed explicitly.

First of all, I want to thank my supervisor Dr. Julien Delanoë for giving me this opportunity and the valuable guidance throughout my Ph.D. Your expertise, enthusiasm, and ideas have enriched my doctoral experience. Your patience is undoubtedly the main reason that I could finish this document and earn this degree. Thank you for persisting with me when my work was moving at trudging pace.

I want to extend my gratitude to the jury members for accepting to examine my thesis; without your suggestions and remarks, this document could not get this quality. My sincere gratitude goes out to Pauline Martinet and Olivier Jourdan, members of the thesis committee, for the annual committee meetings and sharing the insightful suggestions to improve this work.

I would like to thank CIFRE and Meteomodem for funding this project. Many thanks to Gaëlle Clain, Damien Vignelles, and Patrick Charpentier from Meteomodem for all the support since my recruitment.

Huge thanks to the BASTA, SIRTA, and SOFOG-3D teams for their contributions and efforts.

Many thanks to the director of LATMOS and the members of the SPACE group for their generosity and for making me feel welcome in this research group. Thank you, Nicolas Viltard, for sharing your ideas and cheering me up all along. Special thanks to the IT team and the administrative team for her irreplaceable help, particularly during the exceptional circumstance of the pandemic.

I want to direct my special thanks to Eva Le Merle for the time she took to help me get settled with the administrative issues during the first few months of my Ph.D. Thank you for introducing me to French culture and language and being a perfect officemate. Thank you, Quitterie and Constantino, for helping me over the initial troubles as a foreigner.

A big hug to my Ph.D. fellow mates for sharing those moments of smile and laughter,

as well as discussion over struggles during our coffee breaks and lunches. Erik, Milissa, Felipe, Minh, Chloé, Clémentyne, and Vibolroth, thank you for all the fun moments and for making me feel at ease. Oscar, my Columbian friend with French nationality, you have been my saviour all the time, Muchas gracias! Thank you, Susana Jorquera, for all the help and support, and for being so kind.

Because of the pandemic, I spent nearly half of my Ph.D. time working remotely. Thanks to Cité Universitaire for providing me a home away from home. Thank you Shalu and Surabhi for sharing happy times and journeys and for being there for me through thick and thin.

Special thanks to my friends and colleagues from India. I appreciated all the time we spent together when I was visiting you and all the chats we had on phone calls. Thank you, Akshay, Rohith, Rekha Ma'am, Abhishek Sir, Aniket, Darshika di, and Bhumika, for the constant encouragement and giving me that extra push to survive.

Most importantly, I want to thank my parents for their endless love, blessings, and trust in me. My heartfelt thanks and love would go to my brother and the rest of my family for cheering me up all these days while being abroad.

Résumé

Les nuages sont essentiels à de nombreux aspects de l'existence humaine sur terre. Ils ont également un impact significatif sur le bilan énergétique de la Terre. Bien que l'effet des nuages sur le climat soit complexe et ne soit pas entièrement compris, une grande partie de l'incertitude concernant le réchauffement climatique est liée aux mécanismes de rétroaction des nuages sur le climat. Des études ont montré que la représentation des nuages de basse altitude est encore sous-estimée dans divers modèles climatiques. La nécessité d'examiner les propriétés des nuages à différents niveaux est devenue une priorité dans l'observation de la terre. Des observations continues et détaillées des nuages sont nécessaires pour caractériser les propriétés des nuages à l'échelle locale et mondiale. Les instruments de télédétection active et passive tels que les radars de nuages, les lidars, les radiomètres dans le visible et les micro-ondes ont l'avantage de permettre une observation continue pendant de longues périodes depuis le sol ou l'espace. Ces capteurs fournissent des observations de l'état de l'atmosphère à plusieurs longueurs d'onde du spectre électromagnétique et à différentes résolutions temporelles et spatiales. Un des paramètres fondamentaux pour caractériser les propriétés microphysiques de ces nuages de basse altitude est le contenu en eau liquide (LWC). Cette thèse vise à développer un algorithme d'estimation du LWC de ces nuages en utilisant de manière synergique le radar nuage (95 GHz) et le radiomètre micro-ondes (MWR). Un radar mesure l'énergie rétrodiffusée par les gouttelettes nuageuses et elle est représentée par le facteur de réflectivité radar (Z). Pour restituer le LWC de ces nuages, on utilise traditionnellement des relations empiriques qui suivent une loi de puissance telle que $Z = aLWC^b$. Cependant, ces relations ne représentent pas toujours la variabilité de la distribution en taille des gouttes dans un système nuageux hétérogène et ne tiennent pas compte de l'atténuation des nuages liquides. Dans cette thèse, je propose de réutiliser le même concept, mais la contrainte sur le pré-facteur « a » est relachée en ajoutant des informations supplémentaires telles que le contenu intégré en eau liquide (LWP), ce dernier sera obtenu à partir du radiomètre. Mon algorithme de restitution est basé sur une théorie d'estimation probabiliste appelée approche variationnelle. Grâce à ce cadre flexible, lorsque l'information sur le contenu en eau liquide intégré provenant du MWR est assimilée, le pré-facteur « a » peut également être restitué. Pour tester

le comportement de l'algorithme de récupération, une analyse de sensibilité pour les perturbations des paramètres clés en utilisant des profils de brouillard synthétiques est menée en utilisant des simulations d'un modèle de prévision météorologique numérique appelé AROME. Pour tester le comportement de l'algorithme, un test de sensibilité est réalisé en utilisant des profils de brouillard synthétiques issus d'une simulation AROME. L'analyse a montré que l'algorithme est très sensible au biais appliqué à LWP car il s'agit d'une information intégrée verticalement qui va impacter l'ensemble du profil. D'autres paramètres, tels que l'exposant « b » et des relations d'atténuation alternatives, ont moins d'impact sur les résultats de l'algorithme. Comme le test de sensibilité ne permet pas de valider les hypothèses microphysiques de la méthode, le LWC restitué est comparé aux observations in-situ recueillies pendant la campagne SOFOG-3D. Les observations d'un radar nuage et d'un radiomètre micro-ondes co-localisés sont utilisées pour restituer LWC, et la comparaison a montré une meilleure concordance avec les observations in-situ pour les stratus que pour le brouillard. Ce résultat est principalement lié au fait que les mesures dans le stratus étaient réalisées dans une zone beaucoup plus homogène que pour le brouillard. Enfin, l'algorithme est appliqué à 39 cas de nuages et de brouillard de novembre 2018 à mai 2019 à l'observatoire SIRTA afin de construire une climatologie de LWC et de valeurs de pré-facteur « a ». Puisque la méthode de restitution doit être utilisable même sans information du radiomètre, nous proposons d'utiliser cette climatologie comme connaissance a priori des valeurs du pré-facteur « a » ce dernier n'étant pas contraint par le LWP.

Abstract

Clouds are critical to the majority of aspects of human existence on earth. They also have a significant impact on the earth's energy balance. Although the effect of clouds on the climate is complex and not fully understood, much of the uncertainty about global warming is related to the cloud-climate feedback problem. Studies have shown that the representation of low-level clouds is still underestimated in various climate models. The necessity to examine the cloud properties at different levels has emerged as a priority in earth observation. Continuous and detailed observations of clouds are needed to characterize the cloud properties on a local and global scale. Active remote and passive sensing instruments like cloud radars, lidars, visible and microwave radiometers have the advantage of continuous observation for long periods from the ground or space. One of the fundamental parameters to characterize the microphysical properties of these low-level clouds is the liquid water content (LWC). This thesis aims at developing an algorithm estimating LWC in low-level clouds using cloud radar and microwave radiometer (MWR) synergy when the latter is available. A 95GHz cloud radar measures the backscattered energy from cloud droplets in terms of radar reflectivity factor (Z). Traditionally, empirical relations following a power law such as $Z = aLWC^b$ are used to retrieve the LWC of low-level liquid clouds. However, such relationships do not always represent the variability of drop size distribution in a heterogeneous cloud system and do not account for liquid cloud attenuation. In this thesis, I propose using the same concept, but the constraint on 'a' from the power law is released by adding extra information such as the liquid water path (LWP), which is provided by the microwave radiometer. My retrieval algorithm is based on probabilistic estimation theory called the variational approach. Thanks to this flexible framework, when LWP information from MWR is assimilated, the LWC in the profile is scaled by LWP information, and the scaling factor 'a' can also be retrieved for each profile. To test the behavior of the retrieval algorithm, a sensitivity analysis for perturbations in key parameters using synthetic fog profiles is conducted using simulations from a numerical weather prediction model called AROME. The analysis has shown that the algorithm is very sensitive to the bias in LWP because it is a vertically integrated information and thus plays a critical role in the retrieval. Other parameters, such as 'b'

and alternative attenuation relationships, have less implications on the stability of the algorithm. Because the sensitivity test is not validating the microphysical assumptions of the method, the validation of such an algorithm is challenging, as we need reference measurements of LWC co-located with the retrieved values. During the SOFOG-3D campaign, in-situ measurements of LWC were collected in the vicinity of a cloud radar and a microwave radiometer, allowing comparison against my retrieved LWC. The comparison showed better agreement with in-situ observations for stratus clouds than fog. This is mainly explained by the fog heterogeneity during the measurements, cloud-fog heterogeneity is therefore an important factor in the assessment. Finally, the retrieval algorithm is employed to build a climatology of LWC and 'a' for 39 cloud and fog cases from November 2018 to May 2019 at the SIRTA observatory. Since the retrieval method must be usable without radiometer information, we propose using this climatology as a priori knowledge for the scaling factor, which is no longer constrained by LWP.

Contents

List of Figures

List of Tables

Chapter 1

Introduction and Motivation

Clouds are one of the most fascinating weather phenomena observable to the naked eye, and have puzzled humans for centuries. Clouds were first thought to be made of water bubbles. With the advancements in science, it was confirmed that clouds consists of microscopic water droplets and/or ice crystals suspended in atmosphere. In addition to their role in the hydrological cycle providing us fresh water, the vertical and horizontal transfers of energy from the smallest to the largest scales are induced by cloud water condensation and evaporation processes.

Furthermore, clouds are strongly linked to the energy and water budgets of the Earth-Ocean-Atmosphere system. The global radiative equilibrium is greatly influenced by both ice clouds and liquid water clouds, with the global cloud fraction of around 60% to 70% [King et al., 2013]. The scattered white clusters in figure 1.1 indicate the cloud fraction (means the area that was cloudy) averaged for the month of July 2020, seen by MODIS, a sensor on NASA's Terra satellite. The colour range from blue indicating no clouds to white referring to a totally cloudy pixel. A band of dense clouds around the equator called Inter-Tropical Convergence Zone (ITCZ) is responsible for rainy and dry seasons over tropical countries. The prominent cloud-free skies over the Sahara, southwest Asia, Australia, and Antarctica are showing the driest areas on earth, while clouds over ocean are common all over the globe.

When clouds reflect the incoming solar radiations back, it cools the planet. But they also absorb terrestrial radiations from earth-atmosphere system and heats the planet (cloud albedo effect). The net effect of clouds on earth's radiative balance depends on the optical and microphysical properties of clouds.

Since the beginning of climate change and global warming investigations, clouds have been a key concern. The low-level tropical clouds are the most uncertain feedback in current climate models [Brient and Schneider, 2016]. A comparison of five climate models has shown that the low-level clouds are underestimated at all the latitudes [Cesana and Chepfer, 2012]. The vertical structure of low-level clouds has been demonstrated

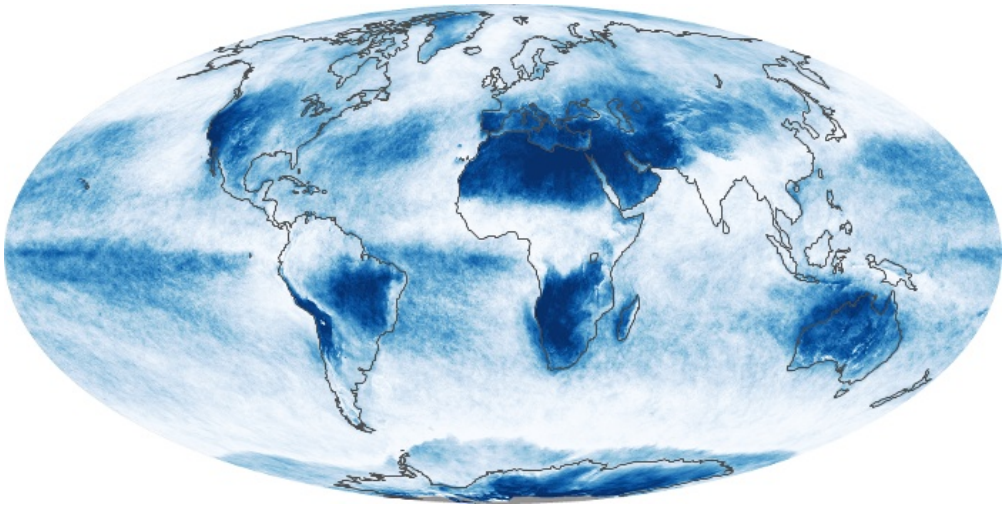

Figure 1.1: Cloud Fraction. The image shows measurement from Moderate Resolution Imaging Spectroradiometer (MODIS) on NASA's Terra satellite for July 2020. Figure source: `https://earthobservatory.nasa.gov/global-maps/MODAL2_M_CLD_FR`

to be inaccurately represented by many climate models [Nam et al., 2012]. These uncertainties in the climate projections are due to the poor representation of their microphysical properties in the models. Low-level clouds also include fog, which is formed when supersaturated air condenses near the ground. Fog differs from cloud only with the fact that the base of fog is at the earth's surface, while clouds are above the surface. Visibility at the ground reduces during fog due to the scattering of visible radiation by droplets, which is hazardous for transportation, especially aviation. Fog also plays an important role in the processing of aerosol particles and trace gases in the atmosphere; for example, urban fog traps more pollutants than clouds at high altitudes [Fišák et al., 2001]. Fog forecasts are still inaccurate due to the complexity of fine scale processes involved in fog life cycle [Martinet et al., 2020]. Therefore, the observations of these warm low-level clouds can advance our understanding of microphysical properties and their representation in models.

The fundamental parameters to characterize the microphysical properties of these low-level clouds is liquid water content (LWC), number concentration (the total number of water droplets per cubic meter of air), and the droplet size distribution (number of droplets per cubic meter in various droplet size bins). These parameters are not independent, and if the droplet spectrum is known, we can compute any moment of droplet distribution. For example, LWC is simply the sum of mass of water in each bin and is proportional to the third moment of droplet size distribution.

To support the improvement in representation of cloud microphysical processes, long-term and continuous observations of clouds are crucial on local and global scales. Remote sensing instruments such as microwave radiometers, infrared radiometers, lidar,

and cloud radars can measure radiation emitted or backscattered by cloud droplets that carries indirect information about their properties. Active remote sensing instruments like cloud radar and lidar can provide the vertical structure of clouds. Depending on the platforms used, these remote sensing instruments can measure the radiative equivalents of microphysical properties at high spatial and temporal resolution at a single point (ground-based) or broad spatial coverage with a lower spatial resolution (satellite). The detection capability of space borne radar is however limited for low-level clouds due to surface contamination. Ground-based observations are particularly beneficial for low-level cloud observations, as ground based instruments are closer to them and therefore, better signal-to-noise ratio can be obtained.

For instance, a cloud radar works by transmitting energy in the atmosphere and measures the power backscattered by clouds (discussed in Chapter 3). The backscattered power received from a sampling volume (cloud droplets) is assumed proportional to the sixth moment of the particle size distribution. But the microphysical properties of clouds are not directly measured; instead the radiative equivalents like radar reflectivity Z are used to infer or retrieve cloud microphysical properties of interest. Several methods and algorithms are proposed in the literature to interpret cloud LWC from radar reflectivity Z. For liquid-phase boundary layer clouds, traditional methods to relate radar reflectivity with LWC include empirical relations in the form of $Z = a \cdot LWC^b$ with constant values of a and b [Atlas, 1954],[Baedi et al., 2000],[Fox and Illingworth, 1997]. The coefficients a and b are derived empirically from in-situ aircraft measurements of drop size distribution. Such relationships may not adequately describe the variability present in a continuous and inhomogeneous cloud system because of certain assumptions in the drop size distribution (e.g., clouds without drizzle). In the past studies, algorithms based on instrument synergies from two or more remote sensing instruments have been shown to improve the LWC estimations of clouds using radar reflectivity [Frisch et al., 1995],[Frisch et al., 1998],[Löhnert et al., 2004],[Illingworth et al., 2007]. However, a comparison of some available retrieval methods have shown discrepancies in the estimated microphysical properties due to difference in the assumptions employed to infer cloud properties from remote sensing observations [Zhao et al., 2012]. This is especially found to be the case when clouds and large droplets called drizzle coexist, for which the microphysical characteristics are more complex. Some example of synergy and retrievals are shown in Chapter 4. Generally, cloud radars also have Doppler capabilities and a Doppler velocity spectrum is a measure of backscattered energy per unit radial velocity. The velocity is calculated using phase shifts due to individual droplet motion along the radar beam [Giangrande et al., 2001]. The first three moments of Doppler velocity spectrum corresponds to total backscattered power Z (zeroth moment), the mean Doppler velocity V_D (first moment) and the Doppler spectral width σ_D (second

moment) [Kollias et al., 2011]. The velocity spectra of the sampled volume is a function of hydrometeors diameters distribution, which is further used to estimate microphysical properties.

The main objective of my thesis is to propose a methodology to retrieve liquid cloud properties using cloud radar. In addition to the scientific question of liquid clouds, my work is also related to the industry. Another aspect of this research is to find new markets for the BASTA cloud radar [Delanoë et al., 2016], a ground-based 95 GHz FMCW (Frequency Modulated Continuous Wave) radar developed in LATMOS and commercialized by Météomodem during my thesis. For instance, users with no particular radar scientific expertise could appreciate an LWC product for liquid clouds and fog using radar measurements that can be automated.

As discussed in the last paragraph, LWC retrieval using only radar reflectivity measurements is extremely dependent on the DSD and therefore LWC retrieval directly using radar reflectivity is under-constrained. In this thesis, to improve the accuracy of LWC retrieval, a synergistic LWC retrieval algorithm is presented that combines two co-located active and passive remote sensing instruments. My retrieval method estimates the LWC using radar reflectivity Z from cloud radar and liquid water path (LWP) from a microwave radiometer and accounts for attenuation in the radar signal due to liquid clouds. Because the Doppler spectrum from BASTA cloud radar is not operationally available, I decided to use the synergy of radar reflectivity Z and LWP from microwave radiometer. The selection of an additional parameter as LWP from a co-located microwave radiometer is because the LWP information of the profile can scale the cloud profile and improve the accuracy of LWC estimates [Ovtchinnikov and Kogan, 2000]. The algorithm will be detailed in the following sections where I have chosen to combine a traditional approach to link Z and LWC (i.e., $Z = a \cdot LWC^b$) and the knowledge of LWP (when available), which will enable the retrieval of prefactor 'a' for each cloud profile in addition to LWC. A flexible approach is required because a microwave radiometer does not always accompany the radar, and therefore and independent estimate of LWP might not be available. Hence, the proposed method must be robust enough to be applied to radar measurements in both synergy configurations (with a microwave radiometer) and in stand-alone radar configurations as well. *A priori* and the measurement errors are incorporated in the LWC retrieval using the variational method [Rodgers, 2000]. This technique allows the estimation of LWC which is physically consistent within the specified errors. However, to test the robustness of the algorithm and identify how much the variations in the input variables and errors impact the estimated LWC, a sensitivity test of the algorithm is conducted. To do so, we need profiles of LWC, which we consider truth, and in this case, I used synthetic profiles of LWC of a fog case from the AROME model forecast [Bell et al.,

2021]. The synthetic values are just a representative of LWC used to simulate input parameters of the retrieval algorithm to verify the stability of the algorithm for different perturbations. The detailed sensitivity analysis of the algorithm is discussed in Chapter 5. Note that fog and cloud microphysical properties are comparable; this method can be used in fog circumstances and cloud cases.

However, the sensitivity test of the algorithm does not allow us to validate the microphysical assumptions in the retrieval method. Due to the fact that all algorithms are based on certain assumptions and theories, cloud retrievals may differ due to the varied assumptions. Evaluation of retrieved parameters with the observations is an essential aspect of the applicability of remote sensing instruments. In order to compare the estimated value of LWC with in-situ measurements, we need the simultaneous cloud observations with cloud radar, microwave radiometer and the in-situ sensors. Thus, I used the tethered balloon-borne measurements collected during the SOFOG-3D campaign (described in chapter 3) to compare the LWC. The co-located observations from radar and microwave radiometer during the campaign are used to estimate LWC of cloud. The comparison of LWC for fog and stratus cloud with LWC measured by the in-situ sensor is discussed in Chapter 5.

The application of this algorithm cannot be limited to case studies. The ground-based remote sensing instruments are also beneficial for long periods of observations of low-level clouds, therefore we propose a climatology of LWC over several months at SIRTA observatory (presented in Chapter 3). A variety of cloud cases are selected to estimate LWC and prefactor a, and the behaviour of retrieved parameters is analysed. As the prefactor, a is retrieved because additional information from the microwave radiometer is assimilated in the retrieval, and such climatology of prefactor a has not been developed before, which can be helpful in establishing new retrieval methods for low-level clouds.

Additionally, for the stand-alone radar retrieval we need to constraint the LWC retrievals, which can be accomplished by using the climatology of liquid phase cloud. The idea is to learn from the synergistic retrieval and utilize that knowledge to direct the retrieval when synergy is not possible. Therefore, when the microwave radiometer is not accompanying the radar, the radar stand-alone retrieval algorithm utilizes the climatology of the prefactor a to constrain the LWC. The climatology of prefactor a as a function of radar parameters is chosen as the *a priori* of the cloud profile in the algorithm that allows the variability in the LWC retrieval. Chapter 5 ends by presenting the results of the stand-alone retrieval technique applied to BASTA radar cloud observations.

The retrievals of the stand-alone algorithm can be improved by using a larger climatology of liquid phase clouds and a better classification of hydrometeor, and the thesis is concluded in Chapter 6. Finally, the outlook of the thesis and possible ways to improve

the LWC retrieval method for warm clouds is presented.

Chapter 2

Clouds

In this chapter, an introduction to fundamentals of clouds used in this thesis are presented. Section 2.2 introduces some basic concepts of Earth's radiative equilibrium, followed by cloud interactions and their impacts. Finally, the chapter explains the concept of radiative forcing and climate feedbacks.

2.1 Cloud formation and classification

The building blocks of clouds are water droplets and suspended particles of dust, sea salt, etc., called Cloud Condensation Nuclei (CCN). These solid and liquid particles, also called aerosols, are released into the atmosphere by a variety of natural (volcanic ashes, ocean wave breaking) and anthropogenic processes (pollution, biomass burning, etc.). The fundamental concepts of cloud formation in this subsection are typically found in a basic textbook on atmospheric science, (e.g. Wallace and Hobbs [2006], Lamb and Verlinde [2011]).

As the moist air rises through the atmosphere, it cools due to lower atmospheric pressure. The rate of cooling can vary depending on the water content, or humidity of the air. The cold air cannot hold as much water vapour as warm air can, therefore when air cools and reaches dew point temperature (the temperature at which condensation occurs), it gets saturated and the water vapour in it condenses to form a cloud droplet. This condensation (for liquid) or deposition (for ice) of water vapour is called homogeneous nucleation of pure water. But, the energy required for homogeneous nucleation is too high in usual atmospheric conditions. Instead, natural clouds condenses on atmospheric aerosol by a process known as heterogeneous nucleation. The condensation or deposition of water vapour on these so-called cloud condensation nuclei forms the cloud droplets or ice crystals. Most CCN consists of a mixture of soluble and insoluble components. The formation of clouds occurs in the troposphere (the lowest layer of the earth's atmosphere, containing 75% of the total mass of the atmosphere). Between the boundary layer and

the free troposphere, the concentrations of CCN drop by a factor of five over land. Once the cloud droplet is formed, it may grow, for instance, by colliding with other droplets and coalescing with them until they reach a sufficient size to precipitate.

We can also categorize clouds based on the phase of cloud particles. *Warm clouds* or liquid water clouds are found mainly in low altitudes of the atmosphere where the temperature is higher. Water droplets commonly remain liquid and do not freeze, even well below 0°C isotherm. These water droplets are referred to as supercooled droplets. *Cold clouds* often involve both ice crystals and liquid water (supercooled), and are more complicated than warm clouds. The microstructure of ice crystals is very complex, from dendrites to columns (long, pencil-like forms) or plates (thin, flat hexagons). High cirrus clouds are an extreme type of cold cloud, dominated by ice crystals. Clouds containing ice particles with supercooled water droplets are called *mixed-phase* clouds. Supercooled water droplets exist down to about -38°C; beyond this temperature, spontaneous homogeneous nucleation of an ice crystal from pure water droplets occurs. Cumulonimbus clouds may exhibit liquid water droplets at their base and ice crystal at their top, with mixed phases in between.

Since the early start of meteorological research, clouds have been classified corresponding to their appearance and their altitude. Luke Howard in the early 19th century established the classification between the three fundamental cloud classes cirrus, cumulus and stratus. Clouds are classified by their altitude, either the cloud base or the cloud top, is a commonly used parameter to distinguish low, middle and high-level clouds depending on the altitude of their occurrence. Clouds are constantly evolving and can take on an infinite variety of shapes. In 2017, World Meteorological Organization (WMO) updated the International Cloud Atlas, classifying cloud types into 'genera', 'species', and 'varieties', similar to plant and animal classification system. The approximate height of 10 genera of cloud for different latitudes in the troposphere is summarized in table 2.1 [WMO, 2017].

As shown in figure 2.1, high-level clouds are mainly made of ice crystals and are usually optically thin due to low concentrations of crystals due to cold and dry air. Mid-level clouds are made of liquid droplets and ice crystals, the ratio between both depends on the temperature of the ambient air. Generally, the cloud base of low-level clouds is located below 2 km. Those clouds are most of the time made of liquid droplets. Clouds with a high vertical structure with a low-level cloud base are made of liquid droplets at their base, and ice crystals at their top are mostly associated with thunderstorms. Cumulus, stratocumulus, stratus, and cumulonimbus are all examples of low-level clouds, and these clouds are impacted by the topography of the surface, such as hills, mountains, valleys, and so on. Stratus may also develop because of the rising fog layer due to warming or an increase in wind speed. A cloud which forms at

Table 2.1: Approximate heights of each level, and the genera occurring in different geographical regions. Table extracted from International cloud atlas (WMO)

Level	Genera	Polar region	Temperate region	Tropical region
High	Cirrus (Ci) Cirrocumulus (Cc) Cirrostratus (Cs)	3-8 km	5-13 km	6-18 km
Middle	Altocumulus (Ac) Altostratus (As) Nimbostratus (Ns)	2-4 km	2-7 km	2-8 km
Low	Stratus (St) Stratocumulus (Sc) Cumulus (Cu) Cumulonimbus (Cb)	From ground to 2 km	From ground to 2 km	From ground to 2 km

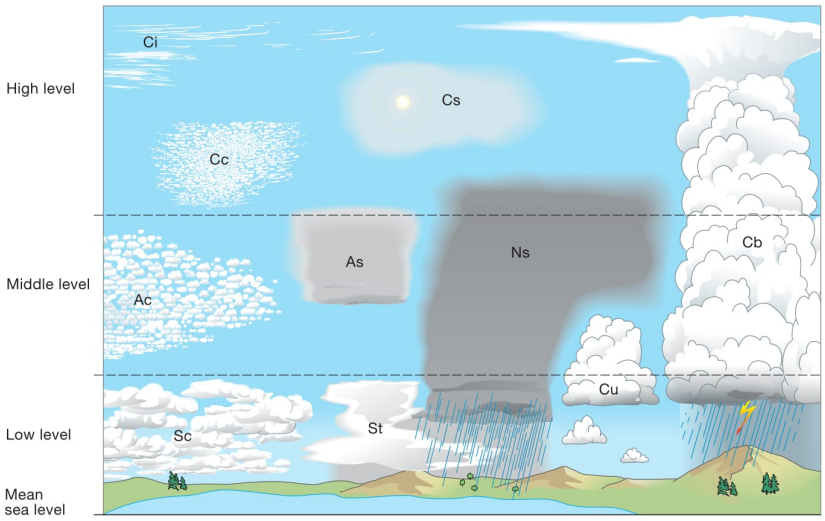

Figure 2.1: Cloud types and their approximate height in atmosphere. Figure extracted from International Cloud Atlas (WMO)

the ground, lowering the visibility to less than 1 km is called Fog. This occurs when supersaturated air condenses close to the ground. In cold environments, fog may also consist of suspended ice crystals. It is possible to achieve supersaturation of the air by either lowering its temperature or increasing its water vapour content, or a combination of the two. Therefore, several meteorological conditions can lead to the formation of fog, and fog types have been defined according to the mechanism causing the fog formation [Gultepe et al., 2006]. The wind has been found to be a significant factor in the development of fog; if the wind is too strong, turbulent mixing dilutes the cooling

and moistening in a layer that is too thick for supersaturation to occur, but mild wind may result in dew deposition rather than fog. Fog also plays an important role in the processing of aerosol particles and trace gases in the atmosphere; for example, urban fog traps more pollutants than clouds at high altitudes [Fišák et al., 2001]. Fog is also associated to reduction of visibility caused by suspended microscopic droplets, which impacts aviation industry. These are known as low-lying clouds and are influenced by the nearby water bodies, wind conditions, and surface topographies. The interaction of these different types of clouds with radiations is called the radiative properties of clouds and are discussed in the next section.

2.2 Earth's radiative balance and clouds

The sun is the primary energy source for most processes in the earth's system. Although the sun emits electromagnetic radiation at various wavelengths, most of the incoming solar radiations consist of visible and parts of ultraviolet and short infrared radiations. The electromagnetic (EM) radiations are characterized by their wavelength λ, or by its frequency ν. The two variables are related as $\lambda \times \nu = c$, where c is the speed of light ($c = 3 \times 10^8 ms^{-1}$ in vacuum). The wavelength of peak radiation emitted by an object is inversely related to its temperature (Wien's law). Due to the high surface temperature of the sun (average $5500K$), the wavelength of peak radiation has high intensity and shorter wavelengths, hence called shortwave(SW). The earth's surface and the atmosphere reflects as well as absorb these solar radiations (SW). A part of the radiation (around 30%) is reflected, and the fraction absorbed by the earth ($T \sim 300K$) is re-radiated at the longer wavelengths in the infrared region (about $\sim 10\mu m$) called longwave (LW) with relatively less intensity. Figure 2.2 presents the radiation intensity and range of wavelengths of incoming solar radiations and the emitted radiations from the earth. Notice that the radiation intensity on the y-axis is relative.

Several factors influence the amount of solar radiation reaching the earth's surface and the amount of radiation leaving the atmosphere. The interaction of radiation with atmospheric gases, water vapour, aerosols, and clouds includes absorption, emission, and scattering processes. These processes play a vital role in the thermodynamic conditions of the atmosphere.

2.2.1 Scattering, absorption and extinction processes

When radiation interacts with a particle, a part of the incident energy is absorbed, whereas the other is spatially redistributed in a non-isotropic direction. These processes are known as the absorption and scattering processes, respectively. The absorbed part

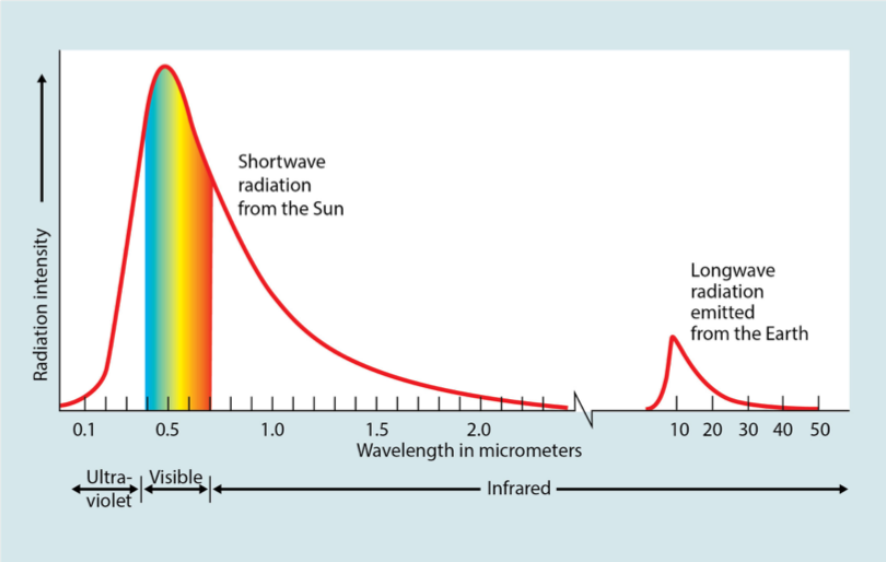

Figure 2.2: Incoming energy from the sun and outgoing energy from the earth relative to the wavelengths. Figure is extracted from Understanding Global Change(UCMP) webpage (see link) (https://ugc.berkeley.edu/background-content/re-radiation-of-heat/)

of the radiation is converted into molecular kinetic and potential energies whereas, scattered radiation is simply redirected without any loss of energy. The *extinction* or attenuation of radiation by a particle represents the sum of absorption and scattering processes. An electromagnetic wave of intensity I_λ propagates along an optical path dl in an atmospheric layer gets attenuated by a factor dI_{ext} which is given by:

$$dI_{ext} = -I_\lambda K_\lambda^{ext} dl \tag{2.1}$$

where K_λ^{ext} is the extinction coefficients and has unit m^{-1}. The contributions of scattering and absorption to the extinction of the incident beam of radiation defines the scattering and absorption coefficient, such as:

$$K_\lambda^{ext} = K_\lambda^{abs} + K_\lambda^{scat} \tag{2.2}$$

Scattering is a process, which conserves the total amount of energy, but the direction in which the radiation propagates may be altered. The amount of scattering depends on several factors, including the wavelength of the radiation, the size of particles (or gas molecules), the amount of particles, and the incident and scattering angles. If we assume a spherical particle of radius r, we define a dimensionless size parameter x to be the ratio of the circumference of the particle to the wavelength of radiation:

$$x = \frac{2\pi r}{\lambda} \tag{2.3}$$

Figure 2.3 shows the range of size parameters for various particles in the atmosphere

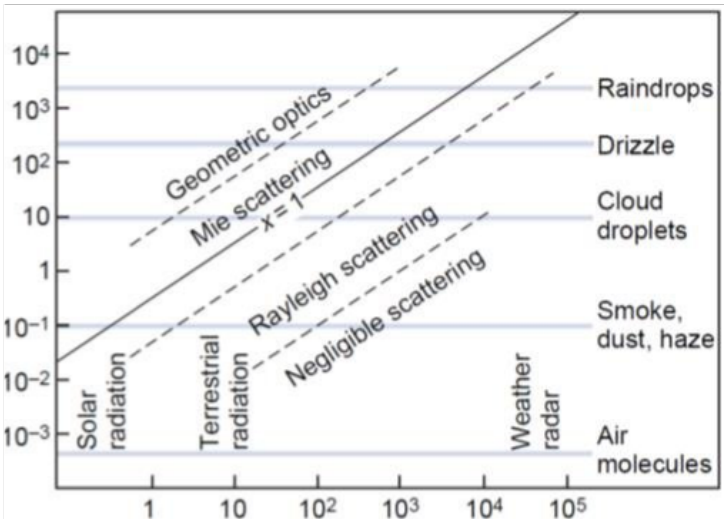

Figure 2.3: Scattering regimes and particle types based on size parameter (x), wavelength λ and radius (r) (replicated from Wallace and Hobbs, 2006[Wallace and Hobbs, 2006])

and radiation in different wavelength ranges. When the particle is small compared with the wavelength, the size parameter $x << 1$, the scattering is weak and symmetrically distributed. In this so-called Rayleigh scattering regime, the scattering is divided evenly in the forward and backward direction, as shown in figure 2.4. The particle for which the size parameter is comparable to the wavelength ($x \approx 1$) the scattering is referred to as Mie scattering regime [Mie, 1908]. When the particle becomes larger, the scattered energy is increasingly concentrated in the forward direction. For $x > 50$, geometric optics methods have to be used to compute scattering properties.

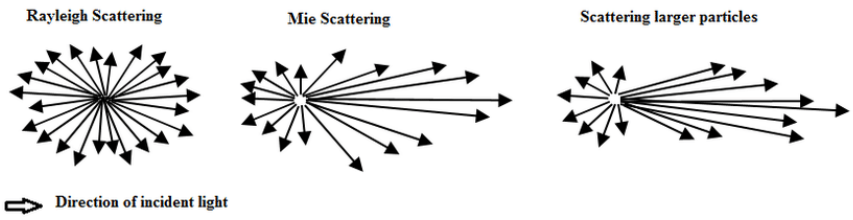

Figure 2.4: Scattering of electromagnetic radiation with a spherical particle at different wavelengths.

However, for the non-spherical particles (like ice crystals, aerosols) in the atmosphere the size parameter can not be defined. The optical properties of such non-spherical particles are computed using advanced computational methods, such as the T-matrix method.

Not only the clouds droplets, the gaseous molecules in the atmosphere also interact with radiation. Besides the major atmospheric gaseous components like molecular nitrogen and oxygen, the minor componenets play a crucial role in the interaction with

the radiation. These minor gaseous components of earth's atmosphere (e.g. CO_2, CH_4, O_3, and H_2O) are selective for both blocking and allowing the EM radiation to pass through it. For example, the upper atmosphere blocks 100% of the gamma rays, x-rays, and most ultraviolet light. These gases in the atmosphere also have unique spectral signatures. The range of wavelengths over which there is relatively less absorption of radiation by atmospheric gases are called *atmospheric windows*. The major windows are the visible window, from 0.3 to 0.9 μm; the infrared window, from 8 to 13 μm; and the microwave window, at wavelengths longer than $\sim 1mm$ as shown in figure 2.5. e.g., water vapour and carbon dioxide absorb from 2.5–3 μm and 5–8 μm.

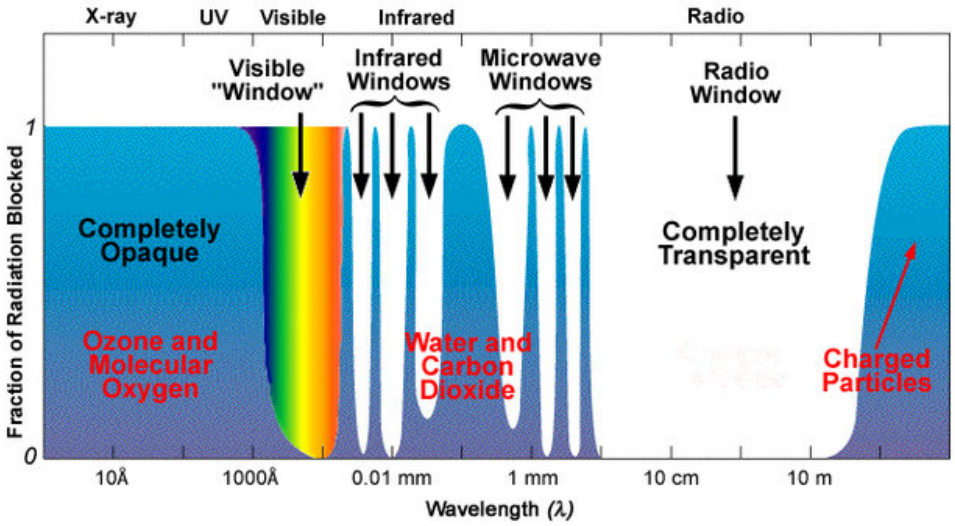

Figure 2.5: Atmospheric windows are regions of the spectrum where most of the radiations pass through the atmosphere. Figure source: `https://earthobservatory.nasa.gov/`

Taking advantage of these windows, we can observe the atmosphere at various wavelengths. The microwave window is particularly useful because of minimal atmospheric influences (absorption, scattering, atmospheric emissions) on microwave radiations and therefore commonly used for microwave remote sensing.

2.2.2 Earth's radiative equilibrium

Earth's radiation Budget at the top of the atmosphere (TOA) describes the overall balance between the incoming energy from the sun and the outgoing thermal (longwave) and reflected (shortwave) energy from the earth. This flow of incoming and outgoing energy is earth's energy budget. The earth system (atmosphere and surface) is heated by absorption of incoming solar radiations and cools by emitting longwave radiations to space. These thermal infrared radiation emitted from the earth surface are re-absorbed and re-radiated in the atmosphere many times by clouds and other greenhouse

gases(water vapour, CO_2 etc.), this process is known as the greenhouse effect. This is responsible for the temperate climate of earth, without it the average temperature of the planet would be about -19°C instead of 15°C.

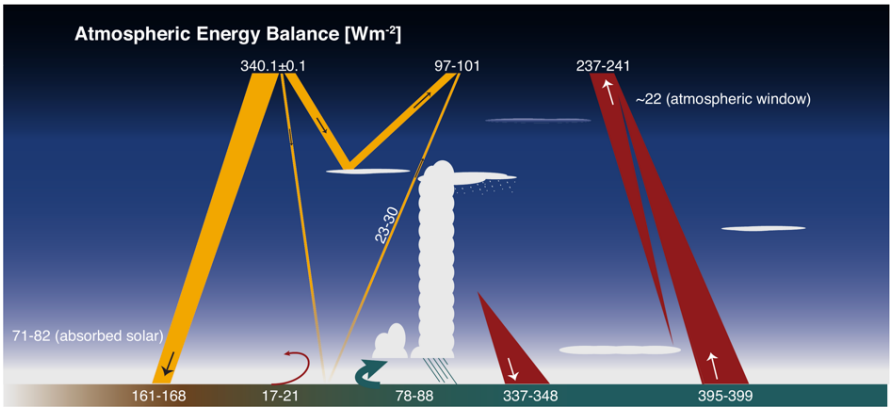

Figure 2.6: Earth's global and annual mean top-of-atmosphere (TOA) and surface energy budget. Figure source: Stevens, Bjorn and Schwartz, Stephen E. (2012)[Stevens and Schwartz, 2012]

Figure 2.6 illustrates the global energy balance, and the numbers represents annual and global averages of quantities that fluctuate substantially in space and time. The total instantaneous solar irradiance is 1360.8 Wm^{-2}, or 340 Wm^{-2} averaged over the global sphere. Out of the 340 Wm^{-2} received from the sun, about 100 Wm^{-2} is reflected by clouds and atmospheric aerosols (e.g. sulfates, nitrates), leaving 240 Wm^{-2} to be absorbed by atmosphere (71-82 Wm^{-2}) and surface (161-168 Wm^{-2}). Therefore, the planetary albedo (the fraction of SW radiation scattered back to space by the clouds, aerosols, and surface without being absorbed) is 0.29 [Stephens et al., 2015]. The radiative equilibrium at the TOA is balanced by emission of 237 Wm^{-2} LW radiation from the earth system. A fraction of this thermal IR radiation escapes directly to space through the atmospheric window (the spectral band between about 8 μm and 12 μm) when skies are clear. But, the presence of clouds reduces the amount of SW radiation reaching the surface and also contributes to additional IR radiation sent toward the surface. This effect of clouds on radiation is discussed in the next subsection.

2.2.3 Cloud radiative forcing

At TOA, the cloud radiative forcing (CRF) is defined as the difference between the downwelling (SW) and upwelling (LW) radiative fluxes in all-sky condition minus the difference in clear sky condition.

$$CRF = (F\downarrow - F\uparrow)_{allsky} - (F\downarrow - F\uparrow)_{clearsky} \tag{2.4}$$

The downwelling forcing ($F\downarrow$) is due to incoming SW radiations, and the upwelling ($F\uparrow$) is due to longwave cloud radiative effect, as all the wavelengths emitted by the earth do not reach into space. The atmosphere absorbs some of LW radiations while allowing other wavelengths to pass through.

The cloud radiative forcing due to SW and LW radiations are always in competition. In general, clouds with large optical thickness reflect most of the incoming shortwave radiation inducing a cooling effect, while clouds with a low cloud-top temperature trap outgoing longwave radiation inducing a warming effect [Hartmann et al., 1992]. Thus, net CRF depends both on the cloud optical thickness and the cloud top temperature.

Low-level clouds have high albedo, which means that these clouds reflect a part of incoming SW radiation back to the atmosphere. This cools the planet, and the size of the effect is determined primarily by cloud optical depth.

High level clouds have a weaker albedo. This means that solar radiation can penetrate deeper in the troposphere and heat the surface. These clouds also trap the IR radiation coming from the lower atmosphere. In the current climate, the global annual mean net CRF is about -17.1 Wm^{-2} [Loeb et al., 2009]. Therefore, the net effect of clouds is slightly cooling. However, a change in radiative forcing can modify the occurrence and the radiative properties of clouds, which can further lead to an enhanced or weakened cooling effect of clouds, thus exerting a radiative feedback.

2.2.4 Cloud feedback on climate

Reflection of solar radiations by clouds serves as a key feedback mechanism for climate change. A reduction in reflection of SW radiations due to low cloud induce positive feedback, while increase in cloud water content with warming induce negative feedback on climate [Stephens et al., 2015]. Clouds and aerosols contribute to climate change in a variety of ways. As shown in figure 2.7, the global radiative balance is affected by anthropogenic forcing agents such as greenhouse gases and aerosols. When a forcing agent alters internal energy flows in the earth system, it affects cloud cover and other climate system components, which in turn affects the global energy budget. In contrast to changes in the global mean surface temperature, which are slowed by the huge heat capacity of the oceans, these adjustments often occur within a shorter time span (generally a few weeks). These rapid adjustments are associated with changes in climate variables that are mediated by a change in global mean surface temperature. These variables further contribute to the amplification or dampening in global temperatures through their effect on the radiative budget [Change, 2014].

The representation of clouds is widely regarded as the largest source of uncertainty in estimates of climate sensitivity obtained by global climate models (GCMs) [Schneider

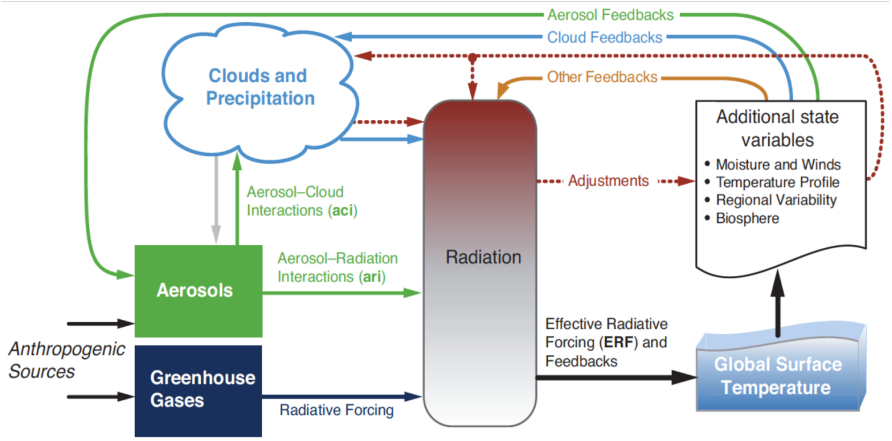

Figure 2.7: Overview of forcing and feedback pathways involving greenhouse gases, aerosols and clouds. Forcing agents are in the green and dark blue boxes, with forcing mechanisms indicated by the straight green and dark blue arrows. Figure source: [Change, 2014]

et al., 2017]. Among all the uncertainties in climate sensitivity estimates, representation of boundary layer clouds such as stratus and stratocumulus have a significant contribution, specifically in the sensitivity of boundary layer clouds to changing surface and PBL (planetary boundary layer, the lowermost part of atmosphere which is directly influenced by surface) properties [Bony and Dufresne, 2005].

Various climate sensitivity studies indicate that climate models often underestimate the low-cloud cover and over-estimate the occurrence of mid- and high-clouds above low-clouds furthermore, these biases can be caused due to inaccurate representation of cloud microphysical parameters [Nam et al., 2012]. Investigation of cloud processes leads to a better understanding of boundary layer clouds behaviour under changing atmospheric conditions have the potential to reduce the uncertainty in model predictions and climate sensitivity significantly [Bony and Dufresne, 2005].

In order to advance our knowledge about clouds-climate interactions, observations at multiple scales are required to verify the theories and hypotheses about clouds. Essentially, observations are the acquisition of information from a primary source or a snapshot of reality, which is analysed to validate or modify the concepts. The next chapter introduces general measurements techniques used for cloud observations.

Chapter 3

Instruments for cloud observation

Continuous observations of clouds are required to bridge the gap between the cloud microphysical properties and their interaction with other atmospheric process on local and global scales. These observations can help in the representation of cloud microphysical processes in climate projections. The ability to measure cloud properties has advanced considerably over recent years. A variety of instruments and methods are used in the observation of clouds, such as in-situ measurements and remote sensing instruments. All instrumentations have some weaknesses and strengths. Before selecting a sensor for a given application, it is essential to know the suitability of the instrument. The selection of platform for cloud observations is also dependent on a number of criteria, including the resolution with which cloud parameters must be recorded and the intended use of the observation. This chapter highlights in-situ and remote sensing instruments, as well as different platforms for collecting the cloud observations.

3.1 In-situ measurements

In-situ measurements are those made at the point where the instrument is located. These in-situ measurements bring information at very small scale and provide detailed information of different cloud characteristics. However, they are very localized and limited to specific time periods and regions, so they cannot provide a global view of cloud properties. In the early days of in-situ cloud measurement, oil-coated slides were exposed to cloudy air from an aircraft along a defined path length. Slides collide with cloud droplets and get absorbed in oil completely, preserving them for further study. Droplets colliding with these slides leave imprints which are proportional to the droplet size. However, droplets less than a few microns in diameter were not captured using this technique [Wallace and Hobbs, 2006].

Measuring meteorological information and various particles (e.g. aerosols) within the clouds, provides reliable data of cloud microphysical parameters and thermodynamic

structure of clouds at local scale. The in-situ cloud sensors from the early start of meteorological research have evolved from oil slides to sensitive cloud imaging and scattering spectrometers. Because such observations are generally expensive and provide only instantaneous information of the clouds, it is difficult to collect continuous measurements of clouds using this method [Gerber et al., 1994]. Nevertheless, these observations are crucial to improve the representation of clouds in various model simulations and also in the development and validation of retrieval products from the satellite, airborne and ground based observations.

These instruments can directly measure the particle size, shape, optical properties of the cloud particles. Other cloud properties like density and fall velocity need to be indirectly derived from the directly measured quantities. It is not possible to address all the available instruments for clouds observations in this thesis. Still, this chapter provides examples of commonly used in-situ techniques for the investigation of cloud physics. The monograph Baumgardner et al. [2017], provides a detailed explanation of different in-situ sensors and their measurement concepts with limitations. Some cloud microphysical parameters are measured in all phase of clouds (e.g., number concentration), therefore the sensors measuring such parameters will work for liquid, ice and mixed phase clouds, with the variation in their sampling volumes and possible accuracy. A few frequently used category of in-situ sensors for cloud observations are optical array probes, imaging probes, light scattering probes and hot wire systems. In this section, an outline of these techniques for collecting in-situ measurement of clouds are highlighted.

Optical Array Probes consist of a laser in one of the arms of the probe, which emits radiation of defined wavelength towards a photodiode array sensitive to the laser light fitted in the other arm. These elements record the decreased intensity of the laser beam due to the particle passing through the gap between arms. This difference in the intensity is used to characterize the shape and the size of the particles. The most common type of optical array probes is the 2D-C (Cloud) / 2D-P (Precipitation) probe that can sample particles with diameters between 50 and 100 μm and a maximum diameter of 1 mm. However, these optical array systems had some installation defects like diffraction effects, out-of-focus regions of the sampling volume, which is why these sensors are not used nowadays.

The Cloud and Precipitation Imaging Probes (CIP and PIP respectively) are also built on the same principle. More recently, more advanced probes were developed. For example, the 2D-S (Stereo) probe uses two laser beams crossing at right angles and illuminating two linear photodiode arrays [Lawson et al., 2006]. This configuration allows a better detection of small particles (e.g. $< 100\mu m$), leading to a better discrimination between small droplets and ice crystals, and can be used to give a three-dimensional

structure of particles that cannot be determined from a single shadow image of the particle.

Light scattering in-situ instruments quantify the size distributions of cloud droplets also using optical sensing discussed above. Currently, all devices used to determine the size and shape of individual cloud particles from aircraft involve use of optical detection [Baumgardner et al., 2011]. The Forward Scattering Spectrometer Probe (FSSP), Cloud Droplet Probe (CDP), and Cloud and Aerosol Spectrometer (CAS) etc., are in-situ probes based on the scattering of light by individual particles within a focused laser beam.

These in-situ cloud probes operate on the idea that the intensity of scattered light is directly proportional to the particle size. Theoretically, particle size can be estimated if the shape and refractive index of a particle and the wavelength of the incident light is known. The intensity of light scattered by a particle varies according to the angle with respect to the incident light. A laser produces monochromatic light, which is focused by lenses, and the light scattered by the particles is collected and sent to a photodetector for analysis. Mie theory [Mie, 1908] is applied to the scattered light from particle that pass through a focused light beam. The resulting electrical signal is digitized and processed in several ways. The primary difference in FSSP, CDP, CAS configurations is the angle at which the scattered light is collected, which defines the measurement characteristics of these instruments. These laser imaging probes have significant errors, for example, the FSSP suffers from 1) inhomogeneity across the length and width of the laser beam, which introduces sizing errors; 2) a limited response time of the detector electronics, which can lead to considerable underestimates of the droplet concentration; and 3) uncertainties associated with the calibration technique.

Imaging probes have the advantage of extracting information about the shape as well as its size by capturing an image of the particle. These probes capture images using optical arrays, which are fundamentally a microscope with a long working distance. Examples of few imaging probes are the Cloud and Precipitation Imaging Probes (CIP, CIP-Gray, and PIP), the Two-Dimensional Stereo spectrometer (2D-S), and the Cloud Particle Imager (CPI) etc.

Considering the cloud parameters under investigation, it is difficult to measure the wide range of cloud particles of various shapes, sizes and phase using a single instrument. The selection of in-situ sensors must depend on the range of conditions over which the measurements are made (e.g., temperature, altitude, LWC, drop size, length scale) and the accuracy required for those measurements. For example, the selection of particle size range from various single particle sizing probes for airborne cloud research can be made using the figure 3.1. The graph shows the approximate size ranges for the single particle sizing instruments, and star(*) denotes the instrument whose upper size range can be extended. Although some of the probes in the graph are no longer in use, new and

more advanced versions of the in-situ probes highlighted in red are considered recently developing technologies Baumgardner et al. [2011].

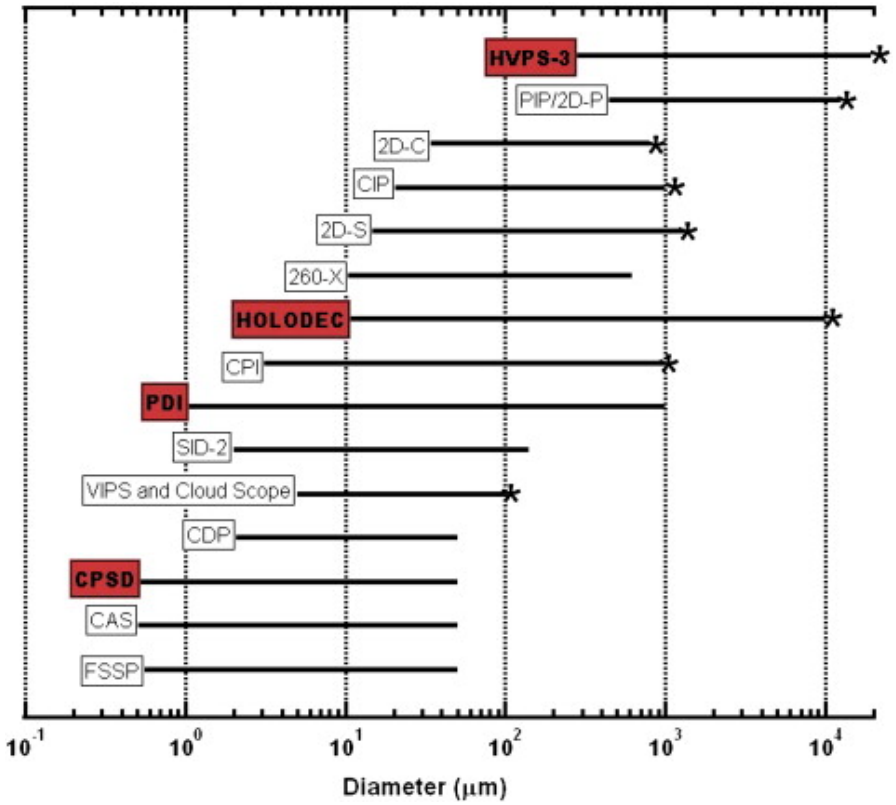

Figure 3.1: Size ranges for the single particle sizing instruments. Figure source: Baumgardner et al. [2011]

However, by measuring the particle size spectrum, the LWC can be determined by a simple integration of the spectrum. While considerable sizing errors can occur in the in-situ measurements, and when the diameters in a size bin are cubed to calculate volume, the resulting inaccuracy in the integrated liquid water content becomes significant. Thus, a probe developed specifically for direct measurement of LWC, such as a hot wire probe, is advised.

Hot wire devices are the instruments which expose an electrically heated wire to the air stream. When cloud droplets come into contact with the wire, they evaporate and reduce the resistance of the wire. In an electrical feedback loop, the resistance of the wire is used to maintain a constant temperature. The TWC (total water content, in case of mixed or ice clouds) is deduced from the amount of power delivered to the wire. LWC measurements from hot-wire probes are independent observations, which are also used for validation of measured cloud droplet size distributions from the same aircraft. Hot wire devices are also used for LWC measurement in ice and mixed phase clouds. Thus, hot-wire LWC measurement sensors and optical cloud probes are generally flown together. They can be used to constrain (closure) the mass-size

relationship for ice. However, hot-wire measurements have many limitations, including the following: (1) they are limited to non-precipitating circumstances; (2) they are inefficient for small droplets ($< 5\mu m$); (3) ice mass present in ice or mixed phase cloud can not be distinguished.

3.2 Remote Sensing

Remote sensing is the technique of acquiring information about a target without physically contacting it. This is accomplished by detecting the reflected or emitted energy from the target, followed by processing and analysing that information. Devices which detects and transform the emitted/reflected electromagnetic radiation into a signal are called Remote sensors. Fundamentally, the energy detected by these sensors in a particular part of the electromagnetic spectrum (SODAR is one of the exception, operates on sound waves), contains the information about the physical and/or thermodynamic properties of the target. The sensors either detect naturally emitted energy from the target or it emits an electromagnetic signal itself towards the direction of the target and then detects the fraction of the signal back scattered by the target. The first case is called passive remote sensors and the former is termed as active remote sensors. The regions of the electromagnetic spectrum which are directly used in remote sensing are visible, infrared and microwave ranges.

3.2.1 Passive sensors

Passive sensors are based on the concept of reception of energy that is naturally emitted, transmitted or reflected from the object. From the basic concept of ideal back body and Kirchhoff's law, it is known that the emission from a black body depends only on its temperature, and the higher the temperature of the body, the more it emits. By calculating the blackbody emission using Planck's Law, which expresses the radiance $B_\nu(T)$ emitted by a blackbody at absolute temperature T (in Kelvin) and frequency ν (in Hz)as

$$B_\nu(T) = \frac{2h\nu^3}{c^2} \frac{1}{(\exp(h\nu/kT) - 1)} \tag{3.1}$$

where h is the Planck's constant, c is the speed of light, and k is the Boltzmann constant. B_ν has dimensions of power per solid angle per area per frequency i.e. $W{\cdot}\mathrm{m}^{-2}{\cdot}\mathrm{sr}^{-1}{\cdot}\mathrm{Hz}^{-1}$. The radiances are converted into atmospheric and cloud parameters with the help of a radiative transfer model that relates the measurement to the different radiation processes (emission, absorption, scattering). Passive remote sensing utilizes either solar radiation reflected at the Earth's surface or scattered in the atmosphere, or thermal radiation emitted by the surface or the atmosphere, to derive atmospheric or surface properties. The passive systems operating in the visible range (430–720 nm) require daylight to see the whole atmospheric column. An example of passive remote sensing is the image from a weather satellite created from reflected visible light from the atmosphere. However, passive sensors operating in the infrared (NIR 750–950 nm and MIR 1580–1750 nm)

or microwave region depend on the emissivity of the body.

Multispectral sensors are generally used in passive remote sensing to measure the acquired quantity in multiple-band combinations. The bands include two or more wavelengths from the visible, IR, and microwave regions. For instance, observing clouds and the Earth's surface in regions known as atmospheric windows (in the visible and infrared 3–5 μm and 10–15 μm bands). Furthermore, by comparison of the observed brightness temperatures with those predicted by a radiative transfer model, optical and microphysical properties of clouds can be derived. Examples of standard passive remote sensing instruments used in atmospheric measurements include radiometers and sounders.

Radiometers measure the intensity of electromagnetic radiation in a specific band of wavelengths. The principal sources of atmospheric microwave emission and absorption are water vapour, oxygen, and cloud liquid. The spectral radiance is measured as the brightness temperature, which is linearly related to the kinetic temperature (ability to emit radiation) of the body. A radiometer is usually distinguished by the region of the spectrum it covers, such as visible, infrared, or microwave. Passive microwave radiometers have been used to derive temperature and humidity profiles of the Troposphere. Multispectral radiometers can detect the radiation in multiple bands suitable for remote sensing of certain parameters like sea surface temperature, cloud characteristics, vegetation and many more. Microwave radiometers measure emitted microwave radiation, expressed in terms of brightness temperature, which can be related to the column-integrated water content (liquid water path, LWP) and precipitation rate. However, little information about the spatial structure can be retrieved.

Sounders make use of all three radiative transfer phenomena, namely absorption, scattering, and emission. Atmospheric sounders generally make passive measurements of the distribution of IR or microwave radiation emitted by the atmosphere, from which vertical profiles of temperature and humidity through the atmosphere are obtained. The sounders differ from radiometers by estimating temperature and humidity profiles rather than path integrated values. Oxygen or carbon dioxide is usually used as a 'tracer' for the estimation of temperature profiles, since they are relatively uniformly distributed throughout the atmosphere, so atmospheric temperature sounders measure radiation at wavelengths emitted by these gases. For humidity profiling, either IR or microwave wavelengths specific to water vapour are used. Microwave sounders have the ability to sound through cloud and hence offer nearly all-weather capability. However, their spatial resolution (both vertical and horizontal) is generally lower than the IR instruments.

3.2.2 Active sensors

Active sensors, on the other hand, provide their energy source for illumination. In particular, the sensor actively transmit the EM radiation and measures the backscatter returned to it. The backscattered signal carries information about different properties of the target, and the travelling time of the pulse (or equivalent) allows an accurate estimate of the distance of the target. Active sensors conveys information about the surface characteristics of the target.Besides wavelengths from the sun, these sensors can evaluate the target in other wavelengths, such as microwaves. Thus, better control over target illumination is possible in active remote sensing. However, the energy required to illuminate the target sufficiently is quite large. The radiation-particle interaction phenomena in the atmosphere introduced in chapter 2 are significant in active remote sensing. Examples of active sensors frequently used for atmospheric measurement are lidar, radar, scatterometer etc. The following section highlights lidar and radar instruments in detail.

Lidar

These systems emit a laser pulses of specific wavelengths in the atmosphere. This pulse is scattered by the atmospheric particles and undergo attenuation, and the attenuated backscattered signal is measured. Lidar wavelength is mainly located in the near UV (355 nm), visible (532 nm) and near infrared (1064 nm) part of the electromagnetic spectrum. As shown in the basic schematic of lidar in figure 3.2, an optical assembly (usually a telescope), collects part of the scattered radiation and the detected signal is then amplified, digitized and processed to retrieve atmospheric parameters. The lidar signal is scattered by the molecular constituent of air, aerosols and cloud particle and the intensity of backscattered depends on the integral extinction along the way back and forth.

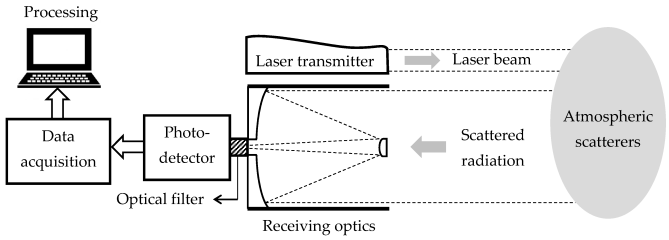

Figure 3.2: Basic schematics of a lidar system. Figure source: Comerón et al. [2017]

The backscattering phenomenon is parametrized by the atmospheric backscatter coefficient, $\beta_\lambda(m^{-1} \cdot sr^{-1})$, and total backscatter is the sum of the contribution of the air molecules and the cloud particles in the sampled volume: $\beta_\lambda = \beta_\lambda^{mol} + \beta_\lambda^{par}$. The apparent

backscatter measured by lidar is a function of the two-way transmission coefficient of the atmosphere along the path:

$$\beta_a(R) = \beta(R)e^{-2\int_0^R \alpha(z)dz} \tag{3.2}$$

where α is the extinction coefficient in m^{-1} and R is the atmospheric path length in m. Note that this equation doesn't account for multiple scattering.

However, the lidar typically measures the attenuated lidar signal $P_\lambda(R)$ as a function of distance between lidar and target R:

$$P_\lambda(R) = \frac{K_\lambda}{R^2}\beta_a(R,\lambda)O_\lambda(R)P_{\lambda_0}(R)$$

where $P_\lambda(R)$ is the backscattered power (in W) received from range R, P_{λ_0} is the emitted power, $O_\lambda(R)$ is the overlap function and K_λ is the lidar system constant. The backscattering coefficient β and the extinction α depend on the scattering properties of the particles and the molecules. They are linked by a parameter S called the lidar ratio (or extinction-to-backscatter ratio) expressed in steradian (sr) which is defined as follows:

$$S = \frac{\alpha}{\beta} \tag{3.3}$$

Lidars are used to retrieve the aerosol profile, boundary layer dynamics, and cloud base height, particularly when lidar is pointing vertically upwards. But, this instrument has the disadvantage of being strongly attenuated by cloud droplets. Thus, a ground based vertically pointing lidar usually cannot provide information about the upper limit of clouds or fog layers. However, they provide more accurate measurements of cloud base heights in the lower altitude. Cloud base heights are commonly measured with zenith-pointing laser ceilometers, a type of lidar. This device is frequently used to determine cloud ceilings (base) at airports and therefore called ceilometer. It works by emitting a laser beam (infrared or ultraviolet transmitter) and the return from the clouds base are detected by a photocell in the receiver.

The equations presented in this section, are described considering the elastic lidar for rayleigh scattering. Mie scattering is referred in the elastic scattering from spherical particles whose size is comparable to or larger than the wavelength of the laser. Note that the backscattered lidar signal typically consists of elastic scattering from both molecules and particles and also of inelastic scattering due to rotational Raman transition in molecules. Inelastic scattering occurs when the molecule (or atom) first absorbes the incident wave and uses the incoming energy to change its rotational or vibrational state. This results in a change in the frequency of the scattered wave. Therefore, Raman lidar systems detect signals at different wavelengths.

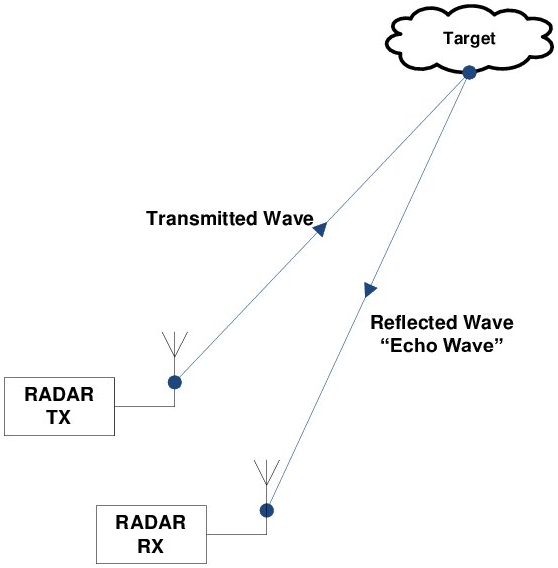

Figure 3.3: Radar Schematic

Radar

Radar system works in much the same way as lidar, with the big difference that it uses radio waves ($\nu < 300GHz$) instead of laser light. The antenna system produces and emits the electromagnetic waves of a defined wavelength, and the characteristics of radar are essentially determined by the properties of how the radio wave interacts with a physical

object (e.g., rain, cloud droplet, airplane, etc.). The figure 3.3 shows a typical schematic of a radar where a transmitter (TX) or antenna transmits the electromagnetic wave towards the target, and the reflected echo is collected at the receiver (RX) end where the signal is amplified, and information about the target is retrieved. Only a fraction of emitted energy is back-scattered by atmospheric constituents such as raindrops, clouds; therefore, meteorological radar receivers are very sensitive instruments.

The choice of radar frequency depends on the application requirements. The radar frequency is actually a frequency band which is designated by a code letter. For example, S-band (2–4 GHz), C-band (4-8 GHz) and X-band (8-12.5 GHz) are used for meteorological applications related to precipitation, hail, and shorter-range hydrology. In order to observe clouds, shorter wavelengths than rain radars are used. Radars operating at millimetre wavelength such as K-band (18-27 GHz), K_a-band (27-40 GHz), and W-band (75-110 GHz) are more sensitive to small cloud droplets and ice-crystals [Lhermitte, 1990]. In particular, radars operating at 35 GHz (8.7 mm wavelength, K_a-band) or 95 GHz (3.16 mm wavelength, W-band) are called cloud radars, because the atmospheric attenuation related to water vapour and oxygen reaches a local minimum at these frequencies [Liou, 2002]. However, due to short wavelengths, K_a and W-band

radar signals are prone to get attenuated due to rain droplets in the path.

While travelling through the atmosphere, the power density decreases due to extinction by particles in its path. Consider a target at a distance R, then the average backscattered power $P_r(R)$ for the transmitted power P_t is given by:

$$P_r(R) = \frac{C}{R^2} L \sigma_v \tag{3.4}$$

where σ_v the backscattering radar cross-section integrated over a unit volume, L is the coefficient linked to attenuation and C is called radar factor, a function of transmitted power P_t, antenna geometry, and wavelength. In the equation (3.4), σ_v and L are the parameters dependent on atmospheric composition (gases, hydrometeors etc.).

The backscattering cross-section σ_v is a quantity that indicates the part of energy which is scattered back towards the direction of incidence. For a hydrometeor, it is a function of the diameter D (and shape), its refractive index m and the wavelength λ of the interacting radiation, i.e., $\sigma_v(D, m, \lambda)$. Mie [1908] proposed a solution for cross-section of homogeneous spherical particles using Maxwell's equations, given as

$$\sigma = \frac{\lambda^2}{4\pi} \left| \sum_{n=1}^{\infty} (-1)^n (2n+1)(a_n - b_n) \right|^2 \tag{3.5}$$

where the Mie coefficients a_n and b_n are spherical Bessel functions depending on m and size parameter $2\pi r/\lambda$. This theory provides an accurate description of the problem, but comes at a high computational cost. The Rayleigh approximation is a representative and valid approximation for different type of scattering calculations. Since liquid cloud particles are much smaller than mm wavelengths, and a simplification of equation (3.5) therefore leads to the Rayleigh approximation ($2\pi r/\lambda << 1$) for spherical droplets, then σ_v can be expressed as

$$\sigma_v = \frac{\pi^5}{\lambda^4} |K|^2 D^6 \quad \text{with} \quad K = \frac{m^2 - 1}{m^2 + 2} \tag{3.6}$$

where the dielectric constant $|K|^2$ depends on the complex index of refraction m. However, the Rayleigh approximation has a significant limitation. It is only valid for small particles compared to the wavelength, and the reason can be seen in figure 3.4. At most of the radar wavelengths, the Rayleigh approximation can be used for cloud particles and small hydrometeors. But with larger meteorological particles (e.g. large ice crystals, hail), the exact Mie solution should be considered because the backscattering cross-section shows an oscillatory behaviour. For even bigger objects, the scattering cross-section of the target approaches their geometric cross-section. It should be noted that both the Mie and the Rayleigh regime discussed here are valid for spherical particles

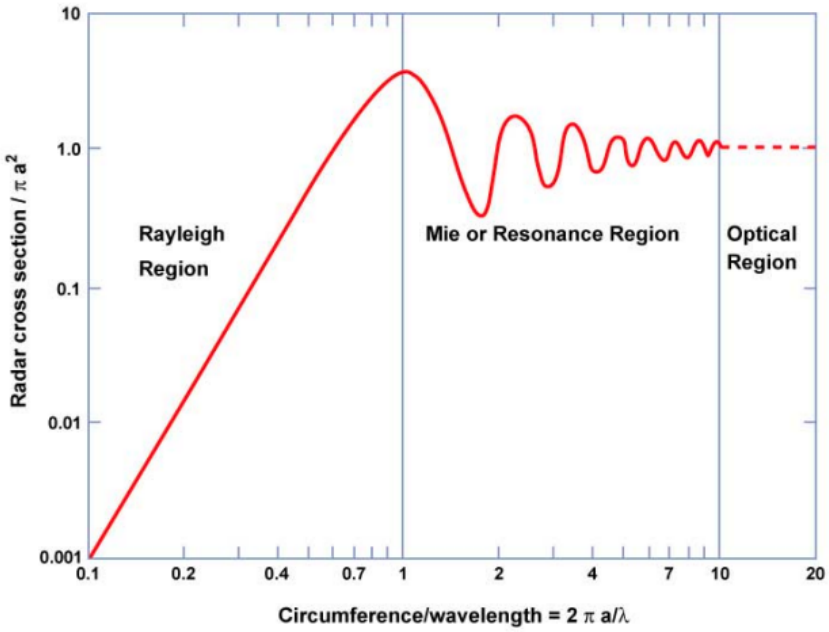

Figure 3.4: Normalized back scattering cross-section $\sigma/\pi a$ as a function of size parameter $2\pi a/\lambda$ for sphere, considering a is the radius of the sphere.

only. In case of non-spherical particles, a computationally much more expensive method called T-Matrix method has been frequently used to model the scattering properties of particles. Another method to estimate scattering properties for large and complex particles is the discrete dipole approximation (DDA) method. DDA method splits up a single particle into a finite array of polarizable points, for which the dipole moments are estimated in response to the local electric field. However, liquid-phase clouds mainly consist of small spherical liquid water droplets and hence the T-matrix and DDA methods goes beyond the scope of this thesis.

The average power backscattered by the particles distributed in a volume V is proportional to radar reflectivity, η which is actually the sum of back scattering cross-section of individual particles over the unit volume. The radar reflectivity η is a characteristic quantity of the target, and its definition does not imply any assumption on the scattering medium. However, in case of standard mereological radars, the condition of Rayleigh approximation remains valid for most of the atmospheric targets except hail. Therefore, radar reflectivity according to Rayleigh approximation becomes

$$\eta = \frac{1}{V}\sum_{V}\sigma_i = \frac{\pi^5}{\lambda^4}|K|^2\int_{D_{min}}^{D_{max}} D^6 n(D)dD \tag{3.7}$$

where the integral is called radar reflectivity factor Z, which represents the average characteristic of the scatterers distributed in the volume and Z is expressed in $mm^6 \cdot m^{-3}$ as

$$Z = \int D^6 n(D) d(D) \tag{3.8}$$

where $n(D)$ is the particle size distribution, which tells us how the droplets of clouds are distributed across the range of sizes. This parameter will be described in detail in section 4.1.

The radar reflectivity factor Z is independent of wavelength, which makes it easier to compare measurements obtained with different radars, and it is usually given in units of $dBZ = 10\log_{10}(Z)$ due to its large dynamic range. However, equation 3.8 is true only if the Rayleigh approximation is valid. If the scattering volume does not satisfy the condition of Rayleigh approximation, the particle in the radar volume are characterized by the equivalent reflectivity factor Z_e, which is equal to the reflectivity factor of liquid spherical particles producing the same signal with in Rayleigh approximation.

$$Z_e = \frac{\lambda^4 |K_w|^2}{\pi^5} \eta \tag{3.9}$$

where $|K_w|^2$ is the dielectric factor of water and η is radar reflectivity as defined in equation 3.7.

However, in case of liquid cloud droplets, the wavelength of the radar signal is large enough and therefore the Rayleigh regime will remain valid. In the last few decades microwave radars have been developed, which can detect all types of non-precipitating clouds well before large hydrometeors are formed up to distances of a few kilometres. As the radar backscattering cross-section is inversely proportional to fourth power of radar wavelength (λ) (refer equation 3.6), and so does the backscattered power. Hence, the shorter wavelengths indicate greater sensitivity of the radar, this means that these radars can detect smaller particles. However, higher sensitivity also signifies that the signal will be affected or attenuation by different particles in the atmosphere. The cloud radar operating at $95GHz$ is capable of penetrating dense and thick cloud layers, allowing a complete scan of deep clouds. A key feature of the cloud radar is the ability to provide information of multiple cloud layers, even if the lowest layer completely obscures the sky.

3.3 Instruments used in this study

In this thesis, a method to estimate the microphysical characteristics of low-level clouds and fog is presented (in chapter 5) using a cloud radar and microwave radiometer synergy. Observations from BASTA cloud radar colocated with the HATPRO (Humidity And Temperature PROfiler) microwave radiometer at SIRTA observatory and SOFOG-3D

field experiment are utilized. The fundamental concept of these remote sensing instruments is already introduced in this chapter, and this section describes these instruments and their capabilities in further depth. While the SIRTA observatory and SOFOG-3D experiment observation sites are detailed in section 3.5. The retrievals of the cloud microphysical parameter using the mentioned synergy are compared with measurements from an in-situ sensor called CDP. To ensure that this section covers all instrumentation utilized in this research, the in-situ sensor is also described here.

3.3.1 BASTA cloud radar

A $95GHz$ FMCW radar called BASTA [Delanoë et al., 2016] developed in LATMOS (Laboratoire Atmosphères, Observations Spatiales) is operational at SIRTA observatory since 2010 (shown in figure 3.5). In addition to its first prototype operational at SIRTA, several other BASTA radars are working over different locations around the globe.

Figure 3.5: A vertically pointing BASTA cloud radar at SIRTA

This Doppler cloud radar uses the frequency-modulated continuous wave (FMCW) technique, rather than pulses, making it less expensive than standard cloud radars by reducing the emitted power. The principle of FMCW radar is same as the radar principle discussed in the previous section, except that the radar transmits the continuous wave of energy whose frequency varies between $F_0+\Delta f$ and $F_0-\Delta f$ with a constant time period T_m with F_0 as the central frequency and Δf is half of the frequency band. The wave, which is returned by a target situated at a range R, is received after time $\Delta t = 2R/c$ where c is the speed of wave propagation in the given medium. The radar returned

signal is convolved (mixed) with the transmitted signal, and the beat frequency f_b can be defined such that

$$f_b = 2\Delta f \times \frac{\Delta t}{T_m} \tag{3.10}$$

The acquisition of the signal occurs only for half of the total time period T_m to avoid echo from other chirp, which costs 3 dBZ loss in sensitivity in BASTA. The range resolution is calculated as

$$R = \frac{c}{2 \times 2\Delta f} \tag{3.11}$$

The advantage of FMCW radar is that the range resolution is inversely proportional to the frequency modulation, and hence can be regulated. To increase it, it is sufficient to increase the value of Δf. The detailed descriptions of BASTA cloud radar and its operating characteristics can be found in Delanoë et al. [2016] and `http://basta.projet.latmos.ipsl.fr/`. A ground-based vertically pointing BASTA radar measures radar reflectivity and Doppler velocity of the atmospheric targets at four different resolution modes depending on the specific application. In particular, the 12.5 m vertical resolution mode is dedicated to fog and low level clouds and is limited to 12 km range height. The 25 m mode is suitable for liquid and ice mid-tropospheric clouds and covers the vertical extent from minimum range of 40 m to 18 km. Furthermore, the 100 m resolution is ideal for optically-thin high-level ice clouds with maximum detectable range of $24km$. The portability and compact size makes BASTA a powerful research tool that has been deployed on various platforms, including ships, aircraft etc. during various field campaigns (e.g., EUREC^{4}A (eur), Sea2cloud (sea), SOFOG-3D (sof) etc). Some Doppler cloud radar can also record the radar Doppler spectrum of the return radar echo over a range of sampled Doppler velocities. However, the Doppler spectrum is not operationally available with BASTA, and we are investigating ways to enhance this capability, in order to perform a spectral analysis of the signal.

Cloud radar calibration is necessary to perform the retrieval of physical cloud parameters from the measured backscattered power. As the radar consists of large number of components, the internal calibration of radar is to determine all the instrumental constants and their gain and losses. Unfortunately, it is quite challenging to determine the exact power budget through each electronic components and their gains. Because different radar configurations require different approaches, a common approach is the external calibration, which characterize the complete system at once. This approach is based on the idea of an external target with known reflectivity factor at a known distance should give the expected backscattered power from radar. Then the calibration constant is defined as the difference in reflectivity between the measured reflectivity and the actual one. The calibration accuracy of BASTA is obtained about 2 dB from the

Figure 3.6: A multichannel HATPRO Microwave radiometer.

uncharacterized reference target. The detailed method used to calibrate BASTA cloud radar is elaborated in Delanoë et al. [2016] and Toledo et al. [2020].

3.3.2 HATPRO microwave radiometer

A 14-channel HATPRO (Humidity And Temperature Profiler) MWR manufactured by Radiometer Physics GmbH (RPG) is operational at SIRTA observatory. Figure 3.6 shows a picture of 14 channel HATPRO MWR of G4 series.

HATPRO MWR is a passive instrument, converting the naturally emitted downwelling radiative energy emitted from the atmosphere within two spectral bands: the first one focuses on the 22.24 GHz water vapour absorption band up to 31 GHz while the second one is centred on the 60 GHz oxygen complex band (51–59 GHz). Through the use of calibration coefficients, detected intensities are then directly converted into brightness temperatures. A retrieval technique is then needed to convert the brightness temperature spectra into vertical profiles of temperature, humidity as well as liquid water path. In general, statistical methods (linear, quadratic regressions or neural networks) trained from simulated MWR observations from a database of radiosoundings or model analyses are used [Cimini et al., 2006]. Optimal estimation retrievals combining an *a priori* estimate of the atmospheric state with observations through an iterative process can also be used [Martinet et al., 2020]. In this study, LWP retrievals based on MWR observations have been retrieved through quadratic regressions trained from a database of radiosoundings for SIRTA while for SOFOG3D, neural networks trained from AROME short-term-forecasts have been used. MWRs are only sensitive to the total liquid water content present in the vertical profile [Ware et al., 2002]. Humidity profiles can be

retrieved with a limited vertical resolution due to the smoother weighting functions for K-band channels. Temperature profiles show a better vertical resolution, which can be improved through the use of different elevation angles (generally from 90 to 5.4° above the ground).

If there is a single layered liquid cloud, MWR thus provide a direct estimate of the LWP for the cloud column. The LWP measurements of the column are unaffected by ice clouds above liquid clouds. The time resolution of LWP measurements used in this study is 1 second, with brief interruptions due to boundary layer scans. The missing measurements during boundary layer scans are interpolated to the BASTA observation frequency. The uncertainty of the MWR for LWP is expected to range between 10 gm^{-2} and 20 gm^{-2} [Crewell and Löhnert, 2003, Marke et al., 2016] particularly dependent on the absolute calibration errors of MWR and uncertainties in retrieval algorithms.

3.3.3 Cloud Droplet Probe (CDP) on tethered balloon during SOFOG-3D experiment

The tethered balloon mounted with in-situ sensor called Cloud Droplet Probe (CDP) which is designed to measure cloud droplet size distribution from 2 μm to 50 μm. The CDP probe housing contains the forward scatter optical system, which includes a laser heating circuit, photodetectors, and analogue signal conditioning and an appropriate data system can also calculate various other parameters including particle concentrations, effective diameter (ED), Median Volume Diameter (MVD), and LWC [Lance et al., 2010]. This instrument (shown in figure 3.7) is designed and commercialized by Droplet Measurement Technology and the specifications are given in table 3.1. As introduced in section3.1, the operation of the probe is based on the Mie scattering theory [Mie, 1908]. In particular, when a cloud droplet passes through the laser beam, the photodetectors of the probe measure the intensity of the forward scattered light over the angles 4-12°. Then, the light is equally distributed (by a beam splitter) between the qualifier, which recognize a countable particle, and the sizer, which is used for the particle size estimation. The sampling rate of CDP was 10 sec during SOFOG-3D campaign.

Table 3.1: Specifications of in-situ cloud droplet probe mounted on tethered balloon

Laser	658 nm, up to 50 mW
Measured Particle Size Range	2 μm – 50 μm
Typical Sample Area	0.24 mm^{-2}
Number Concentration Range	0 – 2,000 cm^{-2}

CDP probes are associated to sizing and undercounting errors, which depend on both the diameter of the droplet and its position inside the sampling area. With various

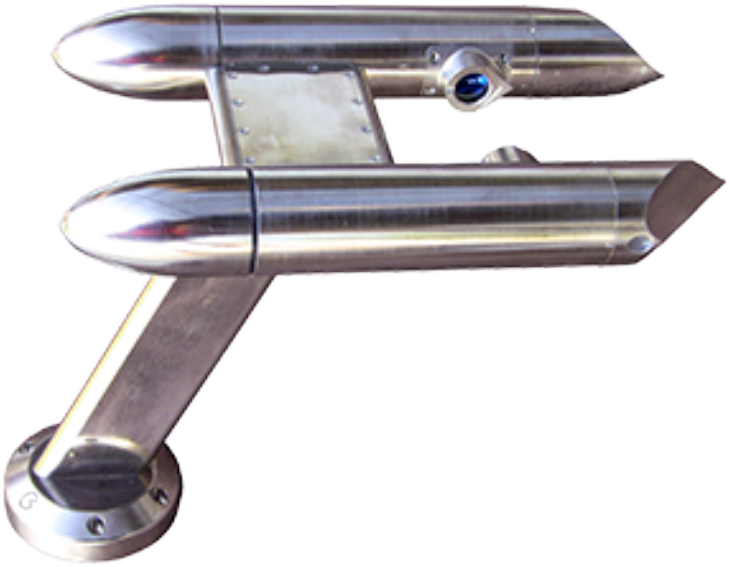

Figure 3.7: A CDP probe. Image courtesy (https://www.dropletmeasurement.com/product/cloud-droplet-probe/)

upgrade in the electronics and the design of the probe, 27% undercounting and 20% to 30% oversizing bias at ambient droplet concentrations of 500 cm^{-3}, were reported [Lance, 2012].

3.4 Observation platforms

The sensors are mounted on various platforms to acquire information about a target under investigation. Based on the altitude above the earth's surface, the platform can be classified as the ground-based (including shipborne), airborne, and space-borne platforms. In this section, we will just give a few examples as illustration.

Ground-based platforms like tripods, cranes, ground vehicles and towers are common examples. Ground-based instruments are frequently used to monitor atmospheric phenomenon for long term. These types of platforms are relatively inexpensive, stable, and due to their low altitude, provide high-resolution data of the lower atmosphere. Sensor quality control of instruments on ground-based platforms are considerably easier. Multiple instruments can be co-located to measure different atmospheric parameters.

Airborne platforms include airplanes, helicopters, UAVs, high-altitude aircraft, and free-floating and tethered balloons. The airborne configuration can have several advantages, as one can easily target a system and follow its development and motion. This special viewing geometry can also allow a better description of the cloud top than ground based instruments (being crucial when instruments are very sensitive to attenuation in the low troposphere). A research aircraft can be equipped with a variety of active and passive remote sensors, as well as in-situ probes. For example, RASTA (RAdar SysTem Airborne) is a $94GHz$ (W-band) Doppler cloud radar and multi-wavelength lidar that can be deployed on a research aircraft (e.g., Falcon 20) to investigate about cloud, aerosol, and convection properties. RASTA can be operated in several configurations, the 6 antennas configuration allows one to retrieve 3D cloud dynamic above and below the aircraft. The RALI (RAdar and LIdar) project combines RASTA and a triple-wavelength dual-polarization lidar, with high spectral resolution and Doppler capability at 355 nm, for characterization of the macrophysical, microphysical, radiative, and dynamical properties of clouds, aerosols, and convection. This project began in 1993, and additional information about this aerial platform and observation system may be found at `http://rali.projet.latmos.ipsl.fr/`. Such aircraft based airborne platforms can be expensive.A UAV, on the other hand, is a small remotely piloted aircraft. It is intended to be inexpensive, a modest payload capacity, and operate without or with a short runway. Cameras, infrared sensors, radar can be mounted on UAV. It communicates through the satellite, and an onboard computer controls the payload and stores data from sensors. The tethered balloon platform is an airborne platform which includes a tethered balloon filled with helium gas and a rack for mounting electronic equipment and instruments under the balloon. Depending on their size and capacity, tethered balloons can even have a payload of 200 kg. Tethered balloons as a sensor platform have many advantages, such as low operating cost and high resolution

profiling of the meteorological and radiative properties over the entire PBL from the surface to its top. The balloon can remain at one location for hours, thus is able to provide time series of PBL variables, which is very important for studying boundary layer transition, surface-air interaction, and PBL process including aerosol and trace gases parameterization. With appropriate sensor packages, it can provide continuous monitoring of air pollutants and portable weather stations below 1000 m. However, the use of tethered balloons is limited to the lowermost 1–2 km levels in light wind and in areas with little air traffic.

Space borne platform Since airborne platform cannot fly for long time period (i.e., months or years), space borne platforms are very useful in remote sensing to provide long term and wider view of the target area. The satellites are used for the space borne remote sensing, which moves in their orbit around the planet. The type of sensor on the platform and the orbit that the platform travels is based upon the type of monitoring and data collection needed. One of the main interest of space borne platforms is to have long-term records of global observations, which can be used to assess weather and climate prediction models. As spaceborne sensors are well placed on stable platforms, they have fewer problems with distortion than airborne sensors. The benefits of using space borne remote sensing includes broad coverage, repeated coverage of an area of interest, lower cost per coverage area. Weather satellites have completely transformed weather analysis and forecasting. The constellation of satellites called *A-Train* (`https://atrain.nasa.gov/`) includes different passive and active sensors for monitoring clouds and aerosols properties. One of the space borne millimeter-wavelength cloud radar is the CloudSat [Stephens et al., 2002] launched in 2006, which has a vertical resolution of 500 m. However, low temporal and spatial resolution is the primary draw back of satellite based sensors.

3.5 Observation sites and field campaigns used in this study

As described above, ground based remote sensing overcomes the limitation of low spatial resolution captured by satellite based sensors. Because I am focusing on low level clouds, ground based remote sensing instruments provides high spatial and temporal resolution of clouds properties, especially for low-level clouds being closer to them with minimum influence of atmospheric noise. Observations from multi-instrument like cloud radar, lidar, radiometer etc. collocated at atmospheric measurement site for example SIRTA (France), JOYCE (Germany), Cabauw (Netherlands), Chilbolton (UK) etc., provides valuable insights of fine scale atmospheric processes and cloud microphysical properties. In this section, I describe the observation sites and instrumentation used in my research. Data from SOFOG-3D field campaign, as well as the French observatory near Paris are used in this research, and these observation sites are outlined in the next section.

3.5.1 SIRTA

Figure 3.8: SIRTA observatory. Image courtesy (`https://sirta.ipsl.fr/index.html`)

SIRTA (Site Instrumental de Recherche par Télédétection Atmosphérique) is a multi-instrumental atmospheric observatory located 20 km in the south of Paris, at the university campus of École Polytechnique, in Palaiseau. The area round the observatory is a semi-urban environment with trees, fields, houses, and some industrial buildings. Many atmospheric variables have been continuously recorded since 2002 [Haeffelin et al., 2005]. The altitude of the site is 156 m above mean sea level and various ground based instruments are set up on the platform as shown in image 3.8. Additionally, a 30 m mast

equipped with sensors for measurement of turbulent and radiative fluxes is also setup at SIRTA. Sensors for temperature, humidity and pressure measurement are installed at 2 m above ground, as well as a wind vane and anemometer installed at 10m above ground. SIRTA has a surface radiative flux station to monitor the downwelling solar and infrared components of the surface radiation budget. A sonic anemometer and a closed-path infrared gas analyser are installed to measure turbulent sensible and latent heat fluxes at 2 m with the eddy covariance method. At depths of 5, 20, and 100 centimetres, the ground heat flux is also monitored. Soil temperature and moisture are measured at different levels of soil, and a thermometer monitors the skin temperature of ground. A multi-wavelength sun-photometer, is exploiting the visible and near-infrared end of the spectrum to monitor aerosol properties at SIRTA. In addition to surface measurements, radiosondes launches at around 11 and 23 UTC from the Trappes Météo-France station which is located 15 km west of SIRTA, are collected on a regular basis to provide atmospheric temperature and humidity profiles.

As already highlighted in the earlier sections, the advantages of ground-based remote sensing instruments in terms of their ability to provide continuous observations make them particularly well suited for monitoring fine scale processes involving complex interactions between clouds, aerosols, and radiative and dynamic processes. SIRTA observatory also houses remote sensing instruments such as radars, lidars, and radiometers. A CHM15K ceilometer operating at 1064 nm produces a 15 m resolution vertical profile of (attenuated) light backscatter. This wavelength is extremely sensitive to cloud droplets, allowing for reliable cloud detection. Since the cloud rapidly attenuates the ceilometer beam, further characterization of the cloud profile above the cloud base is performed by the 95GHz cloud radar named BASTA. A 14-channel HATPRO microwave radiometer (MWR) is also operational since 2010 which provides brightness temperature measurements in 7 oxygen and 7 water vapour bands. The vertically integrated liquid water path (LWP) and integrated water vapour (IWV) of the whole atmospheric column, as well as profiles of temperature and humidity up to 10 km can be retrieved from these measurements. The HATPRO MWR and vertically oriented BASTA radar both are operational at SIRTA since 2010, and these instruments are detailed in the section 3.3. SIRTA has also deployed a fog monitor FM-120 (Droplet Measurement Technologies) to characterize fog properties. Individual droplets are counted and sized using a forward scattering probe inside a compact measurement chamber that samples a steady flow of air using active ventilation.

Many research activities focusing on the dynamics and properties of clouds at different levels are utilizing the observations and the instrument synergies offered from SIRTA. More information about the observations and the data set from SIRTA can be found at `https://sirta.ipsl.fr/`. The observations of clouds acquired by remote

sensing devices at SIRTA between November 2018 and May 2019 are used in this study.

3.5.2 SOFOG-3D

SOFOG-3D stands for SOuth west FOGs 3D experiment for processes study and the related field experiment was conducted between October 2019 to March 2020 in the South-West region of France, which is particularly prone to fog occurrence. Because, aviation sector all around the world is severely hindered due to fog and hence observations and specific research for fog is necessary to improve fog forecast. The primary goal of this field experiment was to advance the understanding of fog processes by exploring both horizontal and vertical variability of fog layers, and finally improve fog forecasts by numerical weather prediction (NWP) models.

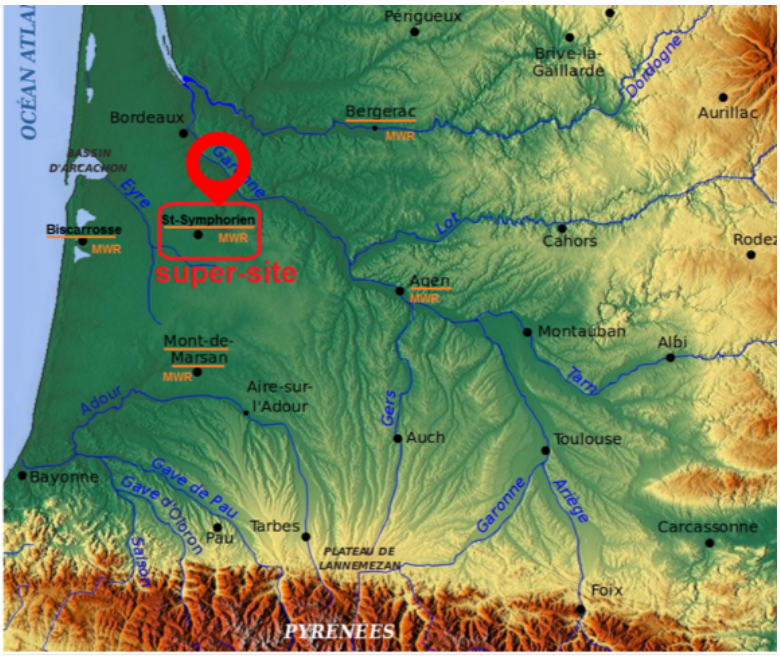

Figure 3.9: SOFOG-3D campaign super site

In order to provide a 3D characterization of fog through detailed observations of dynamics, radiation, microphysics and surface fluxes, a number of in-situ and remote sensing instruments were deployed to collect the observations of various characteristics of fog. The supersite is located at Saint-Symphorien commune of France and is centred at 44°24'44.5 N, 0°35'51.5 W covering a surface of around 5 km as shown in figure 3.9. Simultaneous measurements from various remote sensing instruments like BASTA cloud radar with scanning capability as well as vertically pointing, HATPRO Microwave radiometer, Doppler lidar were collected to better understand the spatiotemporal evolution of fog. In addition to the remote sensing instruments on the super site, detailed

measurements of meteorological conditions, aerosol properties, fog microphysics, water deposition, radiation budget, heat and momentum fluxes are collected to provide 3D structure of the boundary layer during fog events. A 50 m tower equipped with sensors to measure the turbulence in the vertical structure of boundary layer was installed. During the field campaign, in-situ observations from radiosonde tethered balloon and Unmanned Aerial Vehicle (UAV) fleet were collected on a regular basis. Around the super-site, a larger domain of 300 x 200 km_2 with network of 6 MWR (underlined in figure 3.9) and about 50 surface meteorological stations were set up to collect detailed observations of fog processes.

In the following part of the thesis, I present different methods from the literature to estimate the LWC of warm clouds using ground-based remote sensing instruments. As discussed in this chapter, the cloud radar measurements can be used to derive macro- and microphysical parameters of clouds; therefore, several methods from the literature are presented in the next chapter. In-situ measurements of clouds are used to compare the retrieval parameters from the algorithm and used to develop an empirical relationship.

Chapter 4

Prerequisites and overview of the literature for LWC retrieval

As demonstrated in the previous chapter, remote sensing sensors offer the radiative equivalents of cloud microphysical parameters. These observations necessitate the use of advanced algorithms in order to infer various cloud properties. This chapter, discusses fundamental microphysical parameters relevant to warm clouds applied in my thesis, followed by the classification methods used to identify radar-detected hydrometeors. Furthermore, this chapter presents some available techniques for estimating the liquid water content of clouds based on cloud radar observations, particularly in the context of low-level liquid phase clouds.

4.1 Microphysical parameters of liquid phase clouds

Clouds in the liquid phase typically originate in the lower troposphere, where temperature anywhere within the cloud is not colder than 0°C, and only liquid water droplet exists. Generally, these clouds have a vertical extent of a few hundred meters. Clouds in the liquid phase are mostly composed of small spherical liquid water droplets that are non-uniformly distributed vertically or horizontally. Warm clouds form when condensation occurs on an activated CCN (introduced in section 2.1) and develops to form a liquid droplet. Collisions, coalescence, deformation and evaporation are subsequent processes that occur in clouds. The amount of liquid water per cubic meter is a microphysical parameter measured in warm clouds. The droplet size distribution (DSD) is another important parameter used to characterize cloud microphysics and various processes related to clouds. The number of drops measured as a function of diameter D in a sample represents the drop size distribution $n(D)$. The drop size distribution $n(D)$ is already introduced in 3.8, which is a representative parameter of particles (droplets) in

the given cloud volume to define the radar reflectivity. The DSD, $n(D)$, is defined as the number concentration of particles in a size interval D to $D + dD$ per unit volume, and the total concentration (or the total number of particles per unit volume) N can be written in lognormal distribution as:

$$n(D) = \frac{N}{D\sigma_{\ln D}\sqrt{2\pi}} \exp\left[-\frac{1}{2}\left(\frac{\ln D - \ln D_m}{\sigma_{\ln D}}\right)^2\right] \tag{4.1}$$

where D and D_m are the diameter and median diameter respectively and σ_{lnD} is the logarithmic width of the distribution. The total number of droplets of all sizes in the unit volume of air is represented by N, which is expressed using $n(D)$ such as

$$N = \int_0^\infty n(D)\mathrm{d}D \tag{4.2}$$

In cloud microphysics, the droplet size distribution is generally characterized in terms of its moments, as they can be related to the remote sensing observations under certain assumptions. To express the properties of the droplet size distribution in this sense, the a^{th} moment of the droplet size distribution is used such that:

$$\langle D^a \rangle = \frac{\int_0^\infty D^a n(D)\mathrm{d}D}{\int_0^\infty n(D)\mathrm{d}D} = \frac{1}{N}\int_0^\infty D^a n(D)\mathrm{d}D \tag{4.3}$$

where a is the integral moment of cloud drop size distribution, N is the number concentration as expressed in equation (4.2), which is the zeroth moment of drop size distribution. Similarly, LWC is proportional to the third moment of DSD which is also the integration over the total mass of the DSD expressed as:

$$LWC = \frac{4}{3}\pi\rho_{\mathrm{w}}\int_0^\infty D^3 n(D)\mathrm{d}D = \frac{4}{3}\pi\rho_{\mathrm{w}}N\left\langle D^3\right\rangle \tag{4.4}$$

where ρ_w is the density of liquid water.

The typical values of LWC and N in the continental stratus clouds from different in-situ and satellite measurements are observed 0.28 gm^{-3} and 250 (droplets per cubic centimetre), whereas for fog the number concentration and can go down to 15 and LWC could be as low as 0.06 gm^{-3} ([gre]). Clearly, the vertical structure of the cloud LWC depends on the DSD characteristics, and these are mainly affected by processes such as droplet nucleation activity at cloud base, adiabatic growth of droplets above cloud base, entrainment-mixing processes of air at cloud top, and collision-coalescence.

The values of LWC determined from the equation (4.4) for a vertically inhomogeneous cloud profile, can be extended to a function of range R above cloud base, and thus the integration of the LWC over the cloud height results in the liquid water path (LWP):

$$LWP = \int_{h_{cb}}^{h_{ct}} LWC(R)dR \tag{4.5}$$

where h_{cb} is the height at cloud base and h_{ct} is the height at cloud top.

The proportionality between the moments of DSD forms the basis of the various methods to retrieve the microphysical and optical cloud properties from the surface remote sensing observations, and it is commonly used in the meteorology community (Frisch et al. [1995]Frisch et al. [1998]Sassen and Liao [1996]). It allows us to infer the moments of the DSD from the observed radar reflectivity as defined in equation 3.8, into the microphysical parameters like LWC and effective radius.

4.2 Classification of hydrometeors

In order to interpret microphysical characteristics of clouds using radar observations, a robust hydrometeor classification is necessary. Accurate classification of hydrometeors can provide not only detailed information about the hydrometeor composition of clouds, but also distinguish unwanted targets such as airborne plankton (dust particles and pollens suspended in the air). After classifying the target, a specific retrieval method is employed to retrieve the microphysical parameters. For instance, there are separate retrieval techniques for pure liquid and pure ice clouds, which are often relevant to single-phase cloud systems. A precise target classification scheme can make a considerable contribution to operational nowcasting applications based on radar observations. In the context of cloud radar, signal processing includes classifying surrounding noise and hydrometeor signal. Various approaches have been proposed in the literature to further characterize the hydrometeors that have been identified by radar. Although, it is important to know the several types of hydrometeors. Clouds, fog, rain, snow, hail, dew, and snow are all examples of well-known hydrometeors. AMS glossary of meteorology defines hydrometeor as *'Any product of condensation or deposition of atmospheric water vapour, whether formed in the free atmosphere or at the earth's surface; also, any water particle blown by the wind from the earth's surface'*[AMS]. Note that snow or water on the ground is, by convention, not considered a hydrometeor. There are many ways of classifying hydrometeors, one of which is as follows:

1. Suspended liquid or solid particles, for example, cloud, fog, ice fog, aerosols
2. Liquid precipitation, for example, drizzle and rain
3. Solid (frozen) precipitation, for example, snow, hail, ice pellets or crystals
4. Freezing precipitation, for example, freezing drizzle and freezing rain

Low-level clouds are often observed with rain and drizzle, and because larger droplets like drizzle and rain can cause strong attenuation of the radar signal, hence it is very important to classify the hydrometer and apply the relevant retrieval method to estimate microphysical properties accurately. Particularly in thick liquid clouds, drizzle and liquid cloud droplets frequently coexist. In such cases, the classification is commonly developed using various theoretical or observational values of radar variables, and using them as thresholds to distinguish clouds and drizzle. For instance, Frisch et al. [1995], Vivekanandan et al. [2020] used radar reflectivity thresholds to differentiate clouds and drizzle. Between -15 dBZ and -20 dBZ are the empirically determined thresholds to separate drizzle from pure liquid cloud reflectivity in the cloudy areas. Classification methods based on analysis of Doppler spectrum from a profiling cloud radars is also used to distinguish the phase of the droplet showing certain signatures in the recorded spectra [Acquistapace et al., 2017].

As my thesis is focused on LWC retrieval methods for low level clouds, therefore I used the available hydrometeor classification scheme and proceed to develop LWC estimates. This target classification level 2 (L2 from now onwards) product of vertically pointing BASTA radar currently has phase discrimination of liquid cloud, rain, drizzle and ice. The classification method is based on melting layer detection using the radar reflectivity (Z) and velocity (V_D) gradients of the cloud profile. The height of the melting layer give a proxy of liquid or ice phase distinction. Further, fall velocity of the hydrometeor is used to distinguish between liquid cloud, drizzle and rain. The velocity of droplets falling faster than 1.5 ms^{-1} are considered rain and velocity of droplets less than 0.5 ms^{-1} is considered as liquid cloud droplet. Radars also detect boundary layer insects, large dust particles and pollens suspended in the air, these non-hydrometeors detected by radar are called airborne planktons. I separated these boundary layer airborne planktons manually by looking at the onset close to ground from noon to evening. These airborne planktons can be a reason for uncertainties in LWC retrieval, which is detailed in section 5.2.4.

Nevertheless, there are more sophisticated target classification schemes available in literature. Because a detailed classification of hydrometeors using only one remote sensing instrument can be challenging, since no individual instrument can unambiguously classify cloud phase for all clouds under all meteorological conditions. Hence, a multi-sensor approach is beneficial for the classification of hydrometeor. Many target classification schemes employ a combination of active and passive remote sensing instruments like cloud radar, lidar, microwave radiometer, and radiosonde, (e.g., CLOUDNET [Hogan and Connor, 2004],[Illingworth et al., 2007],[Shupe, 2007]). These approaches can distinguish between liquid, ice, mixed phase, drizzling, raining, and snowing clouds, aerosols and insects. However, the accurate classification of phase in a mixed phase

cloud is very complex. Differences in scattering processes between radar and lidar allows improved target classification and detection of spherical water droplets and other non-hydrometeors (aerosol and airborne planktons) below cloud base. After determining the category of hydrometeors, the next aspect is to evaluate how these hydrometers are interacting with the radiation and impacting the radar measurements.

4.3 Atmospheric Attenuation

Attenuation is the exponential decay of radiation (amplitude, power) during the transmission through the medium. In meteorology, the atmospheric attenuation is caused by gases and the hydrometeors. Water vapour and oxygen are the two primary atmospheric gases that contribute to gaseous attenuation. At millimetre wavelengths, the contribution from oxygen is relatively less, but the contribution from water vapour can be quite large and is very sensitive to the amount of water vapour in the atmosphere. In case of hydrometers, attenuation due to clouds, precipitation, ice and melting layer is described differently. The impact of attenuation is taken into account in radar equation (3.4) where the parameter L indicates attenuation. By definition, attenuation is the loss in the transmitted power dP is a function of distance dR in a two-way attenuating medium. As the wavelength of the radar decreases, the attenuation also increases through each medium. Attenuation by atmospheric gases is relatively small at low temperatures, at high temperatures and frequencies, the attenuation is significantly higher and must be corrected for. Despite the enhanced sensitivity with the shorter wavelength, cloud radars are also associated with attenuation issues. Even though W-band radars work in one of the water vapour transmission windows, absorption due to water vapour can reach 2 $dBkm^{-1}$ depending on temperature and humidity in the lower troposphere [Kollias et al., 2007]. Two-way atmospheric attenuation of about 0.5 dB for humidity less than 45% was observed by Delanoë et al. [2016], however the atmospheric attenuation can vary depending on the latitudes. Attenuation by rain is significant at $95GHz$ and there is an additional attenuation due to wet radome which can reach almost 20 dB as observed by BASTA [Delanoë et al., 2016]. The radome attenuation is significantly reduced by installing a very powerful blower in BASTA. Clearly, the radar reflectivity measured by the cloud radar is biased by attenuation due to mentioned hydrometers and gases and therefore these attenuation biases must be eliminated before it can be used. In cases of ground based vertically pointing radar, when looking at low-level liquid clouds, attenuation due to ice and melting layer is not necessary to be considered. However, there is still a need to account for cloud droplets and atmospheric gas attenuation, though.

At cloud radar wavelengths, cloud particles are sufficiently small and attenuation (extinction) by clouds satisfies the condition of Rayleigh approximation. Moreover, for

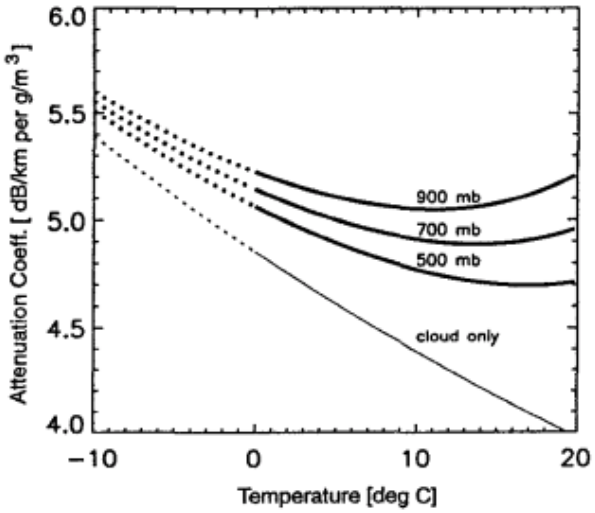

Figure 4.1: Attenuation by clouds and water vapour at $95GHz$. Figure source: Vali and Haimov [2001]

such small particles, the scattering is small compared to absorption (equation 2.2). In fact, the extinction by absorption due to cloud particle is proportional to the volume of liquid particles. This proportionality of attenuation with cloud liquid water content can be presented as

$$A = k_c \times LWC \tag{4.6}$$

where k_c is the coefficient of attenuation by cloud per unit density in $dBkm^{-1}$ and is dependent on wavelength and the temperature. Figure 4.1 shows the extinction coefficient per gm^{-3} of liquid water content (LWC) for clouds alone, and for the total attenuation including cloud and water vapour using the approximation given by Liebe [1985] [Vali and Haimov, 2001].

In addition to this approximation to determine the attenuation at 95 GHz, Lhermitte [1990] also calculated approximately 4 $dBkm^{-1}$ per gm^{-1} attenuation due to liquid water at temperature between 0° to 20°C using Mie calculations. When using measurements from 95 GHz radar to determine LWC, the radar reflectivity must be corrected for attenuation, which can range between 0 and 4 $dBkm^{-1}$. The detailed discussion about incorporating attenuation in the LWC estimation method is presented in the section 5.2.3. After the attenuation correction, the radar reflectivity can be used to infer cloud microphysical properties like LWC, and the techniques to link radar reflectivity Z with LWC are illustrated in the next section.

4.4 Cloud radar based techniques for LWC retrieval

As already stated, the estimation of LWC from remote sensing instruments like cloud radar requires one to invert the observations parameters in order to obtain the cloud liquid water content. Various methods such as empirical methods, statistical methods, probabilistic methods, Doppler spectral analysis etc, are generally employed. The proportionality between the moments of DSD (explained in section 4.1) forms the basis of the method to retrieve the microphysical properties of clouds from the surface remote sensing observations.

Cloud radars at $95GHz$ have the major advantage of the frequency which is ideal for observing cloud as it lies within a part of the spectrum which experiences relatively low absorption in the atmosphere, whilst being high enough to resolve small particles like cloud droplets by Rayleigh scattering [Lhermitte, 1990]. The development of various techniques to estimate cloud liquid water content using W-band cloud radars are briefly discussed in the next few sections.

4.4.1 Empirical relation

As introduced in section 3.1, the in-situ particle size spectra of clouds can be measured by sensitive cloud probes. Universal $Z - LWC$ relations proposed in the literature are derived using these in-situ measurements of droplet spectra from a research aircraft flying through clouds [Atlas, 1954],Sauvageot and Omar [1987], [Fox and Illingworth, 1997]. The in-situ sensors such as forward-scattering spectrometer probe (FSSP), cloud droplet probe (CDP) (described in chapter 3) are used to collect the cloud microphysical parameters (e.g. DSD, LWC). These microphysical parameters, are correlated to obtain a linear relationship in log space. For instance, the DSD collected from in-situ cloud sensor can be used to estimate radar reflectivity factor Z and LWC by calculating sixth and third moment of DSD respectively. Then, the logarithmic Z (in mm^6m^{-3}) and LWC (in gm^{-3}) dataset are fitted to a linear relation using the least squares criterion for the best fit. However, there are further steps including filtering of larger droplets from of spectra, and a detailed analysis of deriving empirical relations is discussed by Baedi et al. [2000] with the validation of derived Z-LWC relations using air-borne radar and lidar measurements.

In order to derive such relationships, various field campaigns focusing different types of clouds over different geographical location for example CLARE'98 (UK), CAMEX-3 (Florida, USA), DYCOMS-II (the Pacific) have been conducted. A brief description of these campaign data set, and their implementation to retrieve LWC from radar reflectivity using different types of the Z-LWC relationships, can be found in Krasnov and Russchenberg [2005]. A typical form of relating radar reflectivity Z with

Table 4.1: Z-LWC relation from literature

Reference	Z-LWC relation	lna	Cloud type
Atlas [1954]	$Z = 0.048 \cdot LWC^{2.0}$	-3.0365	Clouds without Drizzle
Sauvageot and Omar [1987]	$Z = 0.03 \cdot LWC^{1.31}$	-3.5065	Non-precipitating stratocumulus and cumulus
Fox and Illingworth [1997]	$Z = 0.012 \cdot LWC^{1.16}$	-4.4228	Non-precipitating marine stratocumulus
Baedi et al. [2000]	$Z = 0.015 \cdot LWC^{1.17}$	-4.1997	Stratocumulus clouds
Wang and Geerts [2003]	$Z = 0.044 \cdot LWC^{1.34}$	-3.1235	Non-precipitating marine stratus
Krasnov and Russchenberg [2005]	$Z = 323.59 \cdot LWC^{1.58}$	5.7794	Drizzle clouds

cloud liquid water content LWC is a power law equation is

$$Z = a \cdot LWC^{b} \tag{4.7}$$

where a and b are constant coefficient and Z is in mm^6m^{-3} and LWC is in gm^{-3}. If Z is known, LWC can be calculated. The value of coefficients a and b varies from 0.012 for marine stratocumulus cloud (Fox and Illingworth [1997]) to 323.59 for drizzling cloud (Krasnov and Russchenberg [2005]) and the exponent b varies between one and two. Table 4.1 shows details of empirical $Z - LWC$ relations from literature for a given cloud type. The column lna is the natural log of prefactor a, and this is discussed in chapter 5.

The empirical method requires only radar reflectivity information to estimate LWC of the cloud. But, the performance of all $Z - LWC$ relationships listed in table 4.1 depends strongly on cloud microphysics, which varies with changing ambient conditions. Considering natural variability of cloud droplet spectra, it is difficult to find a universal $Z - LWC$ relationship. The empirical approach is also based on certain approximations in DSDs which widely vary within the cloud and among different cloud systems. This can be shown analytically, if we replace $n(D)$ from equation (4.1) to equation (4.4) and (3.8), only one of the three unknowns, i.e. σ_{lnD}, D_m or N can be eliminated using two equations. A unique $Z - LWC$ relation may be obtained if other two parameters are known [Ovtchinnikov and Kogan, 2000]. Theoretically, $Z - LWC$ the relationship is derived by assuming the shape of the DSD. Therefore, the relationship derived for a given DSD will not be valid for other DSD. Note that the empirical Z-LWC relation do not account for attenuation of signal by gaseous molecules, cloud and rain droplets

when propagating through the atmosphere. Generally, the attenuation increases with increasing frequency, which should be considered before interpreting Z.

4.4.2 Spectral Analysis

The advancements in cloud radar signal processing allow one to compute the radar Doppler power spectrum in addition to the observed mean Doppler velocity. Doppler spectrum observed by radar is defined as the function of the backscattering cross-section of the droplets in the detection volume with respect to their fall velocity Giangrande et al. [2001]. The idea behind the Doppler spectrum is that the motion of a meteorological target induces a Doppler frequency shift on the radar signal. Because many particles are moving with their speed and direction, the radar backscattered signal thus contains combined information of all the frequency shifts created by the different particles. Hence, the backscattered radar signal is a function of the full range of frequency shifts, is called the Doppler spectrum. Furthermore, with the assumption that fall velocity is a function of droplet size, the power spectrum is related to the drop size distribution. Typically, the first three moments of the radar Doppler spectrum, i.e., total power, mean Doppler velocity, and velocity variance, are used in radar spectral analysis [Kollias et al., 2011].

The analysis of Doppler spectra helps separate the phase of hydrometeors by identifying their signature shape and the number of local maxima in the Doppler spectrum, as stated in the section 4.2. Higher moments of the Doppler spectrum, e.g., Doppler spectrum skewness, are used to classify particles such as cloud droplets and drizzle droplets [Acquistapace et al., 2017]. However, in the context of this thesis, as the Doppler spectra are not operationally available with the vertically pointing BASTA radar, we decided to concentrate on developing a method to estimate LWC using radar-microwave radiometer synergy. We foresee utilizing Doppler spectra operationally and making the most of the cloud information from BASTA cloud radar.

4.4.3 Multi-sensor retrieval techniques

Given the inherent heterogeneity of cloud droplet spectra, finding a universal $Z - LWC$ relationship in the form of equation (4.7) with constant coefficients is challenging. Radar, lidar, and microwave radiometers are among the most suitable remote sensing instruments used to observe cloud properties. Due to different operating frequency, each of these instruments provides a unique perspective of cloud information. For instance, a lidar sensor can detect the cloud base efficiently, but the lidar signal weakens as it passes into the cloud, making it difficult to reach the cloud top. Conventional microwave radiometers measure the path-integrated microphysical equivalents of the cloud profile

(e.g., brightness temperature). Because of short wavelengths, cloud radars, on the other hand, can detect even the smallest cloud droplets and ice crystals, but they are typically not sensitive enough to identify the small droplets at the cloud base, instead they are most adequate for detecting cloud tops. Combining these devices is therefore an effective approach to obtain the cloud microphysical properties.

Therefore, to improve the accuracy of LWC estimates, additional information such as N and (or) integrated Liquid water path (LWP) has been used with radar reflectivity. However, the complexity of estimating LWC increase many folds due to the presence of drizzle with cloud in the profile. If drizzle drops are present in the radar volume, they contribute substantially to the radar reflectivity factor because of larger droplet size in Rayleigh regime (αD^6)). Since the concentration of drizzle drops is rather low compared to the concentration of the smaller droplets, their contribution to the LWC is small. Therefore, the empirical and theoretical obtained $Z - LWC$ relationships will produce biased results when there is drizzle present in liquid water clouds.

Because radar and lidar are both differently sensitive to droplet size, by radar to the larger droplets, and lidar to the smaller ones. When combined, better insights are obtained in the microstructure of the clouds.

Cloud radar when combined with a microwave radiometer which gives the total liquid water path in the cloud, and the properties like mean droplet size, number concentration can be derived. The combination of instruments with cloud radar is highlighted in the next section, where a few methods from available literature are introduced.

Combination of active sensors

Lidar is the optical counterpart of meteorological radar, which is discussed in chapter 3.2.2. Very smaller particles in the atmosphere can be identified at optical wavelengths. This remote sensing instrument is also used for analysing thin cirrus clouds in synergy with cloud radars. Due to the shorter wavelength, lidar is more sensitive to small particles because most of the cloud particles are larger than the typical lidar wavelengths (355 nm, 532 nm, and 1064 nm) therefore clouds fall with in the optical scattering regime. Whereas radar complements lidar by representing large particles in DSD.

In the Rayleigh regime, as the radar reflectivity factor is proportional to the sixth moment of the DSD (Eq. 3.8), while in case of the lidar instruments, the measured backscatter signal is related to optical extinction, which is proportional to the second moment of the DSD. A common approach to utilize radar-lidar synergy is to define the characteristic droplet diameter that is represented by the ratio of radar reflectivity to the lidar extinction (Z/α) [Krasnov and Russchenberg, 2005] and the ratio of radar reflectivity to the lidar backscatter (Z/β) [Zhang et al., 2021].

Krasnov and Russchenberg [2005] used the ratio of radar reflectivity to lidar ex-

tinction coefficient(Z/α) to classify clouds into 'without drizzle', 'with light drizzle' or 'with heavy drizzle' in the vertical profile. Further, they used the empirical $Z - LWC$ relations from previous studies to estimate LWC in the classified profile. Although, this technique is more realistic than using empirical $Z - LWC$ relation, which may not be appropriate for any form of drizzling clouds. It is worth highlighting that this method can fail to categorize drizzle in the cloud for thick stratus clouds, as lidar signal cannot reach the cloud top. Estimation of microphysical properties of drizzle falling below the cloud base of is also challenging due to the mentioned reason. The radar-lidar synergy have shown satisfactory results to retrieve vertical profiles of mean diameter(D_0), LWC of drizzle, and drizzle liquid water flux below cloud base [O'Connor et al., 2005].

Although, use of lidars for remote sensing of liquid water clouds is limited because of the strong attenuation of the signals in liquid water clouds; however, these are very useful for determining cloud base in case of microphysical analysis of fog (e.g., [Wærsted et al., 2017]), classification of hydrometeors ([Illingworth et al., 2007]), and estimation of ice microphysical parameters ([Delanoë and Hogan, 2008]). Nevertheless, in the context of estimation of LWC in liquid water clouds, we have to opt for a stronger synergy of radar and microwave radiometers, which is discussed in the next section. Although, we do not exclude the use of lidar in the future, as the cloud microphysical properties and the optical extinction are related and therefore, valuable information of cloud microphysics can be found [Sarna et al., 2021].

The multi-sensor approach towards retrieving LWC from radar measurements also includes two radars at different wavelengths. Since attenuation is proportional to LWC within the Rayleigh backscattering regime, the differences between the Z measurements at a certain height give information on attenuation and thus on LWC [Hogan et al., 2005].

Radar-microwave radiometer

Cloud radar in synergy with passive microwave radiometer (MWR) have been proposed in several studies for retrieving liquid water content of clouds. Ovtchinnikov and Kogan [2000] evaluated the accuracy of different liquid water retrieval algorithms based on empirical Z-LWC power law relationships by comparing the Z and LWC obtained from cloud droplet spectra generated by the LES (Large Eddy Simulation) model. With these comparisons, Ovtchinnikov and Kogan [2000] concluded that the performance of the retrieval algorithms can be significantly improved by introducing an additional constraint based on the independently measured liquid water path.

Furthermore, the combination of radar reflectivity factor Z and LWP from MWR has been introduced by Frisch ([Frisch et al., 1995],[Frisch et al., 1998],[Sassen and Liao, 1996]) to retrieve cloud properties. The retrieval methods based on combination of Z and brightness temperature T_b (a measure of radiance emitted by a grey body) from

MWR has shown much better estimates than any empirical relation for liquid water clouds (Löhnert et al. [2001]). These methods also assume a gamma or log-normal distribution of DSD and a modelled relation between the radar reflectivity and the LWC. Then the estimated LWC is matched with the LWP obtained from the MWR using various approaches. In addition to LWC, effective radius (r_e) can also be determined due to the relation of effective radius and the particular radius moments of DSD. However, if this assumption in DSD differs from the actual DSD, that can add considerable inaccuracies in the retrievals [Miles et al., 2000]. Drizzle drops, significantly increase the radar reflectivity factor which contribute as Rayleigh scatterers (αD^6) whereas, have a minor impact on the LWC since their concentration is often very low in comparison to the smaller droplets. This is why, all radar reflectivity based approaches are restricted to liquid clouds without the presence of drizzle in the radar volume, and thus the empirical and theoretical Z-LWC relationships produce biased results when applied to drizzling clouds.

Retrieval methods based on a combination of MWR brightness temperature, cloud radar reflectivity and radiosonde profiles of temperature and humidity with prior information on the moments of DSDs from in-situ data sets of non-drizzling and drizzling clouds proposed by Löhnert et al. [2004] retrieves the LWC using conditional probability are applicable to drizzling clouds as well.

It is more accurate to use a combination of passive and active remote sensing instruments to estimate LWC than to rely solely on radar information. However, it is not necessary that these sensors are always collocated. There can be cases when the additional instrument is not operational. Using only radar information, how the retrieval of LWC can be optimized? In the next chapter, we will go through a methodology for retrieving LWC for liquid water clouds, which uses additional information when it is accessible and adapts to use a climatology when extra information is unavailable.

Chapter 5

LWC estimation using radar-microwave radiometer synergy

5.1 Introduction

The previous chapters addressed the cloud microphysical parameters such as cloud liquid water content and various ways to observe the clouds. Active and passive remote sensing instruments are suitable for long-term cloud observations from space and the ground. These sensors measure the radiative equivalents and therefore, we need to develop methods to estimate cloud micro physical from the radiative equivalents measured by the remote sensors. At 95 GHz (3.2 mm), the Rayleigh regime is still valid as the radar wavelength is nearly two orders of magnitude longer than the observed cloud droplet size, which is invariably less than 50 μm [Miles et al., 2000]. Therefore, radar reflectivity can be considered proportional to the sixth moment of the droplet spectrum and whereas, LWC is proportional to the third moment of the droplet spectrum. However, Mie scattering becomes significant at larger sizes, such as drizzle droplets. As already described in section 4.4.1, the LWC calculated using any Z-LWC relationships listed in table 4.1 depends strongly on cloud microphysics, which varies significantly with changing ambient conditions. Due to the inherent heterogeneity of cloud droplet spectra, it is challenging to establish a universal Z-LWC relationship. Since the shape of droplet spectrum changes significantly within the cloud structure, the retrieval of LWC using only Z information will not be accurate even if the most appropriate empirical relation for the cloud type is used. To reduce the uncertainties due to unknown droplet spectra, a synergy of two or more active and passive sensors providing additional cloud information with sophisticated retrieval techniques has been used in several studies, which are discussed in section 4.4.3. Following the objective of the thesis to develop an LWC retrieval algorithm using BASTA cloud radar measurements, a method based

on the optimal estimation technique is discussed in this chapter. This retrieval method demonstrates radar-microwave radiometer synergy to retrieve LWC of warm clouds and accounts for attenuation due to cloud droplets. The LWC retrieval algorithm works in two different modes, radar-microwave radiometer synergistic mode (when MWR accompanies radar) and the radar stand-alone mode. The main goal of this method is to make the most of the LWC retrieval when additional information is available with radar measurement, and utilize this a priori knowledge to improve the LWC retrievals when this additional information is not available.

The content of this chapter has been submitted to the Atmospheric Measurement and Techniques journal, and is under review at the time of writing this thesis, with the title 'Climatology of estimated LWC and scaling factor for warm clouds using radar–microwave radiometer synergy'. The discussion is available through the following link: `https://amt.copernicus.org/preprints/amt-2022-3/`. The instrumentation for cloud observations used in the publication is already described in chapter 3, and the various techniques and perquisites to estimate LWC using radar measurement are described in chapter 4. Therefore, this chapter starts with the methodology developed to estimate the LWC of liquid water clouds during my thesis. The optimal estimation technique is described in section 5.2.1, incorporate *a priori* information of desired variables, and the forward model detailed in section 5.2.3 converts these variables into observation parameters. In this algorithm formulation, the measure of uncertainty in observations, forward model and, *a priori* acts as weights in the retrieved quantities. Section 5.3 elaborates the sensitivity analysis of the retrieval algorithm using the synthetic profile, and the validation of retrieval with in-situ measurements is discussed in section 5.4. After evaluating the performance of the retrieval algorithm, section 5.5 focuses on the derivation of the climatology of the retrieved parameters. Finally, the BASTA stand-alone retrieval using climatology is discussed in section 5.6.

5.2 Methodology of LWC retrieval

The objective of the algorithm is to retrieve LWC using radar reflectivity measurements and LWP derived from MWR when the latter is available. The integrated liquid water content in the cloud column constrains the vertical profile of LWC which is strongly related to reflectivity profile. There are several methodologies for modelling such algorithms, including analytical methods, machine learning techniques, and others. The technique proposed in this chapter is framed within the context of optimal estimation theory [Rodgers, 2000]. This approach combines *a priori* information and uncertainties in the observations, the way we represent them and is easily expandable to accommodate additional information from multiple instruments. This retrieval method must

be able to combine active and passive remote sensing instruments to derive the most possible accurate climatology of liquid cloud properties and also work when only radar observations are available (i.e. stand-alone version). This must be achieved using a common framework. Such a technique has been widely applied in previous studies [Löhnert et al., 2001, Hogan, 2007, Delanoë and Hogan, 2008]. Synergistic retrieval combining radar and microwave radiometer in order to estimate liquid cloud properties has been already proposed by Löhnert et al. [2001]. In their approach, they directly assimilate brightness temperature (T_b) and humidity profiles from microwave radiometer. The method presented here aims at providing more flexibility when the microwave is not available. Therefore, we do not directly assimilate brightness temperatures but the microwave radiometer product (LWP) and the associated uncertainties are taken into account. In standalone mode, when only radar is available, our method relies on *a priori* knowledge of liquid cloud properties and their link with radar measurements. This *a priori* information will be built using climatology derived when radar and microwave radiometer are simultaneously available.

Figure 5.1, which represents the block diagram of the method illustrates how the input parameters (Z and LWP) are used to retrieve the output variables (LWC and lna, where lna comes from the power law relation Z-LWC presented in equation 4.7), will support the discussion in the next sections.

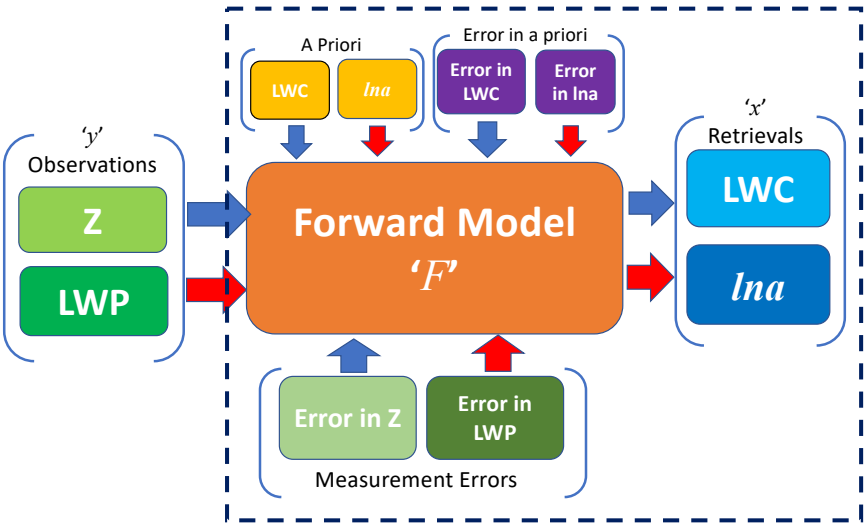

Figure 5.1: Schematic of LWC retrieval algorithm.

5.2.1 Optimal estimation formulation

The optimal estimation [Rodgers, 2000] is a retrieval approach in which the measured quantities are related to unknown atmospheric parameters using a Forward model. If 'y' is the measurement and 'x' is the unknown parameter, then the forward model 'F' and errors 'ϵ' can be mathematically written as

$$y = F(x) + \epsilon \tag{5.1}$$

where error due to measurements and forward model are accounted in ϵ. The forward model is a mathematical description of the atmosphere as a function of the measurements and the atmospheric states. From equation 5.1, to retrieve x (atmospheric states) as $x = F^{-1}(y-\epsilon)$, it is essential to have good knowledge of F before physically inverting it because such operators are generally complex and non-invertible. This problem is referred as the inverse problem. An example of solution of inverse problem is a probabilistic optimization based on Gauss-Newton method [Rodgers, 2000] by minimizing the cost function J as:

$$2J = \delta y^T R^{-1} \delta y + \delta x_a^T B^{-1} \delta x_a \tag{5.2}$$

And the forward model is linearized about the state vector x at i^{th} iteration, then y can be written as

$$y = F(x_i) + K_i(x - x_i) \tag{5.3}$$

where K is called the Jacobian matrix, containing the partial derivative of measurement with respect to state parameter. Minimization of cost function leads to iterative solution for the state at $i + 1$ iteration

$$x_{i+1} = x_i + A^{-1}[K^T R^{-1} \delta y + B^{-1} \delta x_a] \tag{5.4}$$

where $A^{-1} = K^T R^{-1} K + B^{-1}$ gives the error covariance matrix of optimized solution of x after convergence is achieved. R is the error covariance matrix accounting for observation and forward model errors, B is the error covariance matrix for '*a priori*' information and x_a denotes the *a priori* of the state vector. A prior or background information of the unknowns (generally derived from the climatology or model), is used to constrain the inverse problem. The retrieval starts with the 'first guess'(can be *a priori*) of the states, and the forward model is then applied to simulate the values of measurements. The states are updated until the simulated and measured quantities are close enough and convergence is achieved.

Convergence is assessed at each iteration using the following variable to estimate

the closeness of the observations with the model:

$$G = |J(i) - J(i-1)|$$

where 'i' is the iteration number.

For every iteration, G examines the absolute gradient of cost function and achieves the convergence when the difference between two successive cost functions is negligible. In this scenario, the retrieval converges when G is of the order of, 10^{-7} which indicates that the additional iteration is not adding prominent change in the retrievals.

5.2.2 Definition of the state and observation vectors

The state vector 'X' is the vector of unknowns, must contain all the variables to retrieve. The observation vector 'Y' is driven by the available observations. In our case, the radar reflectivity for 'n' vertical levels and LWP (when microwave radiometer is available) are the parameters in the observation vector. These two vectors are also defined in the way that we can link them through the forward model. The forward model accounting for radar attenuation will be described in details in section 5.2.3.

From the power law relation of Z-LWC in equation (4.7) the constants a and b are dependent on many microphysical parameters such as the particle size, number concentration and other ambient conditions. Through this kind of relationships we can associate a LWC value to a reflectivity value, adding LWP retrieved by the microwave radiometer we can release one more constrain and adjust one of the parameters of the Z-LWC relationship that varies with each profile. This is because the retrieved LWC is constrained by the observed LWP. The choice of using the pre-factor a is motivated by its capability to adjust the whole profile of LWC regardless of the reflectivity and a shows a much higher variability than b. Note that the impact of variability in b will be assessed in section 5.3.1.

The state and observational vectors are defined as follows:

$$X = \begin{pmatrix} lnLWC_1 \\ \vdots \\ lnLWC_n \\ lna \end{pmatrix}, \tag{5.5}$$

$$Y = \begin{pmatrix} lnZ_1 \\ \vdots \\ lnZ_n \\ lnLWP \end{pmatrix} \tag{5.6}$$

To account for the large dynamic range of the observations within a profile, this algorithm uses the logarithm of the state variables and measured quantities, which also prevent the unrealistic retrieval of negative values.Therefore, the linear relation between Z and LWC in log space in the form of, $y = mx + c$ where lna represents intercept and b is the gradient of the line can be written as:

$$\ln Z = \ln a + b \times \ln LWC \tag{5.7}$$

The logarithm of *a priori* coefficient a is referred to as scaling factor, and logarithm also enables visualizing the wide range of a. Although, the observation vector y may not incorporate LWP when it is unavailable, however by adding the LWP in the observation with Z, the forward model allows retrieving lna in addition to LWC.

The state and observation vectors are defined as shown in equation (5.5) and (5.6). The errors in measurement are tested using a synthetic profile of observations, and detailed in the section 5.3.1.The most suitable error in observation vector is set as 25% and 10% respectively for Z and LWP. As mentioned in section 3.3.2, LWP estimates from MWRs have an expected uncertainty of $\pm 20\ gm^{-2}$. However, this uncertainty estimation also depends on the MWR calibration and retrieval algorithm uncertainties, an approximate evaluation of the LWP measurements using longwave radiation measurements demonstrates an RMSE in LWP of around 5–10 gm^{-2} during fog with LWP$<$ 40 gm^{-2} [Wærsted et al., 2017]. Thus, to minimize the errors due to the measurement uncertainties, the LWP is assimilated only when the measured LWP is greater than 10 gm^{-2} because the relative error for low LWP values from HATPRO is significantly higher than for high LWP values. Although, 10% error in LWP is very small when compared to expected error, but the profiles with LWP values below 10 gm^{-2} are already excluded from retrievals, implying that there is less error to be considered. A detailed analysis of errors in measurement of Z and LWP are explained in section 5.3.1, covering the sensitivity analysis of retrieval algorithm using synthetic profile.

Prior knowledge of the state parameters enables the retrieval to be constrained in order to avoid unrealistic solutions, especially when additional measurements are missing. *a priori* information usually consists of long-term climatology or model outputs of state parameters, i.e. LWC and lna. For example, from various in-situ measurements of LWC in fog or liquid cloud it is known that LWC in the cloud is not equally distributed vertically and is strongly related to reflectivity. *A priori* of LWC dependent on reflectivity should be more suitable than a constant LWC profile. In this retrieval, a LWC profile derived from the empirical relation is used as the *a priori* with an *a priori* error of 1000% (or 10) for both LWC and lna. Note that the errors are presented in logarithm and the error in the *a priori* is considered high, because LWP measurements are available to constrain the

retrievals. Even so, *a priori* information is vital in case of missing LWP measurements, which plays an important role in case of LWC retrieval using only radar observations and climatology. In such a case, expected error in the *a priori* will be considered less. In case of low LWP observations, retrieval depends on *a priori* which is taken from Atlas [1954] empirical relation and therefore, the scaling factor is not retrieved for such profiles. The retrieval of LWC for the profiles with LWP $< 10gm^{-2}$ incorporates attenuation in the retrievals, rather than just applying empirical relationships.

5.2.3 Description of the forward model and Jacobian matrix

The forward model is an approximation of the physical phenomenon represented as a function of measurement and state variables. In order to expand the retrieval when additional measurement is available, it is recommended to describe the forward model for each element of the observation vector. The forward model for radar links radar reflectivity to LWC using the equation (5.7). Furthermore, LWP as additional information constrains LWC using equation (4.5) and allows the retrieval of scaling factor lna. When additional information is unavailable, the retrieval constrains LWC using lna climatology, which is elaborated in section 5.6. The microphysical model for attenuation consideration is discussed in next subsection 5.2.3.

Forward model for attenuation correction

As described in section 4.3, water vapour and oxygen are the two primary atmospheric gases that contribute to microwave absorption. Even though W-band radars work in one of the water vapour transmission windows, absorption due to water vapour can exceed 1 $dBkm^{-1}$ depending on temperature and humidity in the lower troposphere. Despite the fact that attenuation by atmospheric gases is relatively small, attenuation due to liquid clouds droplets can diminish the advantages of W-band radar observation, particularly in the liquid cloud case. According to Lhermitte [1990], the attenuation due to liquid droplets is more problematic as it depends on drop size distribution, which is not known in general. Since attenuation due to liquid cloud is dependent on temperature and density of cloud droplets and clouds consists of randomly distributed, spherical droplets of diameter less than 100 microns, the 95-GHz microwave absorption can be adequately described by the Rayleigh approximation. Various theoretical studies have been conducted to determine the attenuation due to liquid cloud and drizzle at different temperatures. For example, at 10°C, Lhermitte [1990] calculated 4.2 $dBkm^{-1}$ per gm^{-3} of liquid water attenuation, while Liebe et al. [1989] obtained 4.4 $dBkm^{-1}$ by using the Rayleigh approximation. On the other hand, Vali and Haimov [2001] assumed spherical hydrometeor and obtained the general solution for absorption (and

scattering) at W-band using Mie approximation. Extinction due to liquid cloud at 95GHz using simultaneous and co-located cloud measurements of drop-size distribution, LWC, temperature, and pressure for maritime stratus clouds was comparable with the theoretical studies mentioned above. This study further concludes that, for around 10°C and pressures close to 900 mb, the one-way attenuation 'A' in $dBkm^{-1}$ was found to be linearly dependent on LWC, and expressed as:

$$A = 0.62 + 4.6 \times LWC \text{ in } dBkm^{-1}, \tag{5.8}$$

where 0.62 $dBkm^{-1}$ represents gaseous absorption.

Vivekanandan et al. [2020] calculated attenuation 'A' as a function of reflectivity Z for cloud droplets and drizzle using power law fit. Reflectivity and attenuation are simulated using DSDs collected from VOCALS field experiment [Wood et al., 2011], with Z being proportional to sixth moments and attenuation being proportional to third moments of DSDs. The DSDs for cloud and drizzle droplets are separated by -17 dBZ threshold for simulated reflectivity and, therefore, as given by equation 5.9 and 5.10 for clouds and drizzle respectively.

$$A = 18.6 \times Z^{0.58} dBkm^{-1} \tag{5.9}$$

$$A = 1.68 \times Z^{0.9} dBkm^{-1} \tag{5.10}$$

However, even with power law fit, the range of attenuation calculated is 0 to 4 $dBkm^{-1}$, which is almost the same order of attenuation per kilometre calculated using linear relations proposed in previous studies. Equation (5.8) is used to calculate attenuation due to liquid water in the forward model. As this study is focusing over the retrieval of LWC and its climatology, attenuation as a function of LWC, will adjust with retrieved LWC for cloud and drizzle without categorizing the hydrometeor on the basis of forward modelled reflectivity. It is worth noting that all the attenuation relation mentioned above were derived using DSDs collected from marine clouds, and the calculation of attenuation relation for continental clouds is prospective. Finally, a sensitivity test for considering inconsistent attenuation in the forward model will be discussed in section 5.3.3.

The attenuation correction is achieved within the forward model by correcting at a particular gate to estimate the associated attenuation, and then using it to correct at all subsequent gates. Therefore, the forward model estimates the two-way attenuation corresponding to LWC using equation 5.8, and then corrects the forward modelled

reflectivity to account for the estimated attenuation. Since the radar is vertically pointing, it is presumed that the lowest gate (closest to the radar) remains unattenuated due to the liquid droplets, whereas all gates above are affected by liquid droplets present in the preceding gates. As the radar beam passes through the cloud profile it gets attenuated due to liquid, as a result the top most cloud pixels of the profile are the most attenuated. To summarize, each cloud pixel is corrected for the two-way attenuation caused by liquid clouds along the path of the radar beam.

The Jacobian formulation

The Jacobian is a matrix representing the sensitivity of the forward model. It consists of partial derivatives of all the element of Y vector with respect to X vector. Since the forward model update the element of measurement vector at each iteration, thus, at each iteration step the Jacobian K is re-evaluated and for a profile of 'n' cloud pixels as

$$K = \begin{pmatrix} \frac{\partial lnZ_1}{\partial lnLWC_1} & \cdots & \frac{\partial lnZ_1}{\partial lnLWC_n} & \frac{\partial lnZ_1}{\partial lna} \\ \vdots & \ddots & \vdots & \vdots \\ \frac{\partial lnZ_n}{\partial lnLWC_1} & \cdots & \frac{\partial lnZ_n}{\partial lnLWC_n} & \frac{\partial lnZ_n}{\partial lna} \\ \frac{\partial lnLWP}{\partial lnLWC_1} & \cdots & \frac{\partial lnLWP}{\partial lnLWC_n} & \frac{\partial lnLWP}{\partial lna} \end{pmatrix} \tag{5.11}$$

K consist of $(n+1)\times(n+1)$ elements with top $n\times n$ elements are partial derivative of reflectivity with LWC and last row corresponds to constrain LWC at each cloud pixel with total LWP. The $(n+1)^{th}$ column corresponds to the relation between radar reflectivity and scaling factor (lna) and the very last element is set to zero because lna is not related to LWP measurements. Therefore, for n cloud pixels in a profile, the forward model will evaluate a Jacobian of $(n+1)\times(n+1)$ to retrieve the state vector corresponding to radar reflectivity and LWP measurements. The attenuation in forward modelled reflectivity due to liquid cloud droplets is accounted at every iteration. The Jacobian matrix incorporates the two-way attenuation 'A' at each cloud pixel by calculating the partial derivatives of 'A' with respect to LWC at each cloud pixel. It is worth noting that the attenuation due to gaseous absorption is not accounted in the Jacobian matrix because L2 reflectivity is already corrected for it. The value of attenuation corresponding to the lna parameter is assumed zero.

The forward model errors are the errors associated to the mathematical model which relates the measurements with the atmospheric physical parameters. The relationships described in the forward model are not necessarily perfect and hence incorporate error in the retrieval. As mentioned already, Z is closely related to LWC of cloud and hence forward model for reflectivity is represented by equation 5.7. In this equation, the errors in Z are taken into error in measurement for Z, whereas lna and LWC are retrieved

parameters. As exponent b is taken constant, there is a possibility to incorporate error in forward model due to b, which is discussed in sensitivity analysis in section 5.3.6. The error incorporated because of model representation of attenuation due to liquid cloud is also discussed in the sensitivity analysis. The cloud liquid water is also constrained by LWP as the summation of LWC for the given cloud column, as shown in equation 4.5. Therefore, the forward model for LWP is simple and therefore, error in the estimation of LWC due to forward model is neglected.

5.2.4 Discussion of the retrieval uncertainty

Other sources of error in the retrieval algorithm are discussed in this section. ~~Doppler r~~Radars also detect boundary layer insects, large dust particles and pollens suspended in the air as a result of the convective boundary layer that grows in the morning hours and matures shortly after the midday [Geerts and Miao, 2005]. These so-called airborne planktons developed due to onset of convective boundary layer, contaminate the reflectivity profile. Therefore, the unwanted signal in the radar reflectivity due to airborne planktons must be removed before estimating LWC. Additionally, all the cloud above 2500 m are anticipated to be mixed phase or ice cloud which cannot be addressed in the same way as liquid cloud and therefore clouds above 2500 m are excluded. The data set employed in this study indicates that the majority of the liquid cloud are observed below 2500 m. However, because the height of the melting layer changes with season and geographical location, it would be appropriate to determine the height of the melting layer to differentiate liquid and mixed phase clouds. The LWP measurements from MWR are unaffected by overlying ice cloud, but accounts for liquid in the overlying mixed phase cloud, which adds error in the LWC retrieval. Therefore, all such cloud profiles are removed before deriving climatology. The profiles with LWP less than or equal to 10 gm^{-2}, the retrieved LWC is not used for climatology due to high relative error in low LWP values.

Fog on the other hand, causes droplet deposition on the radome and hence contributes towards substantial amount of attenuation in the radar reflectivity which is not accounted in the retrieval. It is worth noting that a blower to remove the droplet deposition on BASTA at SIRTA is installed since 2019 which has substantially reduced the wet radome attenuation after rain. Although, the retrieval assumes completely dry radome for all the cases, including clouds immediately after rain and drizzle. Since the retrieval algorithm deals with two independent measurements and therefore the two instruments have distinct observation frequency which is addressed by interpolating the LWP measurements into the radar temporal resolution and hence acts as additional source of error.

Due to the coupling of transmitting and receiving antennas of radar, the vertically

pointing radar misses a few lowest gates close to the ground. These unavailable gates do not impact the information about the clouds aloft, but the missing information of thin fog causes over estimation in LWC for the first few available gates. The overestimation is due to the fact that retrieval forces the assimilated LWP of the profile by constraining it over available range gates and hence overestimates the LWC for available gates. The most appropriate way to overcome this issue is to use scanning radar, but for vertically pointing radar we assume that the properties of fog remain the same between the first available gates and the ground, and thus reflectivity is extrapolated (extended) downwards for the unavailable range gates. The extension of range gates is particularly significant for SOFOG-3D experiment cases, which are specifically concerned with fog processes. However, the extension of range gates may introduce inaccuracy into LWC retrieval for fog, as the reflectivity of fog at the surface is not always equal to the reflectivity of the first available gates, particularly for dissipating fog.

5.2.5 Analysis of the method when microwave radiometer is available

This section describes the analysis of retrieval when applied to various cloud types. As detailed in section 5.2, the retrieval technique is applied to reflectivity data from 95 GHz BASTA radar with LWP estimates from co-located RPG HATPRO microwave radiometer for various cloud cases from SIRTA. Between November 2018 to May 2019, 39 cloud and fog cases at SIRTA observatory are selected to address the algorithm's implementation on warm clouds. The data set contains a relatively large number of cloudy cases, including fog and light drizzle. A detailed discussion of retrieval and algorithm implementation is elaborated for a typical example of cloud in the next subsection.

Illustration of retrieval of 05 February 2019 case at SIRTA

A case study of one of the selected cloudy cases from SIRTA on 05 February 2019 is presented in figure 5.2. Figure 5.2(a) and (b) presents the time height plot of radar reflectivity and velocity, respectively. LWP estimated by the radiometer alone through quadratic regression is interpolated at radar time of observation as shown in figure 5.2(d). The retrieved LWC for the cloud pixels is plotted in figure 5.2(c) and the retrieved scaling factor for each profile is shown in figure 5.2(e).

There were no overlapping clouds observed in this instance, and the airborne planktons were removed manually. A dense cloud from midnight with cloud base close to ground dissipates before noon and the formation stage of a fog is initiated after the sunset. The liquid water path remains below 100 gm^{-2} throughout the day. The radar

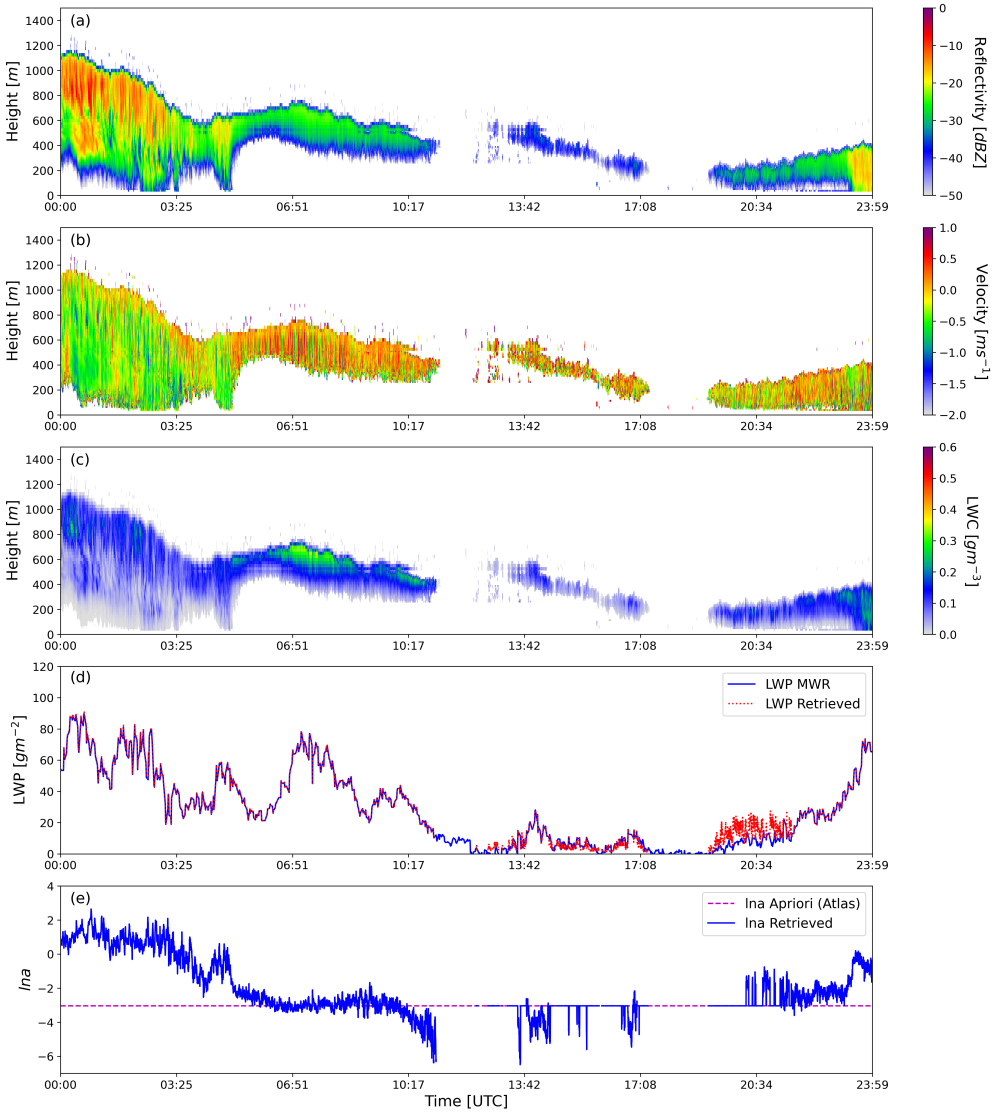

Figure 5.2: (a) Radar reflectivity (b) Vertical velocity (c) Retrieved LWC, (d) LWP and (e) Retrieved *lna* for 05 February 2019 case at SIRTA.

Doppler velocity, displayed in figure 5.2(b), shows variation in the velocity of the cloud droplets, ranging from -1.5 to 1 ms^{-1}. Within the cloud, the velocities are typically low and decrease toward the cloud top, when they approach 0 ms^{-1}. Cloud droplets have terminal velocities of only a few centimeters per second, when drizzle droplets develop, the terminal fall velocity increases. Reflectivity values reach 0 dBZ for a few profiles indicating drizzle in the beginning (between 00:00 to 03:00 hrs). As indicated by radar observations, higher reflectivity values due to drizzle, yet LWP is nearly identical for the cloud with reflectivity as low as -35 dBZ and contributes the least to LWP. This also explains why it is critical to have LWP information to constrain LWC retrievals, particularly for profiles with drizzle within the cloud and when it evaporates fully before reaching the ground. Figure 5.2(c) indicates a general increase in LWC towards the cloud top, and the retrieved LWC is less than 0.3 gm^{-3}. The scaling parameter has a wide range from -6 to +3 which supports empirical values of a in table 4.1. The value of lna changes for each profile. Therefore, this case illustration shows that the retrieval of LWC and scaling factor can be utilized to derive a climatology of scaling factor for different cloud types. It is worth noticing that the retrieval algorithm deals with all the variations of cloud types, and the behavior of scaling factor must be studied. The next section elaborates the robustness of the retrieval algorithm for various sensitivity parameters.

5.3 Sensitivity analysis of retrieval algorithm using synthetic data

The goal of this section to verify the consistency of the retrieval behavior and to assess the sensitivity of the algorithm to inputs, errors and hypotheses. Sensitivity analysis does not replace a proper validation of algorithm retrievals, in section 5.4 a comparison with in-situ measurement is discussed. Like every other algorithm, this retrieval algorithm also suffers from some fundamental uncertainties which must be addressed. To do so, we use a sensitivity analysis approach. It can also be referred to as 'what-if' analysis, where the input parameters of the model are varied one by one. As shown in the schematic of the retrieval algorithm in figure 5.1, the retrieval is sensitive to not only input parameters but also other settings like the *a priori*, expected errors in measurement and *a priori* information. To quantify the sensitivity of the retrieval algorithm, real observations are not used because the true profile of LWC from an in-situ sensor is not always available. Instead, synthetic data which contains all the characteristics of real observations are used to evaluate the performance of the algorithm. Maahn et al. [2020] highlighted major benefits of using synthetic data to test algorithms and models. First

and foremost, systematic forward model errors cancel each other, and second, we know the true atmospheric state X_{truth}, which can be compared with the retrieved optimal result X_{ret}. Hence, considering the mentioned advantages, we are using synthetic data for the sensitivity analysis of the retrieval algorithm.

The flowchart of sensitivity analysis is presented in figure 5.3 where sensitivity parameters are the parameters in the retrieval algorithm which are perturbed, and the impact is tested. The objective is to formulate input parameters from truth and by feeding synthetic observation to the retrieval algorithm, the result should match with the truth. In the block diagram, synthetic observations (Z and LWP) are fabricated using the forward model. The block inside the dashed line is the same as shown inside the dashed line in figure 5.1 with all the sensitivity parameters.

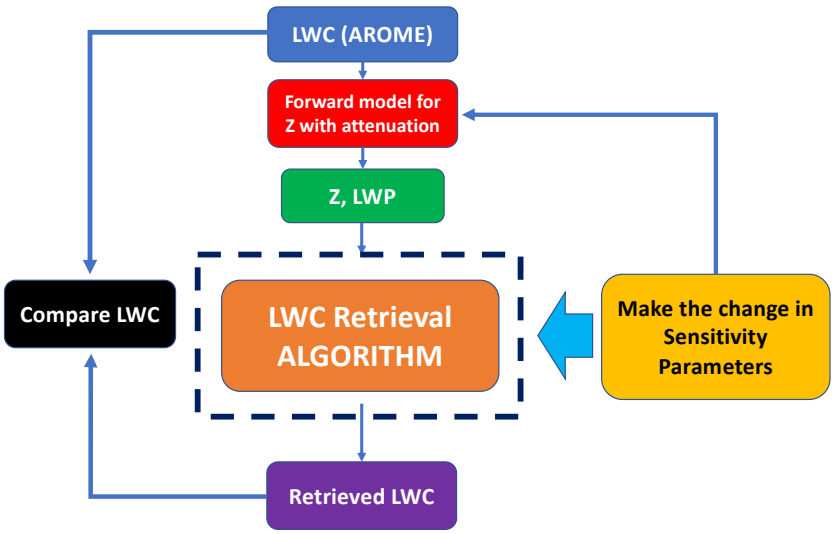

Figure 5.3: Flow chart for sensitivity analysis of retrieval algorithm.

However, we are aware of the fact that the retrieval errors might be different when observed in real observation scenario, which are already discussed in the section 5.2.3 for real observations. The error in retrieved LWC with respect to what we consider as true LWC is calculated using the equation (5.12), (5.13), and (5.14) for all the sensitivity test.

1. Root mean squared error

$$RMSE = \sqrt{\frac{\Sigma_0^n (LWC_{ret} - LWC_{true})^2}{n}} \tag{5.12}$$

2. R^2 (coefficient of determination) quantifies the degree of any linear correlation between observations (LWC_{true}) and retrievals (LWC_{ret}). The general definition of R^2 regression score function is:

$$R^2 = 1 - \frac{SS_{res}}{SS_{tot}} \tag{5.13}$$

where SS_{res} is residual sum of squares and SS_{tot} is total sum of squares.

3. Mean absolute percentage error: It measures the accuracy of the retrieval in percentage.

$$MAPE = \frac{100}{n}\Sigma_0^n \left| \frac{LWC_{true} - LWC_{ret}}{LWC_{true}} \right| \tag{5.14}$$

where LWC_{ret} and LWC_{true} are retrieved and true LWC respectively, and n is the number of data points. Analysis of each sensitivity parameter is presented in the next section.

5.3.1 Description of synthetic data

Synthetic data of LWC can be prepared from empirical relations, satellite observations, theoretical adiabatic LWC or model forecasts. For this sensitivity analysis, we opted to include physical parameters of 16 November 2018 fog structure simulated by the AROME model. The selection requirement for this instance is that it contains a number of LWC profiles with LWP ranging from 20 to 240 gm^{-2} to evaluate the behaviour of the algorithm.

AROME is a French convective scale NWP model, operational since 2008 covering France and western Europe providing high-resolution simulations of fog forecasts at 1.3 km of horizontal resolution and 90 vertical levels of 144 profiles. Detailed setup of the AROME model and fog forecast is explained in Bell et al. [2021]. LWC of a fog structure from AROME short-term forecasts at the nearest grid location of SIRTA is considered as the true atmospheric state. In this case, we are considering only liquid droplets, with no overlapping of liquid or ice clouds aloft. Profiles of LWC simulated by AROME are used to synthesize observation parameters like radar reflectivity using the previously defined power law relation and the liquid water path of each profile by integrating true LWC at each pixel. The forward model (block in red) consisting of the power law relation and attenuation correction model for deriving the synthetic profile of Z using coefficients a and exponent b is taken from Atlas [1954] the empirical relation. The two-way attenuation correction applied to Z is calculated from equation (5.8). Figure 5.4(a) shows the distribution of true LWC as a function of time and height, and the synthetic profile of Z is plotted in figure 5.4(b) and in figure 5.4(c) LWP calculated by integrating true LWC.

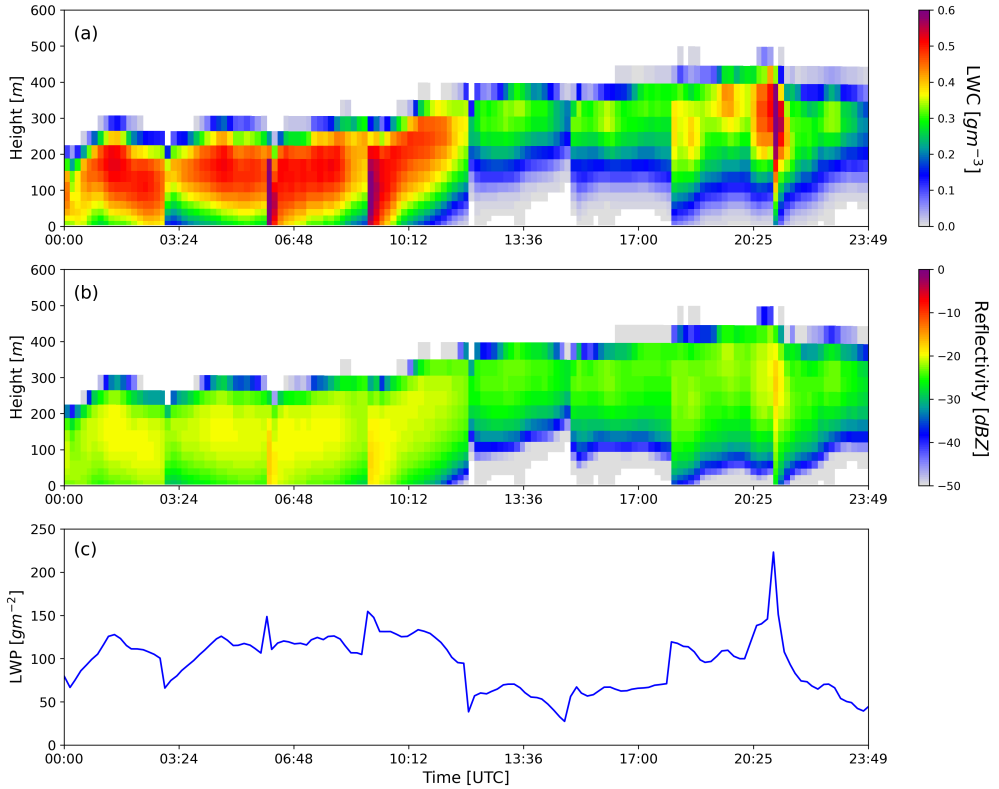

Figure 5.4: Simulations from AROME model for 16 November 2018 showing (a)True LWC in gm^{-3}, (b) Synthetic reflectivity and (c) LWP.

One of the most obvious sources of uncertainty in the retrieval is the observation (calibration errors and instrumental noise) and forward model errors. The forward model errors tested in this sensitivity analysis are the variation in attenuation consideration and the variation in exponent b. As the observation vector, Y contains measurements from two independent instruments, bringing random and uncorrelated errors within the elements of Y [Maahn et al., 2020]. The deposition of liquid droplets on the radome introduce an additional bias in radar observations. This is tested by analyzing the impact of possible biases in Z. The next sections cover the sensitivity analysis of the retrieval algorithm for perturbations in different parameters.

5.3.2 Sensitivity analysis of impact of error in observation

The input for synergistic retrieval in the observation vector Y consists of concatenated observations from the cloud radar and the radiometer. Each instrument has different errors, and it is worth mentioning that in case of radar observations, instrumental errors are considered for each gate whereas for the LWP measurement from the radiometer the observation error is estimated over the entire cloud profile i.e. an integrated measurement. By varying the weight of instrumental error from each observation (Z and LWP)

and keeping the rest constant, impact on the retrieved LWC is compared with the true LWC.

Observation errors are assumed to be independent, and the synthetic observations of Z and LWP are calculated using true LWC, as shown in figure 5.4. Equation (5.8) is used to calculate attenuation due to liquid water in the synthetic profile as well as in the forward model. *A priori* for LWC is calculated using synthetic reflectivity and scaling factor from empirical relation proposed by Fox and Illingworth [1997]. Since we are looking at the impact of observation error, the retrieved parameters should have the least contribution from *a priori* and therefore high error in *a priori* (1000% in this case) is considered. Because *a priori* of LWC is calculated from synthetic Z, *a priori* of LWC must be different from true LWC to minimize the contribution of *a priori* which forces retrieval to be close to true LWC.

Table 5.1 shows the combinations of errors in measurements of Z and LWP considered in the retrieval, and the errors are calculated for retrieved LWC with reference to true LWC. Cases 3 and 4 in table 5.1 are indicating that the retrieval is more sensitive to errors in LWP as compared to errors in Z with approximately the same mean absolute percentage error in LWC of 7% whatever the assumed errors in Z. This is because for each profile there is only one LWP value which impacts the whole profile for given error but for error in reflectivity, only the associated pixel is impacted. With the increase in percentage errors in LWP measurement from 1 to 100%, the RMSE in LWC is also increased approximately 100 times, further demonstrating the high sensitivity of the algorithm to the LWP.

Delanoë and Hogan [2008] likewise incorporates a 1 dBZ uncertainty in the measurement of Z for ice cloud retrieval using 95 GHz radar with lidar and microwave radiometer. However, error in LWP has very low difference in MAPE and RMSE when 1% to 10% error is considered. Therefore case 6 in table 5.1, is an optimum balance of observational error for Z and LWP. This combination of error in measurement is used in all the retrieval cases presented in section 5.2.5 and 5.4.1.

Table 5.1: Different configurations of error in measurement and respective statistical errors in retrieved LWC w.r.t. true LWC

Case	Error in Z	Error in LWP	RMSE (LWC)	$R^2(LWC)$	MAPE(%) (LWC)
1.	1% (0.043 dB)	1% (1.01 gm^{-2})	0.000209	0.99999	0.05783
2.	100% (4.34 dB)	1% (1.01 gm^{-2})	0.000245	0.99999	0.15286
3.	1% (0.043 dB)	100% (2.71 gm^{-2})	0.021870	0.98495	7.37329
4.	100% (4.34 dB)	100% (2.71 gm^{-2})	0.021832	0.98499	7.43851
5.	25% (1.08dB)	50% (1.64 gm^{-2})	0.006013	0.99874	2.05276
6.	25% (1.08dB)	10% (1.1 gm^{-2})	0.000454	0.99999	0.17123

5.3.3 Sensitivity analysis of impact of attenuation due to liquid droplets model

In this section, the sensitivity of the attenuation model considered in the algorithm to retrieve LWC is highlighted. Wet radome can cause up to 20 *dBZ* of two-way attenuation due to rain in the reflectivity [Delanoë et al., 2016], but attenuation due to fog is far less than 20 *dBZ*. Two attenuation relations for liquid clouds from literature are used to test the sensitivity of the algorithm. Equation (5.8) is proposed by Vali and Haimov [2001] in which attenuation is a function of LWC (abbreviated as att(LWC) in table 5.2) and the relationship in equation (5.9) is proposed by Vivekanandan et al. [2020] where attenuation is the function of radar reflectivity factor (abbreviated as att(Z) in table 5.2). Both of these relationships are derived using in-situ observation from 95 GHz radar mounted on a research aircraft. Forward model with different attenuation relationships in the algorithm is tested for synthetic Z and LWC. To fabricate synthetic Z, the power law relation with $a = 0.012$ and $b = 2$ (in equation (4.7)) is used. Different combinations of attenuation correction in synthetic profile and in the retrieval algorithm are tested, as shown in table 5.2. *a priori* for state parameters is calculated from Atlas [1954] empirical relation with error in *a priori* as 1000% and the measurement errors for Z and LWP are considered 25% and 10% as discussed in section 5.3.2. Finally, the comparison of bias in LWC for attenuation model is shown in figure 5.5.

Table 5.2: Variation in error in *a priori* and different errors calculated w.r.t. true LWC

Attenuation correction in synthetic profile	Forward model attenuation	RMSE (LWC)	R^2(LWC)	MAPE(LWC)%
Z (attLWC)	Att (LWC)	0.000204	0.999998	0.056426
Z (attLWC)	Att (Z)	0.008286	0.997535	2.780574
Z (attZ)	Att (LWC)	0.008012	0.997687	2.660039
Z (attZ)	Att (Z)	0.000206	0.999998	0.057094

Retrieved LWC considering same attenuation correction in synthetic Z profile and in forward model, RMSE is 0.0002 and MAPE is as low as 0.05% as all the parameters are identical. But when the attenuation relation is exchanged for synthetic profile and the forward model, MAPE increase to 2.7%. Figure 5.5 shows the bias in LWC when different attenuation relation is used in the forward model and synthetic profile. The distribution of bias in LWC over the profile is different because attenuation due to LWC estimated by two relation is different, and thus the estimated LWC is also different. A similar test for attenuation with different 'a' in the power law relation gives the same errors when the retrieved LWC is compared with true LWC. Bias in LWC for considering same attenuation relation in synthetic profile and forward model is found close to zero. Therefore, the sensitivity test for attenuation indicates that attenuation correction of Z

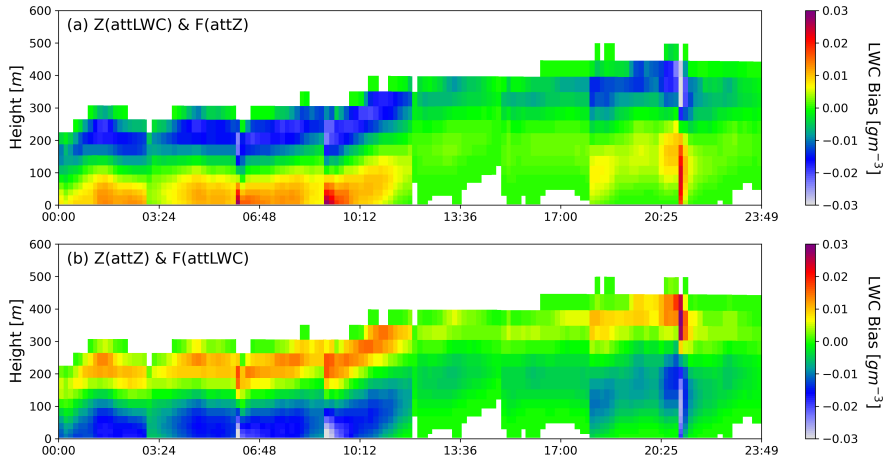

Figure 5.5: Bias in retrieved LWC with respect to true LWC for different attenuation consideration in the retrieval algorithm

has very low-impact, and it can bring up to 2.7% mean absolute percentage error in retrieved LWC when wrong attenuation model is used.

5.3.4 Sensitivity analysis of bias in Z and LWP

Bias in observation is the systematic error added in measurement, which can be due to the error in calibration of any instrument or transfer function of the measurement. Similarly, threshold value of MWR also adds a systematic error in LWP measurement. Therefore, it is necessary to test the behavior of retrieval algorithm for such systematic biases in measurement. For the test cases of biases, error in observation vector in considered 25% and 10% for Z and LWP with *a priori* of LWC is calculated using $a = 0.012$ proposed in Fox and Illingworth [1997] and $a = 0.012$ is used as *lna a priori*. This test is to analyze the impact of bias in measurement on retrieval, therefore the *a priori* should have minimum contribution and hence 1000% error in *a priori* of LWC and *lna* is considered. In this analysis, only one of the two observations is biased at a time to see the individual impact on retrieval. It is assumed that the bias in Z is 2 *dBZ* considering that error in calibration in BASTA radar measurements is around 1 to 2 *dBZ* [Toledo et al., 2020]. The bias in LWP estimation is considered 10 gm^{-2} which is supported by Wærsted et al. [2017] for this sensitivity test.

Table 5.3: Error in retrieved LWC due to bias in Z and LWP

Case	Bias	RMSE(LWC)	R^2(LWC)	MAPE(LWC)%
1.	LWP-10 (gm^{-2})	0.029413	0.96343	11.246633
2.	LWP+10 (gm^{-2})	0.030236	0.97184	11.542570
3.	Z-2 (dBZ)	0.000355	0.99999	0.131603
4.	Z+2 (dBZ)	0.000558	0.99998	0.210887

The order of error in retrieved LWC with respect to true LWC is much higher for 10 gm^{-2} bias in LWP than 2 dBZ bias in Z. However, the bias in two measurements is not comparable because parameter Z is measured over each pixel and LWP is a single point measurement for the whole column. Since the bias applied on Z applies on each cloud pixel and bias applied in LWP is integrated for whole profile, however, 11% MAPE in LWC is observed which is again indicating the sensitivity of retrieval for LWP. Another reason for the difference in LWC is due to the fact that Z is in log space and error in observation allows more spread in Z (25%) than in LWP (10%) therefore the impact on LWP is larger. The bias in Z is propagated in lna, but the bias in LWP directly impacts LWC. The simultaneous biases in Z and LWP have been also tested, which reveals that the bias in LWP is dominating over the bias in Z with 11% MAPE when mentioned biases are considered in Z and LWP.

5.3.5 Sensitivity analysis of LWP assimilation

The impact of adding LWP information in the retreival is evaluted by comparing LWC retrievals in the situation where LWP information is assimilated with those in the case where it is not assimilated. For the case when LWP is not assimilated, the prefactor a is not retrieved and hence kept constant. Different values of scaling factor *lna* are selected from various empirical relations listed in the table 4.1, and the error in retrieved LWC is calculated with respect to true LWC for each fixed value of scaling factor *lna*.

In this subsection, the synthetic profile of Z is fabricated using the power law with constant a and b proposed by [Atlas, 1954] and LWC provided by the AROME model. The table 5.4 contains the scaling factors taken from the empirical relations used to retrieve LWC without LWP assimilation. The MAPE is calculated for retrieved LWC for each *lna* value. In the table 5.4 the highest value of MAPE is observed when $a = 0.012$, and the lowest value is for $a = 0.048$ which is the exact value of *lna* used to fabricate Z. As the value of scaling factor *lna* differs from the scaling factor used to fabricate the synthetic profile (here *lna* from [Atlas, 1954] relation), the error in retrieved LWC w.r.t. true LWC also increases.

Table 5.4: Error in retrieved LWC for fixed a and LWP is not assimilated

Empirical relation	a	*lna*	MAPE (LWC)%
Fox and Illingworth [1997]	0.012	-4.42	109.48
Sauvageot and Omar [1987]	0.03	-3.50	27.956
Krasnov and Russchenberg [2005]	323.59	5.77	98.82
Atlas [1954]	0.048	-3.05	0.0021

On the other hand, when the LWP information is assimilated in the retrieval, the MAPE in retrieved LWC compared to true LWC is 0.171%. However, it is not nec-

essary that the LWP is always accurate, as LWP is also a retrieved parameter and can have random errors. Therefore, one must test the retrieval algorithm when the LWP information is biased. The retrieval technique is now evaluated for different biases in LWP information. As already mentioned, when we assimilate LWP information, the scaling factor can vary. We tested the retrieval with varying biases, as shown in table 5.5. The highest value of LWP in the synthetic profile is approximately 240 gm^{-2}, and the highest bias added in LWP is $\pm 50 gm^{-2}$ which indicates 56 % MAPE in LWC. The error in retrieved LWC due to such high biases in LWP is much less than the error when the diverse value of *lna* are taken in the retrieval. These errors are summarised in the figure 5.6 where the olive green bars indicate the MAPE in LWC for different values of *lna* taken in the retrieval without LWP assimilation. The blue color bars are the MAPE in LWC for various biases in assimilated LWP. It is clear from this comparison that the assimilated LWP, even with bias, has lower error than the retrieval case that do not use LWP assimilation.

Table 5.5: Error in retrieved LWC for various biases in assimilated LWP

Case	Bias (gm^{-2})	MAPE [LWC] (%)
1.	LWP ±5	5.5
2.	LWP ±10	11.23
3.	LWP ±20	22.71
4.	LWP ±50	56

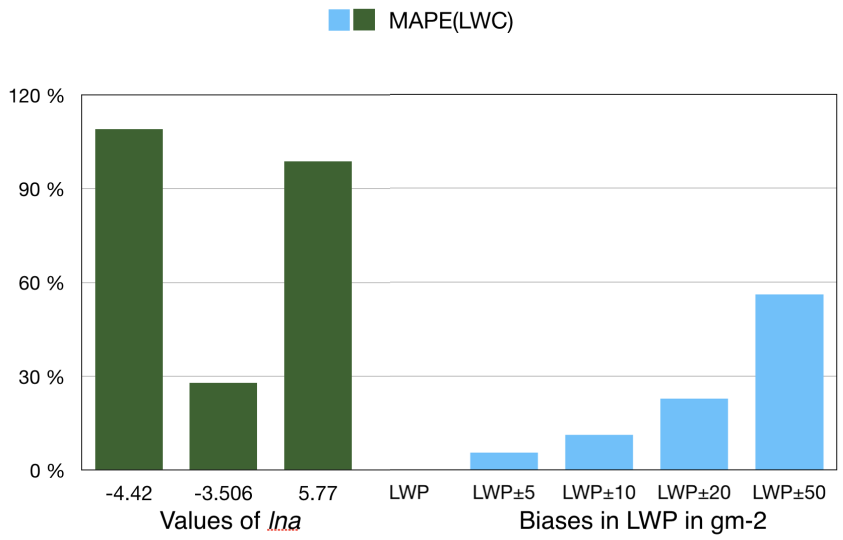

Figure 5.6: Errors in retrieved LWC when LWP is not assimilated, as compared to those when LWP is assimilated with biases. The Y-axis represents the MAPE in LWC, and the X-axis shows the value of *lna* taken from empirical relations and biases in LWP

.

5.3.6 Sensitivity of parameter b

The exponent b from the power law equation (4.7) is considered 2 for all the cases discussed in this chapter, however the range of parameter b in the literature is proposed from 1 to 2. To test the impact of variation in b on the retrieval algorithm, the value of b used to fabricate synthetic observations Z and LWP, and b in the forward model are same. Keeping all the other settings constant, the error in retrieved LWC should be due to changing b. Table 5.6, shows the range of b and the respective error in retrieved LWC with respect to true LWC. The retrieved LWP matches with the assimilated LWP only the distribution of LWC is changed observed least for $b = 2$. Figure 5.3.6 shows that the cost function is also least for $b = 2$ and MAPE in LWC is twice when the value of b is taken 1.

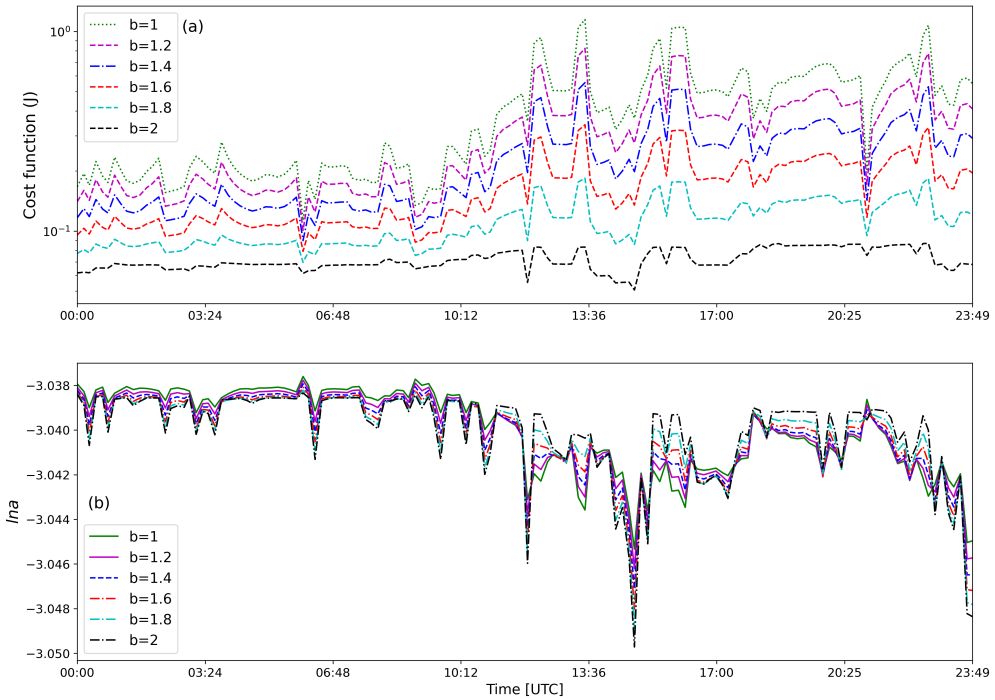

Figure 5.7: (a) Cost function and (b) Retrieved lna for different b values

There is negligible impact of variation in b over lna as shown in figure and the error

Table 5.6: Error in retrieved LWC for different b values

Case	b value	RMSE (LWC)	$R^2(LWC)$	MAPE (LWC)
1.	b=1	0.00069	0.99998	0.35599
2.	b=1.2	0.00064	0.99998	0.301158
3.	b=1.4	0.00059	0.99998	0.260569
4.	b=1.6	0.00054	0.99998	0.227267
5.	b=1.8	0.00050	0.99999	0.198041
6.	b=2	0.00045	0.99999	0.171237

in LWC is between 0.35% to 0.17%. The convergence is achieved with less cost function and MAPE in LWC is also least for $b = 2$ case. Because lna is allowed to be variable in the forward model, it is most likely that the change in b is compensated by the change in lna.

5.3.7 Analysis of the sensitivity exercise

In conclusion, since this sensitivity test was performed on a synthetic profile, the overall impact of uncertainty of each parameter on the retrieval can be very different when applied to a real profile. However, an estimate of errors can be made using this exercise. The error in observation must be chosen very carefully for retrievals. 25% error in Z is also supported by realistic calibration error of BASTA radar which was calculated between 1 and 2 dBZ using 20 m mast [Toledo et al., 2020] where 25% error in Z corresponds to 1.08 dBZ. This combination of 25% and 10% error in measurement has only 0.17% MAPE when tested with synthetic profile, which is why this combination is used in the algorithm. *a priori* must be considered only to stabilize the retrievals for unavailable measurements, otherwise the error in *a priori* can be kept high. A prior is a constraint for the entire retrieval, hence the uncertainty in the retrieval must be smaller than the error in *a priori*. Otherwise, the retrieval does not add any information from the observations [Maahn et al., 2020]. Attenuation by liquid cloud droplets is yet unknown for continental cloud however the available relations from literature proposed for marine clouds is used in the retrievals might bring up to 2.7% error in retrieved LWC. Retrieval is very sensitive to bias in LWP as LWP is point information for whole cloud column, therefore error in observation and biases in Z and LWP both play a very critical role in the retrieval. Sensitivity of retrievals for parameter b is showing the least error when $b = 2$ because this is the same used to fabricate Z synthetic from the true LWC. Nevertheless, it is worth noting even with other values of b the MAPE is not exceeding 0.35%.

5.4 Comparison of LWC retrieval with in-situ data

In-situ measurements of cloud and fog are required to validate the distribution of LWC with time and height. In general, in-situ measurements of cloud microphysical parameters are collected using a research aircraft mounted with sensors flying inside the cloud. During the SOFOG-3D field experiment, a tethered balloon equipped with in-situ sensors was used to collect the microphysical parameters of fog. This approach is much more economical than the research aircraft flying inside cloud, however the trajectory of the balloon cannot be fully controlled, and the measurements are limited to the lower-

most 1–2 km level. Simultaneous measurements using remote sensing instruments like BASTA cloud radar, microwave radiometer and automatic weather stations were also collected for various fog cases [Martinet et al., 2020]. Since the LWC retrieval algorithm described in previous sections essentially works with liquid clouds including fog, measurements collected during the SOFOG-3D experiment are well suited to validate the algorithm. The input for the algorithm is taken from vertically pointing cloud radar reflectivity and LWP estimates from MWR measurements. Retrieved LWCs are then compared with the measured LWC using in-situ sensors.

5.4.1 Presentation of the case study of 09 February 2020

One fog case study observed at the super-site (44.4°N,−0.6°E) on 9th February 2020 is presented to compare retrieved LWC with in-situ measurements collected from the tethered balloon. This case is selected because fog and stratus were observed, allowing us to validate the algorithm for two different cloud types at once. The observations from vertically pointing radar and MWR are used to retrieve LWC with exactly the same algorithm described in previous sections. During this experiment, MWR was set up to collect boundary layer scan at lower elevation angle down to 4° every 10 minutes and therefore the LWP is interpolated for such gaps. Relying on the previously led sensitivity study, error in observations for Z and LWP is taken as 25% and 10% respectively, with *a priori* information calculated from Atlas [1954] empirical relation. Error in *a priori* is considered 1000% which is the same as mentioned in section 5.2.3 when MWR information is available. As stated in section 5.2.3, radar misses a few low level gates near the ground due to antenna coupling, which contains critical fog information. The properties of fog are assumed to remain constant between the first available gates and the ground, and thus reflectivity is extrapolated (extended) downwards for the unavailable range gates. The fog shown in figure 5.8 sustained for 4 hours and then started dissipating to form a stratus cloud. Figure 5.8(a) illustrates radar reflectivity extended to the lowest gates, whereas in figure 5.8 (b) Doppler velocity is plotted only for the available gates. Higher velocity at the fog top are indicating the entrainment process causing the dissipation of fog after 04:00 hours. The visibility observed at the super-site is also less than 1000 m until 04:00 hours. The discontinuity in radar reflectivity close to 200 m is due to the beam overlap correction used in L2 product of BASTA. The distribution of retrieved LWC over time and height is shown in figure 5.8(c) along with the trajectory of the tethered balloon. Figure 5.8(d) and (e) are the plots for LWP and retrieved lna respectively for this case.

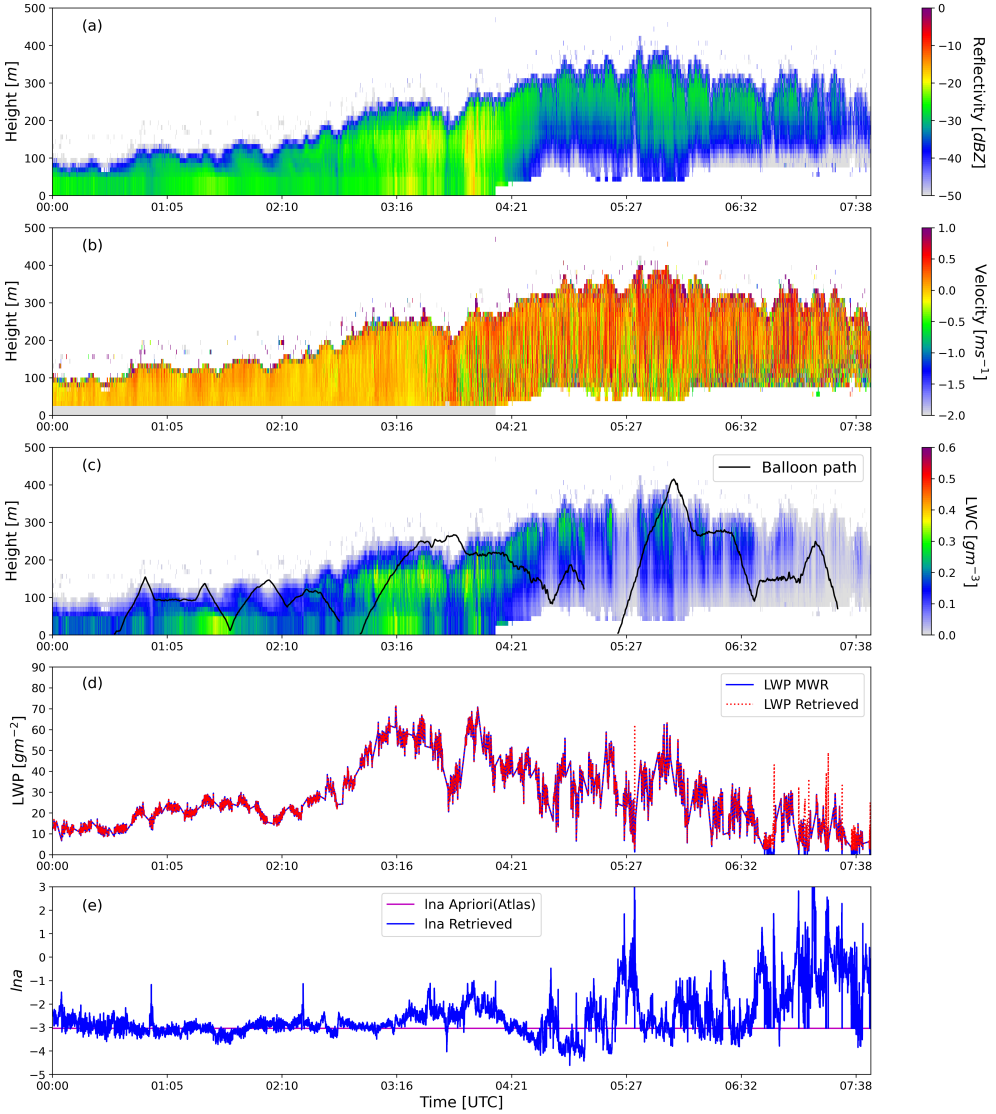

Figure 5.8: (a) Radar reflectivity Z (b) Vertical velocity (c) Retrieved LWC, (d) LWP and (e) Retrieved *lna* for 09 February 2020 case at SOFOG-3D super-site. Tethered balloon trajectory over retrieved LWC is shown in black line.

5.4.2 Comparison between in-situ and radar measurements

To compare the retrieved LWC with in-situ measurement, the co-location of tethered balloon data with BASTA reflectivity points is accomplished by determining the closest radar gate that corresponds to the balloon height. In figure 5.9(b) and (c) the black dashed line indicates that the visibility is more than 1000 m from 04:00 hours onwards and therefore separates fog and stratus cloud. Since the balloon also contaminates

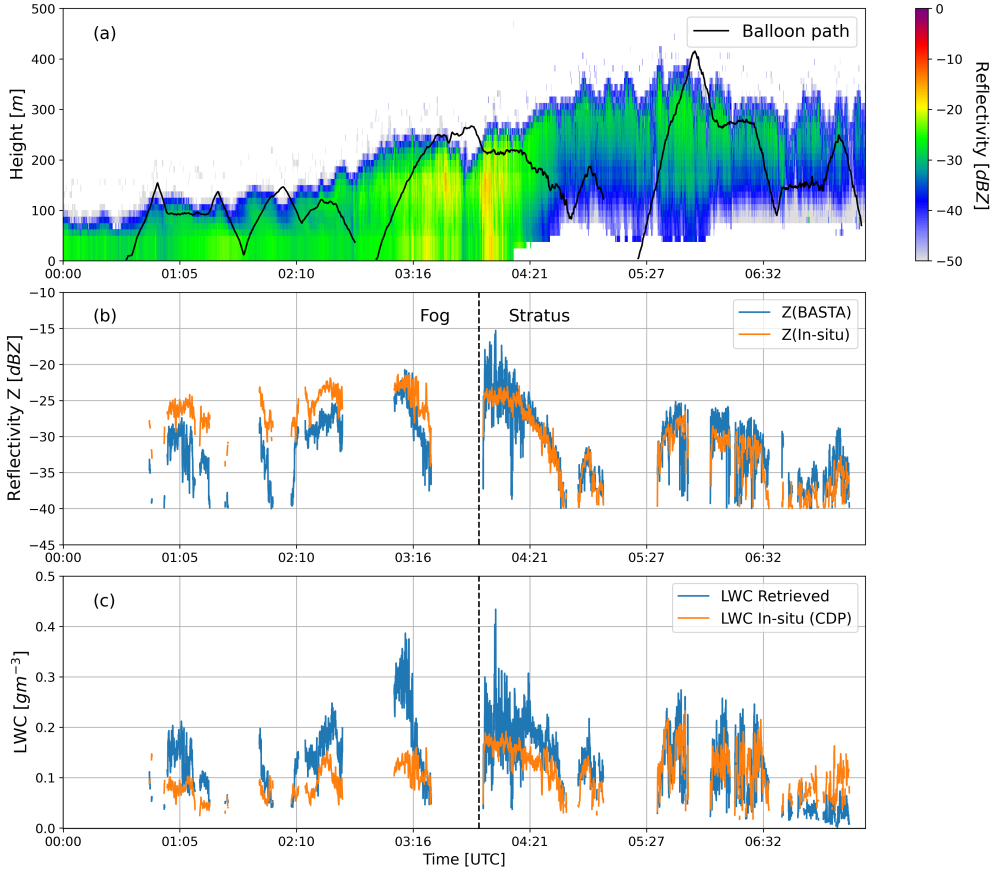

Figure 5.9: (a) Radar reflectivity and balloon path (b) Comparison of radar reflectivity with reflectivity calculated from CDP using DSD at the altitude of balloon (c) Comparison of retrieved LWC with in-situ LWC at the altitude of balloon.

the radar measurement, therefore all the co-located points when the tethered balloon was within the radar detection range are eliminated. The maximum distance observed between the tethered balloon and BASTA radar was 700 m. Radar reflectivity factor from in-situ measurements is calculated using the 6th moment of the droplet distribution measured by CDP. Note that the radar reflectivity is still in the Rayleigh regime as the measurements from CDP cannot exceed 50 μm. The co-located points with reflectivity less than -40 dBZ are masked because the signal-to-noise ratio for radar is low.

In figure 5.9(b) the radar reflectivity from BASTA and CDP are compared for the co-located points and indicates a clear bias for fog and relatively much better agreement

for stratus cloud with -4.44 dBZ mean bias for fog and 0.89 dBZ for stratus cloud. The bias is calculated as the difference between Z_{BASTA} and $Z_{in-situ}$. The root mean square error (RMSE) in Z is 5.2 dBZ for fog and 2.8 dBZ for stratus. Figure 5.9 (c) shows the comparison of the retrieved LWC values with LWC observed by CDP at the co-located points of the balloon trajectory. The mean bias in LWC for fog is 0.06 gm^{-3} and for stratus cloud is 0.009 gm^{-3}. The root mean square error (RMSE) in LWC for fog is 0.082 gm^{-3} and 0.056 gm^{-3} for stratus. The comparison of retrieved LWC with in-situ observations of LWC from CDP resulted in a root-mean-square error of 0.067 gm^{-3} including fog and stratus.

For a well-calibrated radar, the reflectivity estimated from in-situ sampling should match with the radar reflectivity if both the instruments are sampling the same cloud column and have a similar sensitivity to DSDs. The sensitivity of the CDP sensor is limited to sample the droplet diameters from 2 to 50 μm, while radar can sample a wider range of DSDs and is more sensitive to the largest droplets. The variations in comparison with in-situ observations are noticed when the balloon is close to the cloud edge, where a slight difference in altitude can have a significant impact on Z and LWC due to the heterogeneity of this area.

The observed differences in simulated Z and radar measurements could be explained by the vertical and horizontal heterogeneity of the fog, which strongly depends on the fog maturity. To further investigate the fog stages, a broader perspective beyond the vertical profile of fog is required. Multiple remote sensing and in-situ instruments were operated simultaneously as part of the SOFOG-3D campaign to explore various fog properties. A 95 GHz scanning radar called BASTA-mini has been centered 1 km away from the vertically pointing radar, and the 360° scan of fog is presented in figure 5.10(a) and (b). Plane Polarised Indicators (PPI) of scanning radar shown in figure 5.10, are collected at 4° elevation angle. Note that this low elevation of radar can also be contaminated by the ground clutter, indicating locally high reflectivity. In the figure 5.10(b), a larger spread of fog is observed, which is due to the development of thicker fog.

Due to the constant evolution of fog stages and the horizontal heterogeneity of fog, the sampled volume away from the vertically pointing radar will also have distinct Z and LWC. As shown in figure 5.10(b), the distribution of reflectivity in the left and right-hand side of scanning radar is different. Therefore, the mismatch in Z and LWC can be explained by different radar and CDP sampling volumes. As the fog lifted into stratus cloud around 04:00 hours, we can observe a better agreement in figure 5.9(b) and (c), which could be explained by a more homogeneous situation. Furthermore, as shown in figure 5.9(a), samples are not collected at the cloud edge for stratus and therefore have lesser uncertainties in Z and LWC.

In order to have a better idea of the representativeness of CDP in-situ data, a scatter

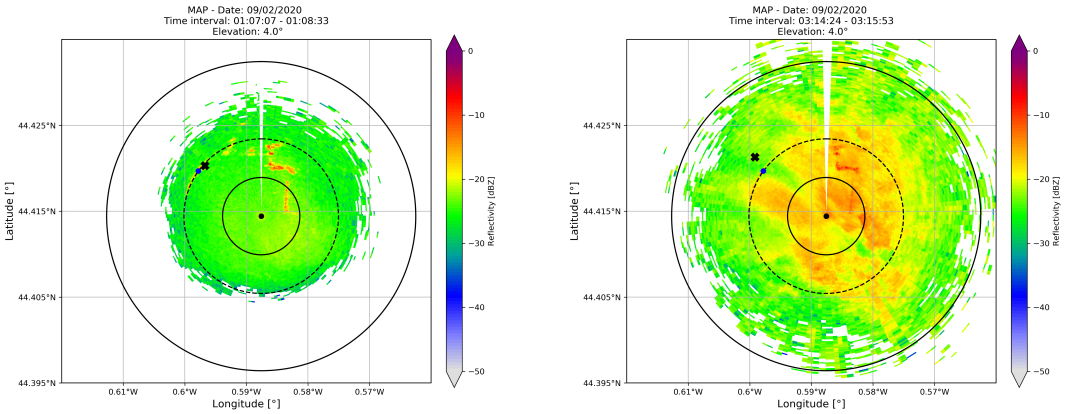

a) Scan at 01:07 hours b) Scan at 03:14 hours

Figure 5.10: Scans of BASTA-mini collected for fog at 4° elevation angle. The vertically pointing radar shown as a blue dot was located 1 km away from the scanning radar and the cross represents the location of the balloon

plot of retrieved LWC with radar reflectivity from BASTA radar and in-situ measurement of LWC with simulated radar reflectivity using DSD compared with empirical Z-LWC relationships in figure 5.11. In-situ measurements are separated for fog and stratus clouds where magenta colour denotes fog, yellow-green (Chartreuse) colour denotes the stratus cloud, and the respective linear fits are also plotted. Various Z-LWC relations for clouds are included in table 4.1, but are not proposed for fog. In Dupont et al. [2018], linear fits for fog are proposed based on in-situ observations from the tethered balloon and BASTA cloud radar at SIRTA. As a reference for fog, Flight1, Flight2, and Flight3 in the figure 5.11 are the fits for three fog instances computed by relating LWC observations from a light optical aerosol counter (LOAC) sensor to BASTA measurements, as described in Dupont et al. [2018]. These Z-LWC fits for fog are obtained by finding the linear fit of LWC from LOAC sensor to the radar reflectivity Z of the closest gate from vertically pointing BASTA radar. We compared the behaviour of in-situ fog measurement during the SOFOG-3D campaign to that of other fog relationships. As illustrated in figure 5.11, no empirical relation from the literature, including the one derived in fog, seems to be able to represent the in-situ observations of this fog situation. However, the scatter for in-situ measurements of stratus represents a good correlation with other empirical relations as well as with the linear fits for fog from Dupont et al. [2018]. The in-situ measurements separated for fog and stratus clearly show different characteristics and also indicate that different reflectivity values for the same LWC can be obtained, as shown in figure 5.11. This could be because of the diverse droplet spectra in stratus and fog.

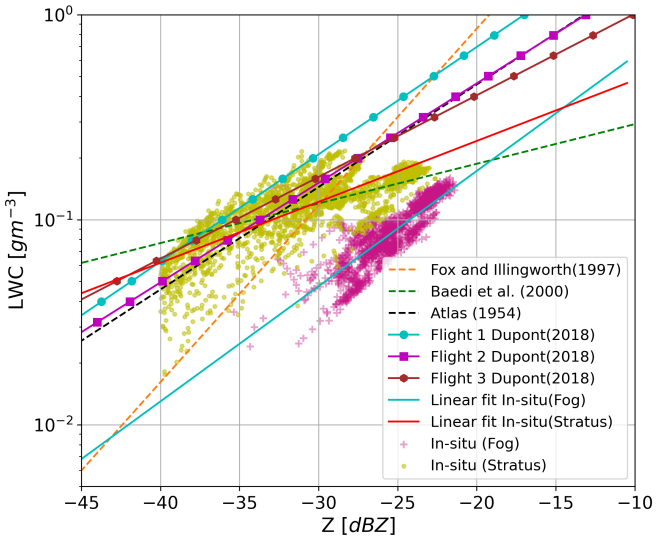

Figure 5.11: Comparison of in-situ LWC and radar reflectivity relation with available literature for fog and clouds

The impact of various DSD characteristics during the fog stages in the simulation of different radiation fogs is discussed in Maier et al. [2012]. In the Raleigh regime Z values might get larger as fog develops due to the increase in droplet radius, while the LWC may remain constant. This introduces a non-linear relation between LWC and radar reflectivity Z. The variability within each fog stage exhibited unique properties depending on the fog event [Maier et al., 2012].

In figure 5.12 the retrieved LWC from the algorithm with respect to BASTA reflectivity is plotted in blue scatter, and it matches only with the in-situ observations for stratus and other empirical Z-LWC relations. In-situ fog indicates relatively less LWC than stratus cloud at the same radar reflectivity. For the sake of comparison with Dupont et al. [2018], we also related the in-situ LWC obtained during SOFOG-3D with co-located radar reflectivity from BASTA. By correlating in-situ measurements of LWC with cloud radar reflectivity, it is assumed that the radar and in-situ sensor are observing the same cloud volume; however, distance between the balloon and the nearest gate of cloud radar can incorporate uncertainties. In addition to this, the sensitivity of the in-situ sensor (CDP) and radar (BASTA) is considered the same, despite the fact that the sensitivity varies with DSDs. Generally, the cloud probes under sample the true DSD of the volume due to their limited sensitivity to droplets. As shown in figure 5.13, the Z-LWC fits from in-situ observation are in neighborhood to other empirical relation for reflectivity less than -30 dBZ. Since the power-law relations are valid only in the Rayleigh regime, the in-situ observation agrees with other empirical relations for low reflectivity. Reflectivity values greater than -30 dBZ may be attributed to larger droplets, which may or may not include a higher LWC. However, a significantly better correlation

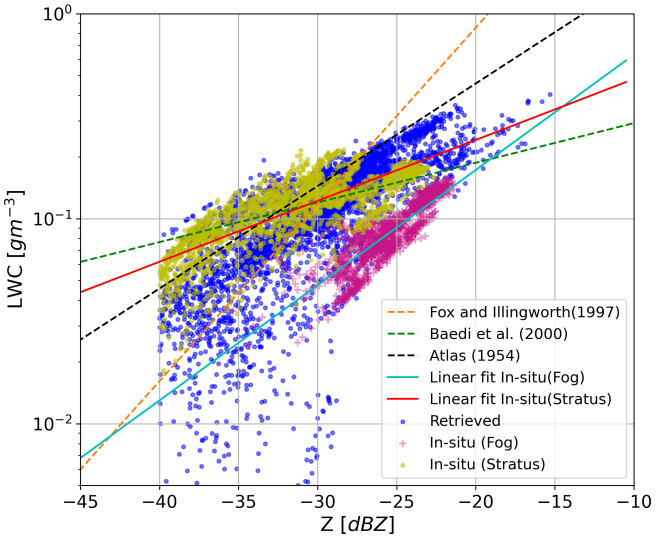

Figure 5.12: Comparison of in-situ LWC and radar reflectivity relation with retrieved LWC and BASTA radar reflectivity relation

of in-situ fit for stratus cloud with empirical relation by Baedi et al. [2000] (proposed for stratocumulus clouds) indicates representativeness of in-situ observations for stratus. The fit for in-situ fog observation still indicates less LWC at the same reflectivity and does not match with any empirical relation. These observations imply that these are either collected for large droplets beyond the CDP limit or from a sampling volume distinct from the one cloud radar samples.

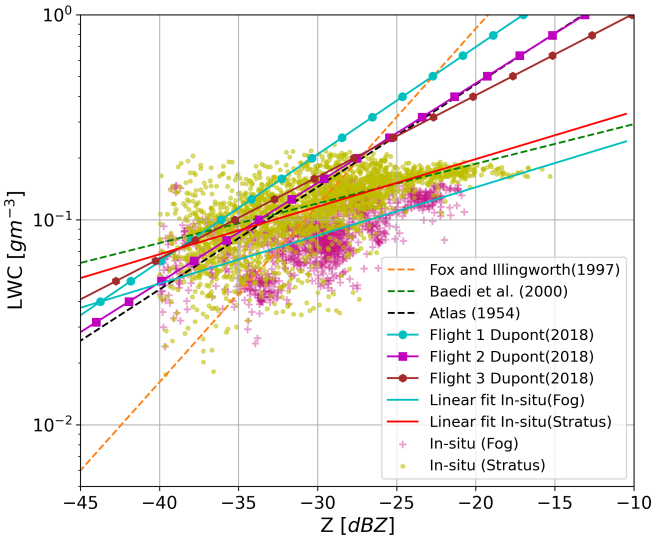

Figure 5.13: Scatter plot for relation between LWC measured from CDP with radar reflectivity from cloud radar, compared with available literature

Unfortunately, the limited in-situ observations collected for fog and stratus here do not represent a validation of the retrieval; however, this comparison highlights that there are situations more complicated than the other. Due to the non-uniform distribution of

LWC in cloud or fog, homogeneity plays a key role while validating with the in-situ measurements. It is unfair to expect LWC to match when simulated reflectivity from in-situ does not match radar measurement. In order to validate such an algorithm, in-situ measurements at different heights for the same volume that radar samples are needed. However, if the in-situ observation platform is positioned in proximity to the radar sampling volume, it may also contaminate the radar observations. Therefore, the in-situ measurements must be collected from a homogeneous cloud to compare with the retrievals. Particularly for fog, more continuous DSD measurements as well as the vertical profiles during distinct fog episodes are required to produce more significant results.

5.5 Statistical analysis of retrievals to derive climatology

The primary objective of this statistical analysis is to derive a climatology of LWC and *lna* in order to allow the algorithm to be able to retrieve LWC for fog and low-level liquid clouds even when additional measurements are not available. A comparison of retrieved LWC with in-situ LWC measurements for fog and stratus cloud from the SOFOG-3D experiment is already presented in section 5.4.1. In this section, the climatology is developed from the retrieval technique discussed in section 5.2.5 using the larger data set from SIRTA measurements for a variety of cloud and fog incidents that occurred between November 2018 and May 2019. Statistical analysis to derive a climatology of LWC and scaling factor is presented in this section. Figure 5.14 presents the histogram of observed parameters followed by retrieved parameters for the selected observation set.

The histogram of the retrieved scaling factor *lna* indicates that, the highest values of occurrence are around -3 which is close to the *lna a priori* value from [Atlas, 1954] the empirical relation plotted as the red line, but it is not precisely the same. The variational framework allows variability in the *lna* retrieval. The assimilation of LWP brings enough information to retrieve *lna* and the spread around the *a priori* value is directly linked to the *a priori* error value. Table 4.1 indicates the *lna* values for various cloud types proposed in the literature, which agree well with the range of retrieved *lna* values. Note that there is one single *lna* value for a given profile, but its value can potentially be used to differentiate clouds from drizzle. All the profiles with rain and drizzle reaching ground are removed for the statistics, however light drizzle with clouds and fog is discussed.

Since the algorithm does not assimilate LWP for the profiles with LWP less than 10 gm^{-2}, LWP histogram in the figure 5.14(b) has no value below 10 gm^{-2} and the LWP for the majority of cloud profiles is less than 120 gm^{-2}, but some profiles have a value

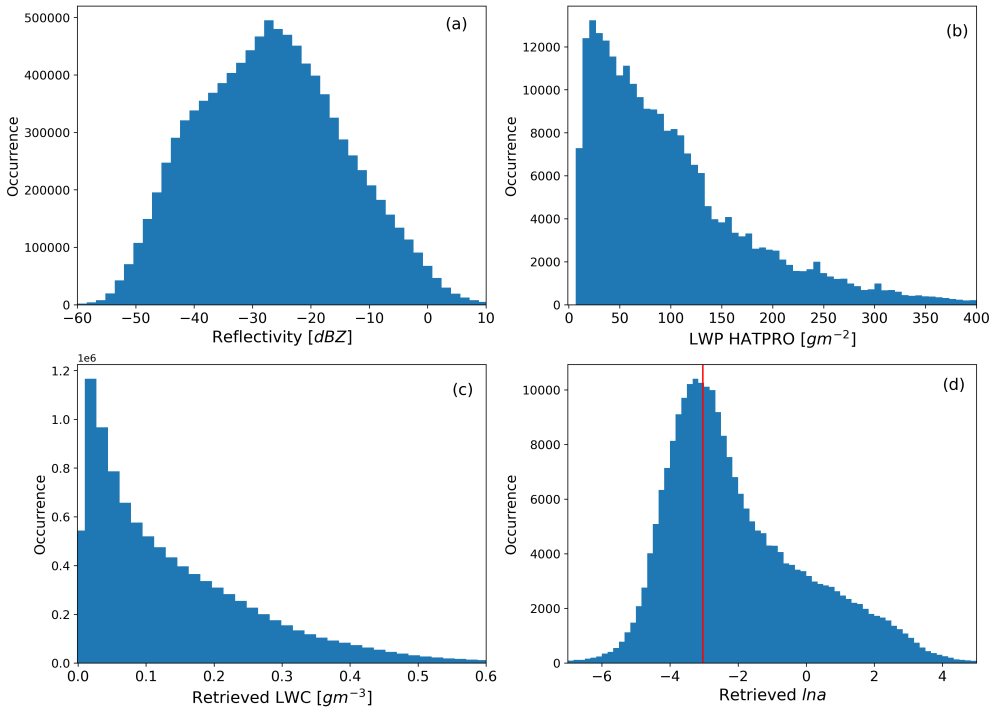

Figure 5.14: Histogram of (a) Radar reflectivity(Z) (b) LWP from MWR (c) Retrieved LWC (d) Retrieved *lna* for 39 cloudy days, and the red line in *lna* histogram indicates the *a priori* of *lna* from table 4.1

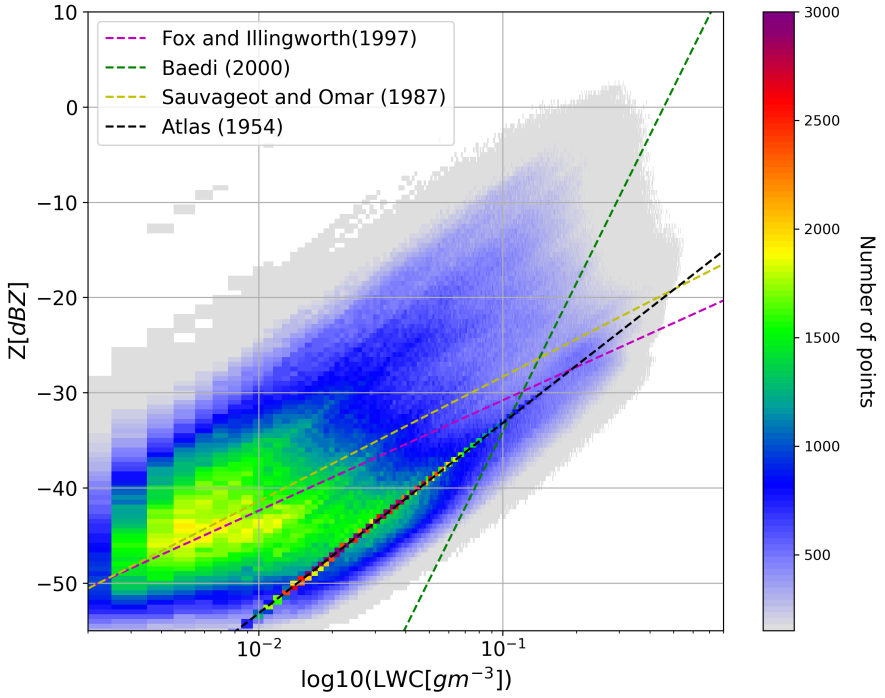

Figure 5.15: Retrieved LWC as a function of radar reflectivity Z for 39 cloudy days, with reference plot of various empirical relation for different cloud types.

of LWP up to 400 gm^{-2}.

The parameter LWC is indicating the range up to 0.6 gm^{-3} which includes light drizzle, while the highest number of cloud pixels have LWC value less than 0.2 gm^{-3}. In figure 5.15, retrieved LWC is plotted as a function of radar reflectivity for the 39 cloud cases, with Z-LWC empirical relationships from literature for various cloud types. The black line represents *a priori* of the retrieval algorithm, and the higher concentration of density points overlaps with the black line is due to the profiles with LWP<10 gm^{-2} where the retrieval of LWC is based on only Atlas empirical relation. All these profiles are not considered in the climatology of lna. However, the wide range retrieval points indicates that the algorithm allows LWC retrieval for a variety of cloud types. The slope of Z-LWC relationship is dependent on the value of b in equation 5.7 and because the retrieval method considers $b = 2$, the slope of the total retrieval in figure 5.15 is constant. However, retrieval allows variability in lna which could partly compensates for b as well.

As already described, knowing LWP allows us to retrieve lna and adjust the relationship between LWC and Z. However, when only BASTA measurements are available, we need to rely on an *a priori* value for lna. Thanks to this climatology we could both define the optimal value for this *a priori* and also eventually propose to parametrise this value, for instance it is envisioned to relate the scaling factor to radar reflectivity and/or Doppler velocity. As Z and V are observed for each cloud pixel and only one value of lna is retrieved for a given cloud profile, one single reflectivity or velocity information should be associated with lna. We propose to summarise the reflectivity and velocity information to the mean or maximum value of the profile, in order to have one value per profile.

Maximum and minimum velocities of the cloud column are associated with the updrafts and downdrafts, which may not represent the complete profile for lna. Therefore, we rely on the mean velocity of the profile. The density plot of mean velocity as a function of lna is plotted in figure 5.16(a) indicating that mean velocity of most profiles is concentrated between -0.5 to 0.1 ms^{-1} which is compatible with liquid cloud sedimentation velocity. Mean velocity close to 0 ms^{-1} with lna values ranging from -4 to -2 implies pure clouds, whereas few profiles with the mean velocity less than -0.5 ms^{-1} must be impacted by the drizzle droplets in the profile. Standard deviation plotted in the red line indicates that the variability of lna is very high for the profiles with mean velocity below -0.5 ms^{-1}. Due to the large standard deviation, lna cannot be associated with mean velocity, however velocity information can be used to classify drizzle droplets. As illustrated in figure 5.16(b), a substantially stronger association is observed between maximum radar reflectivity and lna of the profile. For most of the cloud columns, maximum reflectivity is observed between -30 to -15 dBZ. As maxi-

mum reflectivity also represents the drizzle in cloud, the maximum reflectivity above -10 dBZ is suspected to indicate drizzle in cloud. High value lna for reflectivity above 0 dBZ, also supports the empirical relation for drizzle by Sauvageot and Omar [1987] as shown in table 4.1 where the lna is given as 5.77. The standard deviation of lna is also high for profiles with maximum reflectivity above -10 dBZ. The standard deviation of lna is lowest between -30 to -20 dBZ. The one-dimensional linear fit relating lna and maximum radar reflectivity for clouds columns, is shown in black dashed line in figure 5.16 (b). As maximum reflectivity of the profile is showing better correlation with lna and the mean lna (red dashed line) coincides with linear fit. Therefore, the one dimensional linear equation relation between lna and maximum reflectivity(Z_{max}) is given by

$$lna = 0.186 \cdot Z_{max} + 1.829 \tag{5.15}$$

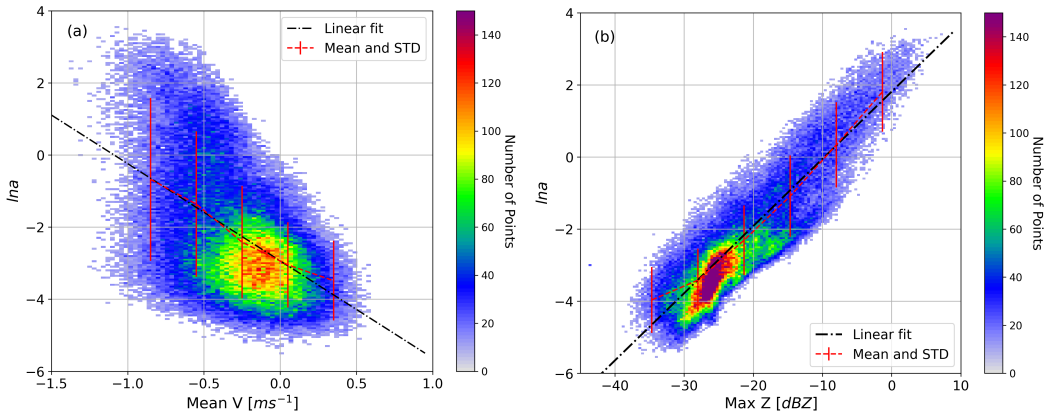

Figure 5.16: Correlation of (a) Mean velocity of the profile versus lna and (b) Maximum reflectivity of the profile versus lna for each cloud profiles, where colour bar indicates the number of profiles

However, from an investigation by selecting 15 fog cases out of 39 cloud cases indicated that the coefficients of linear fit are slightly different for fog profile.

$$lna = 0.149 \cdot Z_{max} + 0.591 \tag{5.16}$$

To utilize the above relationships, it is necessary to differentiate between liquid cloud aloft and fog. This can be easily done by determining the cloud base height to identify fog, and hence specific climatology is applied to the profile.

5.6 BASTA standalone LWC retrieval using climatology

In this section, we describe the stand-alone approach and its assessment using MWR LWP retrieval as a reference. The climatological relation of *lna* as a function of maximum radar reflectivity in the profile is used for the BASTA standalone retrieval when MWR observations are unavailable.

5.6.1 BASTA standalone LWC retrieval approach

The radar is not always accompanied by a MWR and therefore a solution must be proposed to improve the retrieval with knowledge of *lna a priori*. Since LWP information is not assimilated, thanks to the *lna* climatology for clouds and fog derived in section 5.5, this information can be used as *lna a priori*. *lna* for the profile can be linked to the maximum value of reflectivity detected in the profile using equation (5.15) and (5.16) for clouds and fog respectively.

In this case, the observation vector 'y' contains only radar reflectivity of each cloud pixel, with 25% error in measurement, whereas the state vector still contains LWC and *lna* both. Therefore, the Jacobian for a cloud profile with n cloud pixels will have $n \times (n+1)$ elements. The variational method also allows us to control the contribution of *a priori* information in the retrieval by providing error in *a priori*. A strong *a priori* of *lna* is required to constrain LWC retrieval therefore, low error in a priori of *lna* is employed. In these standalone retrieval cases, 100% error in *a priori* of *lna* is used, because the standard deviation of *lna* in figure 5.16 is approximately 1 which is equivalent to 100% error in *a priori*. The climatology of *lna* for fog from equation (5.16) is applied to the profile with cloud base less than 80 m. Retrieval of LWC should be constrained by LWC *a priori* only to avoid non-physical values, therefore the error in *a priori* of LWC is taken 1000%. In BASTA standalone retrieval setup, *a priori* of LWC is calculated using Atlas [1954] relation exactly the same as radar-MWR synergistic retrieval.

5.6.2 BASTA standalone LWC retrieval first assessment using LWP retrieved from MWR

With the details given above, LWC retrieval algorithm is adapted to utilize climatology of scaling factor with only radar reflectivity measurements from SIRTA. BASTA standalone retrieval algorithm is applied to the 39 selected cloud and fog cases from SIRTA.

Due to the absence of in-situ sensors at SIRTA for recording the distribution of the LWC in cloud and fog, the integrated LWP from the HATPRO microwave radiometer is utilized to assess the quality of the retrieved LWC for BASTA stand-alone retrieval.

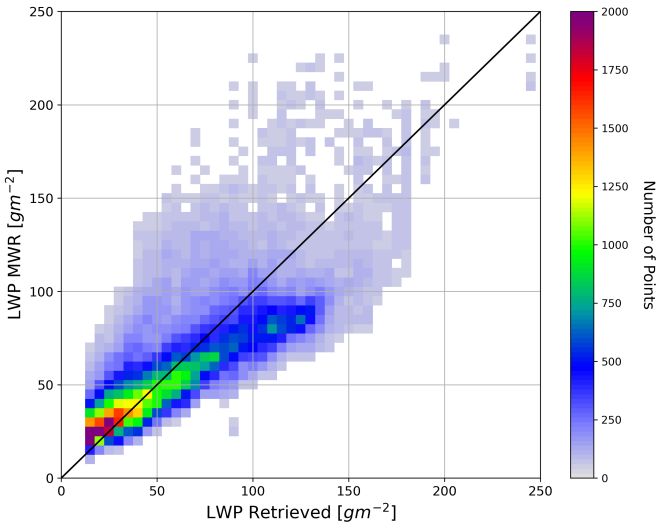

Figure 5.17: Comparison of retrieved LWP with LWP retrieved by HATPRO, where the black line represents the exact match of LWP for given profile.

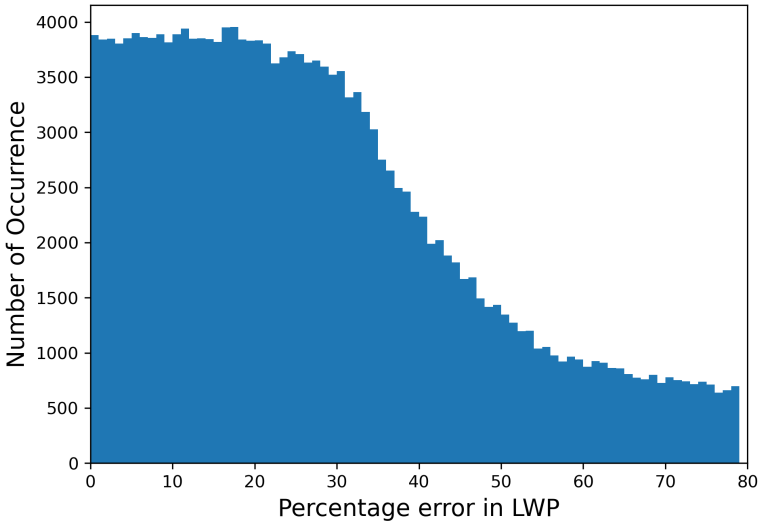

Figure 5.18: Percentage error in retrieved LWP with respect to LWP measured by MWR at SIRTA.

The retrieved LWP is calculated by vertically integrating the retrieved LWC. Because LWP information is not assimilated and strong *lna a priori* derived from climatology is constraining the retrieval, and hence *lna* is not a retrieved parameter. However, the variational framework allows *lna* to adjust around its climatology depending on radar reflectivity. In this case *lna* values falls within the range of known values from literature as shown in table 4.1.

Figure 5.17 presents the comparison of retrieved LWP from BASTA stand-alone retrieval with LWP retrieved from HATPRO microwave radiometer. Number density of profiles with LWP ranging from 10 to 250 gm^{-2} are compared with LWP from

BASTA stand-alone retrieval. Profile with retrieved LWP less than 50 gm^{-2} shows good agreement with LWP from HATPRO. For the profile with higher LWP an increase in bias is clearly observed in figure 5.17, and the mean bias in LWP obtained as the difference between LWP from HATPRO and retrieved is -21 gm^{-2}. The mean absolute percentage error in LWP w.r.t. LWP from HATPRO is 57.15%. The relative error in LWP shown in figure 5.18 indicates that the majority of clouds has less than 35% error in retrieved LWP. Because the climatology of the scaling factor constrains the retrieval, effective estimation of LWC can be made using only radar information when additional information is unavailable. By investigating the origin of biases, we discovered that the profiles with light drizzle droplets characteristics tend to overestimate the LWP by a large margin. The improvement in standalone retrieval can be made by classifying clouds with and without drizzle and using specific lna climatology for them.

The next chapter concludes this thesis and suggest the possible improvement in the retrieval algorithm.

Chapter 6

Conclusion and outlook

The liquid water content of warm clouds (including fog) is a fundamental parameter for characterizing their microphysical properties. The primary objective of this thesis was to develop an algorithm which allows one to retrieve water content from the combination of the BASTA cloud radar and a microwave radiometer. Various aspects of developing this algorithm are covered in this thesis, which are summarised in the next section. I will also recall the current limitations of the method and introduce some potential ways to improve the methodology.

In addition to the scientific question of liquid clouds, my work is also related to the industry. Another aspect of this research is to find new markets for the BASTA cloud radar. Users with no particular radar scientific expertise could appreciate an LWC product for liquid clouds and fog using radar measurements that can be automated. My retrieval is also constrained by the current measurement capabilities of this radar, which explains that I mainly use the reflectivity as information.

6.1 Conclusion

The vertical structure of low-level clouds has been demonstrated to be inaccurately represented by many climate models [Nam et al., 2012]. These uncertainties in the climate projections are due to the poor representation of the cloud microphysical properties in the models. Understanding low-level cloud dynamics under changing atmospheric circumstances will help to minimize model uncertainty and climate sensitivity [Bony and Dufresne, 2005]. To support the improvement in representation of cloud microphysical processes, long-term and continuous observations of clouds are crucial on local and global scales. The introductory chapter 1, presents the motivation to focus on clouds and their observations. In chapter 2, I presented the fundamentals of clouds in the atmosphere and their interaction with radiation. The concepts of Earth's radiative equilibrium and the climate implications of diverse clouds have been introduced.

Cloud radars are ideal remote sensing instruments to scan multi layered clouds with which we can determine macrophysical features such as cloud base and cloud top as well as microphysical features such as water content. A brief discussion on various remote sensing and in-situ measurement techniques for cloud observation are discussed in chapter 3. Since the interaction of atmospheric constituents with radiation changes with wavelength, therefore measurements of clouds at different wavelength can reveal different information. Hence, we also introduced the potential of the combination between active and passive sensors. Synergy of cloud radar with lidar is used for separating drizzle in radar volume and determining cloud and fog base. The synergy of passive microwave radiometer with radar showed significant improvement in LWC estimation by adding integrated water content to scale the LWC estimate, and therefore this synergy is employed in this retrieval algorithm.

The microphysical parameters of liquid water cloud and the quantities measured by remote sensing instruments mentioned above can be related under certain assumptions. Considering capabilities of cloud radar observations, chapter 4 of this thesis highlighted several methodologies and prerequisites for converting the radar observations into LWC. For improvement in the accuracy of LWC estimation, prerequisites such as the classification of hydrometeors is a significant aspect of radar application. Because each hydrometer have certain characteristics, and therefore their retrieval methods are different.

Chapter 5 contains the main part of my work and its content has been submitted to the Atmospheric Measurement and Techniques journal. An algorithm for LWC estimation of warm clouds is proposed using a vertically pointing radar and microwave radiometer synergy. This algorithm is based on the hypothesis that LWC is related to reflectivity with a power-law fit, and one of the constants of the Z-LWC relationship (equation 4.7) is allowed to vary according to LWP of the same cloud profile which is retrieved by a colocated MWR. The scaling factor lna of the relationship, is retrieved while the exponent b is assumed constant. Therefore, the technique proposed in this study is equivalent to finding a suitable Z-LWC relationship consistent with the measured LWP for each cloud profile. This synergistic retrieval algorithm works seamlessly for liquid clouds and fog without prescribing the cloud type. The uncertainties in the retrieval are analysed in the sensitivity analysis of the algorithm. The retrieval algorithm is tested on a synthetic profile for different perturbations in sensitivity parameters. This sensitivity analysis is useful to identify how much the variations in the input variables and errors impact the estimated LWC.

Furthermore, the retrievals are compared against in-situ measurements for a fog and cloud case collected during the SOFOG-3D field campaign. The comparison of LWC values estimated using this synergistic retrieval algorithm revealed that LWC was

more consistent with stratus cloud than fog. From this experience, we note that a homogeneous cloud system is required for the comparison of retrieved LWC with in-situ measurements, or else the in-situ sensors must sample the same cloud or fog volume as radar. To assess the accuracy of algorithm for LWC estimates in various clouds types, in-situ measurements of several types of warm clouds like fog, low level stratus clouds with and without drizzle are required.

The proposed algorithm is implemented to a set of cloud and fog instances observed at SIRTA and the analysis is discussed in this thesis. The observations of cloud and fog instances from several months are utilized to build a climatology of LWC and scaling factor. The application of derived climatology to estimate LWC for stand-alone radar observations is also presented. By utilizing the climatology of the scaling factor, this radar stand-alone method can provide continuous retrieval of LWC for warm clouds even in the absence of radiometer and other additional measurements. The standalone method uses climatology of scaling factor as *a priori* information that allows the variability in the LWC retrieval in the stand-alone mode. Such climatologies can be helpful in establishing new retrieval methods for low-level clouds.Although this climatology is developed using measurements from SIRTA observatory for limited cloud scenarios, a more extensive data collection from several measurement locations might be used to generate a more robust climatology of scaling factor.

6.2 Outlook

Although the current retrieval technique provides LWC estimates of liquid clouds and fog, some improvements can still be made in the retrieval algorithm. The perspectives of possible future investigations are presented in this section. Note that the BASTA radar will have some new capabilities in the future that could benefit to the LWC retrieval (for instance the Doppler spectrum information).

The retrieval algorithm could be updated with an improved target classification scheme to apply two different scaling factors in one profile, especially when drizzle and cloud co-occur. Also, for multi-layered liquid clouds, different lna might be prescribed for each cloud layer with proper classification of hydrometeors. Improved classification of hydrometers for the BASTA stand-alone retrieval will improve the LWC retrieval because the range of scaling factor varies for different categories. Further, the climatology of scaling factor for different cloud types will improve the LWC retrieval. As mentioned in the section 5.2.4, the radar reflectivity profiles can be contaminated by particles in the boundary layer. In the retrieval method, these airborne planktons must be categorized and hence not processed as hydrometeors. Ultimately, a sophisticated algorithm for the classification of hydrometeors to distinguish between fog, liquid cloud,

drizzle and airborne planktons (non-hydrometeor) is necessary.

Drizzle in clouds is a substantial source of error in the retrieval. In general, the liquid water clouds and fog can have bimodal populations of drops, which means that the droplets in the clouds are of two characteristic droplet size, one representing cloud droplets, the other of drizzle-sized drops. Because drizzle droplets are significantly larger than cloud droplets, power law may not be applicable in the Mie regime. As a result, the forward model exclusively for drizzle must incorporate Mie scattering or eventually another kind of relationship to link Z and LWC. A prospective work for such cloud columns is planned to separate drizzle and cloud pixels using Doppler velocity information and develop a forward model for drizzle. The variational framework discussed here can be modified to incorporate additional measurements, such as Doppler velocity.

Another current limitation of our synergistic retrieval method is that it is applicable to profiles with LWP values greater than 10 gm^{-2}. A better *a priori* of lna can be proposed in future to estimate accurate LWC for low LWP profiles. Additionally, this retrieval method is not applicable when a mixed phase cloud overlap the liquid cloud layer, whereas ice cloud above the liquid cloud does not impact the LWC retrieval of the liquid layer. Therefore, the retrieval methods focusing on mixed-phase clouds can be developed.

While validating the LWC retrievals with in-situ measurements, the colocation of the in-situ probe and radar volume is necessary (homogeneity is the key of the comparison as the volume sampled are not the same). We used in-situ measurements from the tethered balloon platform which was limited for fog observations, however the retrieval algorithm can be validated with in-situ measurements from aircraft or UAVs flights with in-cloud sensors for diverse liquid clouds. A variety of in-situ sensors could be utilized for validating retrieved LWC at different height. Since UAVs and balloons travel at a slower speed than airplanes, which would allow them to sample the clouds more thoroughly. Note that some sites cannot be overflown by aircraft for safety reason. UAVs can be more efficient in terms of controlling them remotely, as the path of tethered balloons cannot be controlled. These platforms can, however, interfere with the radar signal. In order to avoid contaminating the radar signal, the samples must be taken from a volume that is close enough and least obstructing the radar. Before comparing the estimated values with in-situ data, it is necessary to verify if the cloud volume represented by radar and in-situ sample are the same. A well mixed or homogeneous cloud systems is ideal for validating such algorithms.

Although single ground based radar measurement may not yield a reliable estimate of the cloud properties, a prolonged series of observations can help to develop climatologies for different geographical locations and provide information on the regional variation in

the nature of warm clouds. Therefore, ground-based remote-sensing networks should be supported and extended because they represent an indispensable tool for measurement of parameters that are not accessible from space.

As the majority of radars are equipped with Doppler capability, the recorded Doppler spectra also be might be used to improve the categorization of hydrometers. Another possibility is to incorporate machine learning approaches to distinguish the hydrometeor seen by radar. Because Doppler spectra also give information about the droplet spectrum and its variability, and therefore LWC retrieval method can be improved for varying spectra.

The integration of multiple remote sensors is the reliable approach to generate more precise LWC profiles. Cloud radars with multichannel passive microwave radiometers and lidar can provide a more comprehensive view of clouds at multiple wavelengths, and the estimation of cloud microphysical properties is more accurate. Using such synergies, improvement in representation of clouds in climate models can be attained.

In order to improve this LWC retrieval algorithm in future and develop a LWC product, the implementation of the retrieval method for long-term data sets of various cloud cases under a variety of climatic conditions is essential to better depict the diversity of clouds and identify scenarios in which the retrieval works and those in which it does not. The resulting long-term statistics of the cloud property retrievals will provide additional information on the sensitivity, the uncertainty and other limitation of warm cloud retrievals. This could be useful in refining our approaches for estimating LWC using cloud radar measurements.

There are many ways to improve the algorithm with sensors synergies and better parameterization. It is also worth emphasizing that synergistic techniques, combining other radars working at different frequency bands, MWR, and lidar, can improve the retrieval algorithm. Measurements from radar and lidar integrated unit such as BALI could be useful for improving the algorithm. Long-term measurements using well-calibrated remote sensing instruments will ultimately help us better understand the relationship between clouds and other fine-scale processes in the atmosphere.

Bibliography

Hydrometeor - Glossary of Meteorology. URL https://glossary.ametsoc.org/wiki/Hydrometeor.

EUREC4A: EUREC4A. URL https://eurec4a.eu/.

Cloud liquid water content, drop sizes, and number of droplets. URL http://www-das.uwyo.edu/~geerts/cwx/notes/chap08/moist_cloud.html.

Sea2Cloud. URL https://sea2cloud.wordpress.com/.

SoFog3D - National Centre for Meteorological Research. URL https://www.umr-cnrm.fr/spip.php?article1086.

Classifying clouds, Jan. 2017. URL https://public.wmo.int/en/WorldMetDay2017/classifying-clouds.

C. Acquistapace, S. Kneifel, U. Löhnert, P. Kollias, M. Maahn, and M. Bauer-Pfundstein. Optimizing observations of drizzle onset with millimeter-wavelength radars. *Atmospheric Measurement Techniques*, 10(5):1783–1802, May 2017. ISSN 1867-1381. doi: 10.5194/amt-10-1783-2017. URL https://amt.copernicus.org/articles/10/1783/2017/. Publisher: Copernicus GmbH.

D. Atlas. THE ESTIMATION OF CLOUD PARAMETERS BY RADAR. *Journal of the Atmospheric Sciences*, 11(4):309–317, Aug. 1954. ISSN 1520-0469. doi: 10.1175/1520-0469(1954)011<0309:TEOCPB>2.0.CO;2. URL https://journals.ametsoc.org/view/journals/atsc/11/4/1520-0469_1954_011_0309_teocpb_2_0_co_2.xml. Publisher: American Meteorological Society Section: Journal of the Atmospheric Sciences.

R. J. P. Baedi, J. J. M. de Wit, H. W. J. Russchenberg, J. S. Erkelens, and J. P. V. Poiares Baptista. Estimating effective radius and liquid water content from radar and lidar based on the CLARE98 data-set. *Physics and Chemistry of the Earth, Part B: Hydrology, Oceans and Atmosphere*, 25(10):1057–1062, Jan. 2000. ISSN 1464-1909.

doi: 10.1016/S1464-1909(00)00152-0. URL https://www.sciencedirect.com/science/article/pii/S1464190900001520.

D. Baumgardner, J.-L. Brenguier, A. Bucholtz, H. Coe, P. DeMott, T. Garrett, J.-F. Gayet, M. Herrmann, A. Heymsfield, A. Korolev, M. Krämer, A. Petzold, W. Strapp, P. Pilewskie, J. Taylor, C. Twohy, M. Wendisch, W. Bachalo, and P. Chuang. Airborne instruments to measure atmospheric aerosol particles, clouds and radiation: A cook's tour of mature and emerging technology. *Atmospheric Research*, 102:10–29, Oct. 2011. doi: 10.1016/j.atmosres.2011.06.021.

D. Baumgardner, S. J. Abel, D. Axisa, R. Cotton, J. Crosier, P. Field, C. Gurganus, A. Heymsfield, A. Korolev, M. Krämer, P. Lawson, G. McFarquhar, Z. Ulanowski, and J. Um. Cloud Ice Properties: In Situ Measurement Challenges. *Meteorological Monographs*, 58:9.1–9.23, Jan. 2017. ISSN 0065-9401. doi: 10.1175/AMSMONOGRAPHS-D-16-0011.1. URL https://journals.ametsoc.org/doi/10.1175/AMSMONOGRAPHS-D-16-0011.1.

A. Bell, P. Martinet, O. Caumont, B. Vié, J. Delanoë, J.-C. Dupont, and M. Borderies. W-band radar observations for fog forecast improvement: an analysis of model and forward operator errors. *Atmospheric Measurement Techniques*, 14(7):4929–4946, July 2021. ISSN 1867-8548. doi: 10.5194/amt-14-4929-2021. URL https://amt.copernicus.org/articles/14/4929/2021/.

S. Bony and J.-L. Dufresne. Marine boundary layer clouds at the heart of tropical cloud feedback uncertainties in climate models. *Geophysical Research Letters*, 32(20), 2005. ISSN 1944-8007. doi: 10.1029/2005GL023851. URL https://onlinelibrary.wiley.com/doi/abs/10.1029/2005GL023851. _eprint: https://agupubs.onlinelibrary.wiley.com/doi/pdf/10.1029/2005GL023851.

F. Brient and T. Schneider. Constraints on Climate Sensitivity from Space-Based Measurements of Low-Cloud Reflection. *Journal of Climate*, 29(16): 5821–5835, Aug. 2016. ISSN 0894-8755, 1520-0442. doi: 10.1175/JCLI-D-15-0897.1. URL https://journals.ametsoc.org/view/journals/clim/29/16/jcli-d-15-0897.1.xml. Publisher: American Meteorological Society Section: Journal of Climate.

G. Cesana and H. Chepfer. How well do climate models simulate cloud vertical structure? A comparison between CALIPSO-GOCCP satellite observations and CMIP5 models. *Geophysical Research Letters*, 39(20):L20803, 2012. doi: 10.1029/2012GL053153. URL https://hal.archives-ouvertes.fr/hal-01113124. Publisher: American Geophysical Union.

I. P. o. C. Change. *Climate Change 2013: The Physical Science Basis: Working Group I Contribution to the Fifth Assessment Report of the Intergovernmental Panel on Climate Change*. Cambridge University Press, Mar. 2014. ISBN 978-1-107-05799-9. Google-Books-ID: o4gaBQAAQBAJ.

D. Cimini, T. J. Hewison, L. Martin, J. Güldner, C. Gaffard, and F. S. Marzano. Temperature and humidity profile retrievals from ground-based microwave radiometers during tuc. *Meteorologische Zeitschrift*, 15(1):45–56, 2006.

A. Comerón, C. Muñoz-Porcar, F. Rocadenbosch, A. Rodríguez-Gómez, and M. Sicard. Current Research in Lidar Technology Used for the Remote Sensing of Atmospheric Aerosols. *Sensors*, 17(6):1450, June 2017. doi: 10.3390/s17061450. URL https://www.mdpi.com/1424-8220/17/6/1450. Number: 6 Publisher: Multidisciplinary Digital Publishing Institute.

S. Crewell and U. Löhnert. Accuracy of cloud liquid water path from ground-based microwave radiometry 2. sensor accuracy and synergy. *Radio Science*, 38(3):7–1, 2003.

J. Delanoë and R. J. Hogan. A variational scheme for retrieving ice cloud properties from combined radar, lidar, and infrared radiometer. *Journal of Geophysical Research: Atmospheres*, 113(D7), 2008. ISSN 2156-2202. doi: 10.1029/2007JD009000. URL https://onlinelibrary.wiley.com/doi/abs/10.1029/2007JD009000. _eprint: https://onlinelibrary.wiley.com/doi/pdf/10.1029/2007JD009000.

J. Delanoë, A. Protat, J.-P. Vinson, W. Brett, C. Caudoux, F. Bertrand, J. P. d. Chatelet, R. Hallali, L. Barthes, M. Haeffelin, and J.-C. Dupont. BASTA: A 95-GHz FMCW Doppler Radar for Cloud and Fog Studies. *Journal of Atmospheric and Oceanic Technology*, 33(5):1023–1038, May 2016. ISSN 0739-0572, 1520-0426. doi: 10.1175/JTECH-D-15-0104.1. URL https://journals.ametsoc.org/view/journals/atot/33/5/jtech-d-15-0104_1.xml. Publisher: American Meteorological Society Section: Journal of Atmospheric and Oceanic Technology.

J.-C. Dupont, M. Haeffelin, E. Wærsted, J. Delanoe, J.-B. Renard, J. Preissler, and C. O'Dowd. Evaluation of Fog and Low Stratus Cloud Microphysical Properties Derived from In Situ Sensor, Cloud Radar and SYRSOC Algorithm. *Atmosphere*, 9 (5):169, May 2018. doi: 10.3390/atmos9050169. URL https://www.mdpi.com/2073-4433/9/5/169. Number: 5 Publisher: Multidisciplinary Digital Publishing Institute.

J. Fišák, D. Rezacova, V. Eliáš, and M. Tesar. Comparison of pollutant concentrations in fog (low cloud) water in northern and southern Bohemia. Jan. 2001.

N. I. Fox and A. J. Illingworth. The Retrieval of Stratocumulus Cloud Properties by Ground-Based Cloud Radar. *Journal of Applied Meteorology and Climatology*, 36(5):485–492, May 1997. ISSN 1520-0450, 0894-8763. doi: 10.1175/1520-0450(1997)036<0485:TROSCP>2.0.CO;2. URL https://journals.ametsoc.org/view/journals/apme/36/5/1520-0450_1997_036_0485_troscp_2.0.co_2.xml. Publisher: American Meteorological Society Section: Journal of Applied Meteorology and Climatology.

A. S. Frisch, C. W. Fairall, and J. B. Snider. Measurement of Stratus Cloud and Drizzle Parameters in ASTEX with a K-Band Doppler Radar and a Microwave Radiometer. *Journal of the Atmospheric Sciences*, 52(16):2788–2799, Aug. 1995. ISSN 0022-4928, 1520-0469. doi: 10.1175/1520-0469(1995)052<2788:MOSCAD>2.0.CO;2. URL https://journals.ametsoc.org/view/journals/atsc/52/16/1520-0469_1995_052_2788_moscad_2_0_co_2.xml. Publisher: American Meteorological Society Section: Journal of the Atmospheric Sciences.

A. S. Frisch, G. Feingold, C. W. Fairall, T. Uttal, and J. B. Snider. On cloud radar and microwave radiometer measurements of stratus cloud liquid water profiles. *Journal of Geophysical Research: Atmospheres*, 103(D18):23195–23197, 1998. ISSN 2156-2202. doi: https://doi.org/10.1029/98JD01827. URL https://agupubs.onlinelibrary.wiley.com/doi/abs/10.1029/98JD01827. _eprint: https://agupubs.onlinelibrary.wiley.com/doi/pdf/10.1029/98JD01827.

B. Geerts and Q. Miao. The Use of Millimeter Doppler Radar Echoes to Estimate Vertical Air Velocities in the Fair-Weather Convective Boundary Layer. *Journal of Atmospheric and Oceanic Technology*, 22(3):225–246, Mar. 2005. ISSN 0739-0572, 1520-0426. doi: 10.1175/JTECH1699.1. URL https://journals.ametsoc.org/view/journals/atot/22/3/jtech1699_1.xml. Publisher: American Meteorological Society Section: Journal of Atmospheric and Oceanic Technology.

H. Gerber, B. Arends, and A. Ackerman. New microphysics sensor for aircraft use. *Atmospheric Research*, 31(4):235–252, Apr. 1994. ISSN 01698095. doi: 10.1016/0169-8095(94)90001-9. URL https://linkinghub.elsevier.com/retrieve/pii/0169809594900019.

S. E. Giangrande, D. M. Babb, and J. Verlinde. Processing Millimeter Wave Profiler Radar Spectra. *Journal of Atmospheric and Oceanic Technology*, 18(9):1577–1583, Sept. 2001. ISSN 0739-0572, 1520-0426. doi: 10.1175/1520-0426(2001)018<1577:

PMWPRS>2.0.CO;2. URL https://journals.ametsoc.org/view/journals/atot/18/9/1520-0426_2001_018_1577_pmwprs_2_0_co_2.xml. Publisher: American Meteorological Society Section: Journal of Atmospheric and Oceanic Technology.

I. Gultepe, J. Milbrandt, and S. Belair. Visibility parameterization from microphysical observations for warm fog conditions and its application to Canadian MC2 mode. *86th AMS Annual Meeting*, Feb. 2006.

M. Haeffelin, L. Barthès, O. Bock, C. Boitel, S. Bony, D. Bouniol, H. Chepfer, M. Chiriaco, J. Cuesta, J. Delanoë, P. Drobinski, J.-L. Dufresne, C. Flamant, M. Grall, A. Hodzic, F. Hourdin, F. Lapouge, Y. Lemaître, A. Mathieu, Y. Morille, C. Naud, V. Noël, W. O'Hirok, J. Pelon, C. Pietras, A. Protat, B. Romand, G. Scialom, and R. Vautard. SIRTA, a ground-based atmospheric observatory for cloud and aerosol research. *Annales Geophysicae*, 23(2):253–275, Feb. 2005. ISSN 0992-7689. doi: 10.5194/angeo-23-253-2005. URL https://angeo.copernicus.org/articles/23/253/2005/. Publisher: Copernicus GmbH.

D. L. Hartmann, M. E. Ockert-Bell, and M. L. Michelsen. The Effect of Cloud Type on Earth's Energy Balance: Global Analysis. *Journal of Climate*, 5(11):1281–1304, Nov. 1992. ISSN 0894-8755, 1520-0442. doi: 10.1175/1520-0442(1992)005<1281:TEOCTO>2.0.CO;2. URL https://journals.ametsoc.org/view/journals/clim/5/11/1520-0442_1992_005_1281_teocto_2_0_co_2.xml. Publisher: American Meteorological Society Section: Journal of Climate.

R. Hogan and E. Connor. Facilitating cloud radar and lidar algorithms: the Cloudnet Instrument Synergy/Target Categorization product. Sept. 2004.

R. J. Hogan. A Variational Scheme for Retrieving Rainfall Rate and Hail Reflectivity Fraction from Polarization Radar. *Journal of Applied Meteorology and Climatology*, 46(10):1544–1564, Oct. 2007. ISSN 1558-8424, 1558-8432. doi: 10.1175/JAM2550.1. URL https://journals.ametsoc.org/view/journals/apme/46/10/jam2550.1.xml. Publisher: American Meteorological Society Section: Journal of Applied Meteorology and Climatology.

R. J. Hogan, N. Gaussiat, and A. J. Illingworth. Stratocumulus Liquid Water Content from Dual-Wavelength Radar. *Journal of Atmospheric and Oceanic Technology*, 22 (8):1207–1218, Aug. 2005. ISSN 1520-0426, 0739-0572. doi: 10.1175/JTECH1768.1. URL http://journals.ametsoc.org/doi/10.1175/JTECH1768.1.

A. J. Illingworth, R. J. Hogan, E. J. O'Connor, D. Bouniol, M. E. Brooks, J. Delanoë, D. P. Donovan, J. D. Eastment, N. Gaussiat, J. W. F. Goddard, M. Haeffelin, H. K. Baltink, O. A. Krasnov, J. Pelon, and A. M. Tompkins. Continuous Evaluation of Cloud Profiles in Seven Operational Models Using Ground-Based Observations. page 16, 2007.

N. J. King, K. N. Bower, J. Crosier, and I. Crawford. Evaluating MODIS cloud retrievals with in situ observations from VOCALS-REx. *Atmospheric Chemistry and Physics*, 13(1):191–209, Jan. 2013. ISSN 1680-7324. doi: 10.5194/acp-13-191-2013. URL https://acp.copernicus.org/articles/13/191/2013/.

P. Kollias, E. E. Clothiaux, M. A. Miller, B. A. Albrecht, G. L. Stephens, and T. P. Ackerman. Millimeter-Wavelength Radars: New Frontier in Atmospheric Cloud and Precipitation Research. *Bulletin of the American Meteorological Society*, 88(10):1608–1624, Oct. 2007. ISSN 0003-0007, 1520-0477. doi: 10.1175/BAMS-88-10-1608. URL https://journals.ametsoc.org/doi/10.1175/BAMS-88-10-1608.

P. Kollias, J. Rémillard, E. Luke, and W. Szyrmer. Cloud radar Doppler spectra in drizzling stratiform clouds: 1. Forward modeling and remote sensing applications. *Journal of Geophysical Research: Atmospheres*, 116(D13), 2011. ISSN 2156-2202. doi: 10.1029/2010JD015237. URL https://onlinelibrary.wiley.com/doi/abs/10.1029/2010JD015237. _eprint: https://onlinelibrary.wiley.com/doi/pdf/10.1029/2010JD015237.

O. Krasnov and H. Russchenberg. A synergetic radar-lidar technique for the LWC retrieval in water clouds: Description and application to the Cloudnet data. Jan. 2005.

D. Lamb and J. Verlinde. *Physics and Chemistry of Clouds*. Cambridge University Press, Cambridge, 2011. ISBN 978-0-511-97637-7. doi: 10.1017/CBO9780511976377. URL http://ebooks.cambridge.org/ref/id/CBO9780511976377.

S. Lance. Coincidence Errors in a Cloud Droplet Probe (CDP) and a Cloud and Aerosol Spectrometer (CAS), and the Improved Performance of a Modified CDP. *Journal of Atmospheric and Oceanic Technology*, 29(10):1532–1541, Oct. 2012. ISSN 0739-0572, 1520-0426. doi: 10.1175/JTECH-D-11-00208.1. URL https://journals.ametsoc.org/view/journals/atot/29/10/jtech-d-11-00208_1.xml. Publisher: American Meteorological Society Section: Journal of Atmospheric and Oceanic Technology.

S. Lance, C. A. Brock, D. Rogers, and J. A. Gordon. Water droplet calibration of the Cloud Droplet Probe (CDP) and in-flight performance in liquid, ice and mixed-phase

clouds during ARCPAC. *Atmospheric Measurement Techniques*, 3(6):1683–1706, Dec. 2010. ISSN 1867-1381. doi: 10.5194/amt-3-1683-2010. URL https://amt.copernicus.org/articles/3/1683/2010/. Publisher: Copernicus GmbH.

R. P. Lawson, D. O'Connor, P. Zmarzly, K. Weaver, B. Baker, Q. Mo, and H. Jonsson. The 2D-S (Stereo) Probe: Design and Preliminary Tests of a New Airborne, High-Speed, High-Resolution Particle Imaging Probe. *Journal of Atmospheric and Oceanic Technology*, 23(11):1462–1477, Nov. 2006. ISSN 0739-0572, 1520-0426. doi: 10.1175/JTECH1927.1. URL https://journals.ametsoc.org/view/journals/atot/23/11/jtech1927_1.xml. Publisher: American Meteorological Society Section: Journal of Atmospheric and Oceanic Technology.

R. Lhermitte. Attenuation and Scattering of Millimeter Wavelength Radiation by Clouds and Precipitation. *Journal of Atmospheric and Oceanic Technology*, 7(3):464–479, June 1990. ISSN 0739-0572, 1520-0426. doi: 10.1175/1520-0426(1990)007<0464:AASOMW>2.0.CO;2. URL https://journals.ametsoc.org/view/journals/atot/7/3/1520-0426_1990_007_0464_aasomw_2_0_co_2.xml. Publisher: American Meteorological Society Section: Journal of Atmospheric and Oceanic Technology.

H. Liebe, T. Manabe, and G. Hufford. Millimeter-wave attenuation and delay rates due to fog/cloud conditions. *IEEE Transactions on Antennas and Propagation*, 37(12): 1617–1612, Dec. 1989. ISSN 1558-2221. doi: 10.1109/8.45106. Conference Name: IEEE Transactions on Antennas and Propagation.

H. J. Liebe. An updated model for millimeter wave propagation in moist air. *Radio Science*, 20(5):1069–1089, 1985. ISSN 1944-799X. doi: 10.1029/RS020i005p01069. URL https://onlinelibrary.wiley.com/doi/abs/10.1029/RS020i005p01069. _eprint: https://onlinelibrary.wiley.com/doi/pdf/10.1029/RS020i005p01069.

K. N. Liou. *An Introduction to Atmospheric Radiation*. Elsevier, May 2002. ISBN 978-0-08-049167-7.

N. G. Loeb, B. A. Wielicki, D. R. Doelling, G. L. Smith, D. F. Keyes, S. Kato, N. Manalo-Smith, and T. Wong. Toward Optimal Closure of the Earth's Top-of-Atmosphere Radiation Budget. *Journal of Climate*, 22(3):748–766, Feb. 2009. ISSN 0894-8755, 1520-0442. doi: 10.1175/2008JCLI2637.1. URL https://journals.ametsoc.org/view/journals/clim/22/3/2008jcli2637.1.xml. Publisher: American Meteorological Society Section: Journal of Climate.

U. Löhnert, S. Crewell, C. Simmer, and A. Macke. Profiling Cloud Liquid Water by Combining Active and Passive Microwave Measurements with Cloud Model Statistics. *Journal of Atmospheric and Oceanic Technology*, 18(8):1354–1366, Aug. 2001. ISSN 0739-0572, 1520-0426. doi: 10.1175/1520-0426(2001)018<1354:PCLWBC>2.0.CO;2. URL https://journals.ametsoc.org/view/journals/atot/18/8/1520-0426_2001_018_1354_pclwbc_2_0_co_2.xml. Publisher: American Meteorological Society Section: Journal of Atmospheric and Oceanic Technology.

U. Löhnert, S. Crewell, and C. Simmer. An Integrated Approach toward Retrieving Physically Consistent Profiles of Temperature, Humidity, and Cloud Liquid Water. *Journal of Applied Meteorology and Climatology*, 43(9):1295–1307, Sept. 2004. ISSN 1520-0450, 0894-8763. doi: 10.1175/1520-0450(2004)043<1295:AIATRP>2.0.CO;2. URL https://journals.ametsoc.org/view/journals/apme/43/9/1520-0450_2004_043_1295_aiatrp_2.0.co_2.xml. Publisher: American Meteorological Society Section: Journal of Applied Meteorology and Climatology.

M. Maahn, D. D. Turner, U. Löhnert, D. J. Posselt, K. Ebell, G. G. Mace, and J. M. Comstock. Optimal Estimation Retrievals and Their Uncertainties: What Every Atmospheric Scientist Should Know. *Bulletin of the American Meteorological Society*, 101(9):E1512–E1523, Sept. 2020. ISSN 0003-0007, 1520-0477. doi: 10.1175/BAMS-D-19-0027.1. URL https://journals.ametsoc.org/view/journals/bams/101/9/bamsD190027.xml. Publisher: American Meteorological Society Section: Bulletin of the American Meteorological Society.

F. Maier, J. Bendix, and B. Thies. Simulating Z–LWC Relations in Natural Fogs with Radiative Transfer Calculations for Future Application to a Cloud Radar Profiler. *Pure and Applied Geophysics*, 169(5):793–807, May 2012. ISSN 1420-9136. doi: 10.1007/s00024-011-0332-0. URL https://doi.org/10.1007/s00024-011-0332-0.

T. Marke, K. Ebell, U. Löhnert, and D. D. Turner. Statistical retrieval of thin liquid cloud microphysical properties using ground-based infrared and microwave observations. *Journal of Geophysical Research: Atmospheres*, 121(24):14–558, 2016.

P. Martinet, D. Cimini, F. Burnet, B. Ménétrier, Y. Michel, and V. Unger. Improvement of numerical weather prediction model analysis during fog conditions through the assimilation of ground-based microwave radiometer observations: a 1D-Var study. *Atmospheric Measurement Techniques*, 13(12):6593–6611, Dec. 2020. ISSN 1867-1381. doi: 10.5194/amt-13-6593-2020. URL https://amt.copernicus.org/articles/13/6593/2020/. Publisher: Copernicus GmbH.

G. Mie. Beiträge zur Optik trüber Medien, speziell kolloidaler Metallösungen. *Annalen der Physik*, 330(3):377–445, 1908. ISSN 1521-3889. doi: 10.1002/andp.19083300302. URL https://onlinelibrary.wiley.com/doi/abs/10.1002/andp.19083300302. _eprint: https://onlinelibrary.wiley.com/doi/pdf/10.1002/andp.19083300302.

N. L. Miles, J. Verlinde, and E. E. Clothiaux. Cloud droplet size distributions in low-level stratiform clouds. *Journal of the Atmospheric Sciences*, 57(2):295–311, Jan. 2000. ISSN 0022-4928. doi: 10.1175/1520-0469(2000)057<0295:CDSDIL>2.0.CO;2. URL https://pennstate.pure.elsevier.com/en/publications/cloud-droplet-size-distributions-in-low-level-stratiform-clouds. Publisher: American Meteorological Society.

C. Nam, S. Bony, J.-L. Dufresne, and H. Chepfer. The 'too few, too bright' tropical low-cloud problem in CMIP5 models. *Geophysical Research Letters*, 39 (21), 2012. ISSN 1944-8007. doi: 10.1029/2012GL053421. URL https://onlinelibrary.wiley.com/doi/abs/10.1029/2012GL053421. _eprint: https://agupubs.onlinelibrary.wiley.com/doi/pdf/10.1029/2012GL053421.

M. Ovtchinnikov and Y. L. Kogan. Evaluation of radar retrieval algorithms in stratiform clouds using large-eddy simulations. *Journal of Geophysical Research: Atmospheres*, 105(D13):17351–17359, 2000. ISSN 2156-2202. doi: https://doi.org/10.1029/2000JD900216. URL https://agupubs.onlinelibrary.wiley.com/doi/abs/10.1029/2000JD900216. _eprint: https://agupubs.onlinelibrary.wiley.com/doi/pdf/10.1029/2000JD900216.

E. J. O'Connor, R. J. Hogan, and A. J. Illingworth. Retrieving Stratocumulus Drizzle Parameters Using Doppler Radar and Lidar. *Journal of Applied Meteorology and Climatology*, 44(1):14–27, Jan. 2005. ISSN 1520-0450, 0894-8763. doi: 10.1175/JAM-2181.1. URL https://journals.ametsoc.org/view/journals/apme/44/1/jam-2181.1.xml. Publisher: American Meteorological Society Section: Journal of Applied Meteorology and Climatology.

C. D. Rodgers. *Inverse Methods for Atmospheric Sounding: Theory and Practice*. WORLD SCIENTIFIC, July 2000. ISBN 978-981-02-2740-1 978-981-281-371-8. doi: 10.1142/3171. URL http://www.worldscientific.com/worldscibooks/10.1142/3171.

K. Sarna, D. P. Donovan, and H. W. J. Russchenberg. Estimating the optical extinction of liquid water clouds in the cloud base region. *Atmospheric Measurement Techniques*, 14(7):4959–4970, July 2021. ISSN 1867-1381. doi: 10.5194/amt-14-4959-2021.

URL https://amt.copernicus.org/articles/14/4959/2021/. Publisher: Copernicus GmbH.

K. Sassen and L. Liao. Estimation of Cloud Content by W-Band Radar. *Journal of Applied Meteorology and Climatology*, 35(6):932–938, June 1996. ISSN 1520-0450, 0894-8763. doi: 10.1175/1520-0450(1996)035<0932:EOCCBW>2.0.CO;2. URL https://journals.ametsoc.org/view/journals/apme/35/6/1520-0450_1996_035_0932_eoccbw_2_0_co_2.xml. Publisher: American Meteorological Society Section: Journal of Applied Meteorology and Climatology.

H. Sauvageot and J. Omar. Radar Reflectivity of Cumulus Clouds. *Journal of Atmospheric and Oceanic Technology*, 4(2):264–272, June 1987. ISSN 0739-0572, 1520-0426. doi: 10.1175/1520-0426(1987)004<0264:RROCC>2.0.CO;2. URL https://journals.ametsoc.org/view/journals/atot/4/2/1520-0426_1987_004_0264_rrocc_2_0_co_2.xml. Publisher: American Meteorological Society Section: Journal of Atmospheric and Oceanic Technology.

T. Schneider, J. Teixeira, C. S. Bretherton, F. Brient, K. G. Pressel, C. Schär, and A. P. Siebesma. Climate goals and computing the future of clouds. *Nature Climate Change*, 7(1):3–5, Jan. 2017. ISSN 1758-6798. doi: 10.1038/nclimate3190. URL https://www.nature.com/articles/nclimate3190. Number: 1 Publisher: Nature Publishing Group.

M. D. Shupe. A ground-based multisensor cloud phase classifier. *Geophysical Research Letters*, 34(22), 2007. ISSN 1944-8007. doi: 10.1029/2007GL031008. URL https://onlinelibrary.wiley.com/doi/abs/10.1029/2007GL031008. _eprint: https://onlinelibrary.wiley.com/doi/pdf/10.1029/2007GL031008.

G. L. Stephens, D. G. Vane, R. J. Boain, G. G. Mace, K. Sassen, Z. Wang, A. J. Illingworth, E. J. O'connor, W. B. Rossow, S. L. Durden, S. D. Miller, R. T. Austin, A. Benedetti, and C. Mitrescu. THE CLOUDSAT MISSION AND THE A-TRAIN: A New Dimension of Space-Based Observations of Clouds and Precipitation. *Bulletin of the American Meteorological Society*, 83 (12):1771–1790, Dec. 2002. ISSN 0003-0007, 1520-0477. doi: 10.1175/BAMS-83-12-1771. URL https://journals.ametsoc.org/view/journals/bams/83/12/bams-83-12-1771.xml. Publisher: American Meteorological Society Section: Bulletin of the American Meteorological Society.

G. L. Stephens, D. O'Brien, P. J. Webster, P. Pilewski, S. Kato, and J.-l. Li. The albedo of Earth: The Albedo of Earth. *Reviews of Geophysics*, 53(1):141–163, Mar. 2015.

ISSN 87551209. doi: 10.1002/2014RG000449. URL http://doi.wiley.com/10.1002/2014RG000449.

B. Stevens and S. E. Schwartz. Observing and Modeling Earth's Energy Flows. *Surveys in Geophysics*, 33(3):779–816, July 2012. ISSN 1573-0956. doi: 10.1007/s10712-012-9184-0. URL https://doi.org/10.1007/s10712-012-9184-0.

F. Toledo, J. Delanoë, M. Haeffelin, J.-C. Dupont, S. Jorquera, and C. Le Gac. Absolute calibration method for frequency-modulated continuous wave (FMCW) cloud radars based on corner reflectors. *Atmospheric Measurement Techniques*, 13(12):6853–6875, Dec. 2020. ISSN 1867-1381. doi: 10.5194/amt-13-6853-2020. URL https://amt.copernicus.org/articles/13/6853/2020/. Publisher: Copernicus GmbH.

G. Vali and S. Haimov. Observed extinction by clouds at 95 GHz. *IEEE Transactions on Geoscience and Remote Sensing*, 39(1):190–193, Jan. 2001. ISSN 1558-0644. doi: 10.1109/36.898682. Conference Name: IEEE Transactions on Geoscience and Remote Sensing.

J. Vivekanandan, V. P. Ghate, J. B. Jensen, S. M. Ellis, and M. C. Schwartz. A Technique for Estimating Liquid Droplet Diameter and Liquid Water Content in Stratocumulus Clouds Using Radar and Lidar Measurements. *Journal of Atmospheric and Oceanic Technology*, 37(11):2145–2161, Nov. 2020. ISSN 0739-0572, 1520-0426. doi: 10.1175/JTECH-D-19-0092.1. URL https://journals.ametsoc.org/view/journals/atot/37/11/JTECH-D-19-0092.1.xml. Publisher: American Meteorological Society Section: Journal of Atmospheric and Oceanic Technology.

J. M. Wallace and P. V. Hobbs. *Atmospheric science: an introductory survey*. Number v. 92 in International geophysics series. Elsevier Academic Press, Amsterdam ; Boston, 2nd ed edition, 2006. ISBN 978-0-12-732951-2. OCLC: ocm62421169.

J. Wang and B. Geerts. Identifying drizzle within marine stratus with W-band radar reflectivity. *Atmospheric research*, 69(1-2):1–27, 2003. Publisher: Elsevier.

R. Ware, F. Solheim, R. Carpenter, J. Gueldner, J. Liljegren, T. Nehrkorn, and F. Vandenberghe. Radiometric profiling of tropospheric temperature, humidity and cloud liquid. June 2002.

R. Wood, C. R. Mechoso, C. S. Bretherton, R. A. Weller, B. Huebert, F. Straneo, B. A. Albrecht, H. Coe, G. Allen, G. Vaughan, P. Daum, C. Fairall, D. Chand, L. Gallardo Klenner, R. Garreaud, C. Grados, D. S. Covert, T. S. Bates, R. Krejci, L. M. Russell, S. de Szoeke, A. Brewer, S. E. Yuter, S. R. Springston,

A. Chaigneau, T. Toniazzo, P. Minnis, R. Palikonda, S. J. Abel, W. O. J. Brown, S. Williams, J. Fochesatto, J. Brioude, and K. N. Bower. The VAMOS Ocean-Cloud-Atmosphere-Land Study Regional Experiment (VOCALS-REx): goals, platforms, and field operations. *Atmospheric Chemistry and Physics*, 11(2):627–654, Jan. 2011. ISSN 1680-7324. doi: 10.5194/acp-11-627-2011. URL https://acp.copernicus.org/articles/11/627/2011/.

E. G. Wærsted, M. Haeffelin, J.-C. Dupont, J. Delanoë, and P. Dubuisson. Radiation in fog: quantification of the impact on fog liquid water based on ground-based remote sensing. *Atmospheric Chemistry and Physics*, 17(17):10811–10835, Sept. 2017. ISSN 1680-7316. doi: 10.5194/acp-17-10811-2017. URL https://acp.copernicus.org/articles/17/10811/2017/. Publisher: Copernicus GmbH.

Y. Zhang, S. Chen, W. Tan, S. Chen, H. Chen, P. Guo, Z. Sun, R. Hu, Q. Xu, M. Zhang, W. Hao, and Z. Bu. Retrieval of Water Cloud Optical and Microphysical Properties from Combined Multiwavelength Lidar and Radar Data. *Remote Sensing*, 13(21): 4396, Jan. 2021. ISSN 2072-4292. doi: 10.3390/rs13214396. URL https://www.mdpi.com/2072-4292/13/21/4396. Number: 21 Publisher: Multidisciplinary Digital Publishing Institute.

C. Zhao, S. Xie, S. A. Klein, A. Protat, M. D. Shupe, S. A. McFarlane, J. M. Comstock, J. Delanoë, M. Deng, M. Dunn, R. J. Hogan, D. Huang, M. P. Jensen, G. G. Mace, R. McCoy, E. J. O'Connor, D. D. Turner, and Z. Wang. Toward understanding of differences in current cloud retrievals of ARM ground-based measurements. *Journal of Geophysical Research: Atmospheres*, 117 (D10), 2012. ISSN 2156-2202. doi: 10.1029/2011JD016792. URL https://onlinelibrary.wiley.com/doi/abs/10.1029/2011JD016792. _eprint: https://onlinelibrary.wiley.com/doi/pdf/10.1029/2011JD016792.